REPORT DOCUMENTATION PAGE

1. REPORT DATE *(DD-MM-YYYY)*	2. REPORT TYPE	3. DATES COVERED *(From - To)*
16-10-2014	Final Report	04/23/2010-9/30/2013

4. TITLE AND SUBTITLE	5a. CONTRACT NUMBER
Spectrally Adaptable Compressive Sensing Imaging System	N00014-10-C-0199

5b. GRANT NUMBER

5c. PROGRAM ELEMENT NUMBER

6. AUTHOR(S)	5d. PROJECT NUMBER
Gonzalo Arce, Dennis Prather, Javier Garcia-Frias	

5e. TASK NUMBER

5f. WORK UNIT NUMBER

7. PERFORMING ORGANIZATION NAME(S) AND ADDRESS(ES)	8. PERFORMING ORGANIZATION REPORT NUMBER
University of Delaware 210 Hullihen Hall Newark, DE 19716	ELEG33227310000

9. SPONSORING / MONITORING AGENCY NAME(S) AND ADDRESS(ES)	10. SPONSOR/MONITOR'S ACRONYM(S)
Office of Naval Research Linda Shipp 703-696-8559 linda.shipp@navy.mil	ONR

11. SPONSOR/MONITOR'S REPORT NUMBER(S)

12. DISTRIBUTION / AVAILABILITY STATEMENT

Approved for Public Release, distribution unlimited

13. SUPPLEMENTARY NOTES

14. ABSTRACT

Compressive Spectral Imaging is a revolutionary technique which senses the spatio-spectral information of a scene by using 2D coded projections. The underlying spectral 3D data cube is then recovered using compressed sensing (CS) reconstruction algorithms which assume that the underlying hyperspectral images are sparse in some representation basis. The great advantage of CSI is that the required number of measurements needed for reconstruction is far less than that required by traditional scanning methods. In practice, the Coded Aperture Snapshot Spectral Imaging (CASSI) systems efficiently implement CSI. The compressive CASSI measurements are often modeled as the summation of coded and shifted versions of the spectral voxels of the underlying scene. Thus, each CASSI measurement is a highly structured random projection of the underlying scene. The structure of these projections is dictated by the CASSI optical system whose only varying components are the coded aperture entries. The coded apertures are crucial inasmuch as they determine the quality of the image reconstruction as well as the required minimum number of FPA measurements.

15. SUBJECT TERMS
Imaging, Spectral, 3D, Optical

16. SECURITY CLASSIFICATION OF:			17. LIMITATION OF ABSTRACT	18. NUMBER OF PAGES	19a. NAME OF RESPONSIBLE PERSON
a. REPORT	**b. ABSTRACT**	**c. THIS PAGE**	UU	104	Gonzalo Arce
U	U	U			**19b. TELEPHONE NUMBER** *(include area code)* 302-831-1493

Final Technical Report of Contract ONR N00014-10-C-0199: "Spectrally Adaptable Compressive Sensing Imaging System"

Submitted by:

Gonzalo R. Arce, PI

Dennis W. Prather and Javier Garcia-Frias

Department of Electrical and Computer Engineering

University of Delaware, Newark, DE, 19716

arce@ece.udel.edu   (302) 831-1493

May 2014

Contents

List of Figures

8

List of Tables

Abstract

Compressive Spectral Imaging is a revolutionary technique which senses the spatio-spectral information of a scene by using 2D coded projections. The underlying spectral 3D data cube is then recovered using compressed sensing (CS) reconstruction algorithms which assume that the underlying hyperspectral images are sparse in some representation basis. The great advantage of CSI is that the required number of measurements needed for reconstruction is far less than that required by traditional scanning methods. In practice, the Coded Aperture Snapshot Spectral Imaging (CASSI) systems efficiently implement CSI. The compressive CASSI measurements are often modeled as the summation of coded and shifted versions of the spectral voxels of the underlying scene. Thus, each CASSI measurement is a highly structured random projection of the underlying scene. The structure of these projections is dictated by the CASSI optical system whose only varying components are the coded aperture entries. The coded apertures are crucial inasmuch as they determine the quality of the image reconstruction as well as the required minimum number of FPA measurements.

For almost a century, coded apertures have been designed by the realization that they are well conditioned when used in least square estimation. In fact, commonly used coded apertures in CASSI include Hadamard matrices $\mathbf{H}_N$ whose entries are $(H_N)_{ij} \in \{-1,1\}^{N \times N}$, Hadamard S matrices $\mathbf{S}_N$ where $\mathbf{S}_N = 1/2(1 - \mathbf{H}_N)$, cyclic S-matrices consisting of cyclic permutations of a single master codeword, and Bernoulli random matrices. In this project, a new generation of coded apertures for compressive spectral imaging are developed. The new coded apertures are designed such that they are not only optimal for least square methods, but also for ℓ_1 recovery methods. We coin the new class of coded apertures as "ℓ_1-coded apertures" since these are optimal under the criteria often used in the emerging techniques of CS. Notably, the ℓ_1-coded apertures ensembles can be designed to obtain better quality in the reconstructed images while minimizes the number of required 2D projections.

By designing the coded aperture patterns such that the sensing better satisfies the Restricted Isometry Property (RIP) of the CASSI sensing matrix. The project thus establishes the CASSI RIP constants in terms of the statistical properties of the coded aperture entries such that the concentration of the eigenvalues of the sub-matrices associate to the CASSI sensing matrix is maximized. More specifically, the optimal ℓ_1-coded apertures are designed when their entries are drawn from: (a) Boolean random variables, (b) binary random variables, (c) random signed and unsigned gray scale values. ℓ_1-coded apertures can also be designed for specific applications such as compressive spectral selectivity. Spectral imaging selectivity is sought in diverse applications since relevant information often lies within a subset of spectral bands. Capturing and reconstructing all the spectral bands in the observed image cube, to then throw away a large portion of this data is inefficient. First, the ℓ_1-selective coded aperture optimization problem, in this case, is shown to be analogous to the optimization of a constrained multichannel filter bank. The optimal ℓ_1-selective coded apertures allow the decomposition of the CASSI measurement into several periodic subsets, each having information from only a few selected spectral bands. This first design approach, however, limits the selective spectral profiles to be periodic patterns. Further, the minimum number of shots is restricted to the periodicity of the spectral pattern. In most practical applications, however, the spectral profiles of interest are not periodic and the number of shots is additionally restricted by the application at hand. A second optimization approach for coded aperture spectral selectivity is then developed, where the ℓ_1-selective coded aperture design is generalized to a more general and more effective mathematical framework for multi-shot CASSI, allowing the reconstruction of arbitrary subset of bands, periodic or aperiodic, while minimizing the required number of shots. The new

approach aims at the optimization of ℓ_1-selective coded aperture sets such that a group of compressive spectral measurements is constructed, each with information from a specific subset of bands. A matrix representation of CASSI is introduced permitting the optimization of spectrally selective coded aperture sets. Further, each ℓ_1-selective coded aperture set forms a matrix such that rank minimization is used to reduce the number of CASSI shots needed. Conditions for the code apertures are identified such that a Restricted Isometry Property in the CASSI compressive measurements is satisfied with higher probability.

Finally, this project develops a higher order precision model for the optical sensing in CASSI that includes a more accurate discretization of the underlying signals, leading to image reconstructions less dependent on calibration. Further, the higher order model results in improved image quality reconstruction of the underlying scene than that achieved by the traditional model. The proposed higher precision computational model is also more suitable for reconfigurable multi-frame CASSI systems where multiple coded apertures are used sequentially to capture the hyperspectral scene. Several simulations and experimental measurements demonstrate the benefits of the new discretization model.

Introduction

Compressive Spectral Imaging

Imaging spectroscopy involves the sensing of a large amount of spatial information across a multitude of wavelengths. Traditional imaging spectroscopy sensing techniques scan adjacent spatial zones of an underlying spectral scene and merge the results to construct a spatio-spectral data cube. Push broom spectral imaging sensors, for instance, capture the spectral data cube by using a dispersive element as a prism or grating and one Focal Plane Array (FPA) measurement. These systems capture one snapshot per spatial line of the scene [?] and the measures are concatenated to construct the spatio-spectral data cube. Spectrometers based on optical band-pass filters scan a scene by tuning band-pass filters in wavelength steps such that a whole spectral region is covered [?].

Although these traditional sensing techniques can be designed to measure the spectral information with high resolution, they have the disadvantage that they require to scan a number of zones (spatial lines, spectral bands) linearly in proportion to the desired spatial or spectral resolution. In contrast, Compressive Spectral Imaging (CSI) senses 2D coded projections of the underlying scene such that the number of required projections is far less than the linear scanning case. CSI exploits the fact that hyperspectral images are sparse in some basis representation [?]. More formally, suppose that a hyperspectral signal $\mathcal{F} \in \mathbb{R}^{N \times N \times L}$, or its vector representation $\boldsymbol{f} \in \mathbb{R}^{N \cdot N \cdot L}$, is S sparse on some basis $\boldsymbol{\Psi}$, such that $\boldsymbol{f} = \boldsymbol{\Psi\theta}$ can be approximated by a linear combination of S vectors from $\boldsymbol{\Psi}$ with $S \ll (N \cdot N \cdot L)$. Here, $N \times N$ represents the spatial dimensions and L is the spectral depth of the image data cube. CSI allows $\boldsymbol{f}$ to be recovered from m random projections with high probability when $m \gtrsim S \log(N \cdot N \cdot L) \ll (N \cdot N \cdot L)$.

Coded Aperture Snapshot Spectral Imager (CASSI) is a spectral image sensor that attains FPA compressive measurements by using a coded aperture and a dispersive element. Indeed, CASSI has motivated a great diversity of research directions in areas such as compressive spectral classification [?, ?], compressive tomography [?], compressive holography [?], X-ray compressive imaging [?], compressive fluorescence microscopy, [?], spatio-spectral compressive super-resolution [?, ?], and compressive Raman spectroscopy [?, ?]. The projections measured in CASSI are given by $\mathbf{y} = \mathbf{H}\boldsymbol{f}$, where $\mathbf{H}$ is an $N(N+L-1) \times (N \cdot N \cdot L)$ matrix whose structure is determined by the coded apertures and the dispersive element.

For spectrally rich scenes or very detailed spatial scenes, a single shot CASSI measurement may not provide a sufficient number of compressive measurements. Further, increasing the number of FPA random projections yields to a less ill-posed problem, however, each additional snapshot requires more integration time at the detector. Each additional shot uses a distinct coded aperture that remains fixed during the integration time of the detector. This will rapidly increase the quality of image reconstruction. The additional time required to sense the supplemental FPA projections can be impractical in applications such as hyperspectral sensing at video rates [?]. Increasing the number of FPA projections also reduces the compressive advantage of CSI. Minimizing the required number of FPA projections is thus a key issue in CSI. The CASSI architecture has been recently modified to admit multiple snapshots, each admitting a different coded aperture pattern. Multi shot CASSI can thus yield a less ill-posed inverse problem and consequently improved signal recovering [?, ?]. The time-varying coded apertures can be implemented using micro-piezo motors [?] or through the use of Digital Micromirror Devices [?, ?]. Denote the ℓth FPA measurement as $\mathbf{y}^\ell = \mathbf{H}^\ell \boldsymbol{f}$ where $\mathbf{H}^\ell$ represents the effects of the ℓth coded aperture. The set of K FPA measurements, each with a different coded aperture is then assembled as $\mathbf{y} = \left[(\mathbf{y}^0)^T, \ldots, (\mathbf{y}^{K-1})^T \right]^T$.

The projections in CASSI can be alternatively expressed as $\mathbf{y} = \mathbf{H\Psi\theta} = \mathbf{A\theta}$ where the matrix $\mathbf{A} = \mathbf{H\Psi}$ is the sensing matrix. The underlying data cube is reconstructed as $\tilde{\boldsymbol{f}} = \mathbf{\Psi}\left(\min_{\boldsymbol{\theta}} ||\mathbf{y} - \mathbf{H\Psi\theta}||_2 + \tau||\boldsymbol{\theta}||_1\right)$ where $\mathbf{H} = \left[(\mathbf{H}^0)^T, \ldots, (\mathbf{H}^{K-1})^T\right]^T$, $\boldsymbol{\theta}$ is an S sparse representation of $\boldsymbol{f}$ on the basis $\mathbf{\Psi}$, and τ is a regularization constant.

Coded Aperture Design in CASSI

A critical component in this inverse problem, is the structure of the sensing matrix $\mathbf{A} \triangleq \mathbf{H\Psi}$ as it ultimately determines the attainable quality of reconstruction. While the optical architecture in CASSI partially imposes a well defined sparse structure to the sensing matrix $\mathbf{A}$, the coded apertures used in each measurement shot, ultimately determine the structure of $\mathbf{A}$. The objective in CASSI is thus to optimally design the set of ℓ_1-coded apertures so as to forge a structure on $\mathbf{A}$ that minimizes the number of FPA snapshots while attaining the highest quality reconstruction. To this end, this project explores the interplay between the Restricted Isometry Property and the set of coded apertures used in CASSI.

The Restricted Isometry Property (RIP) characterizes the "goodness" of a matrix in CS, and it is used to develop many theorems in CS. It establishes the conditions necessary for $\mathbf{A}$ such that the ℓ_2 norm of the underlying 3D spectral image is approximately preserved under the transformation $\mathbf{A\theta}$. More precisely, the restricted isometry constant δ_s of the matrix $\mathbf{A}$ is the smallest constant such that $(1 - \delta_s)||\boldsymbol{\theta}||_2 \leq ||\mathbf{A\theta}||_2 \leq ||\boldsymbol{\theta}||_2(1 + \delta_s)$ [?]. The RIP requires that all $m \times |T|$ column submatrices $\mathbf{A}_{|T|}$ of $\mathbf{A}$ are well conditioned for all $|T| \leq S$. Indeed, the RIP imposes that all the eigenvalues of the matrices $\mathbf{A}_{|T|}^T\mathbf{A}_{|T|}$ are in the interval $[1 - \delta_s \ , \ 1 + \delta_s]$. The probability of satisfying this condition is calculated by estimating the statistical distribution of the maximum eigenvalue λ_{max} of the matrices $\mathbf{A}_{|T|}^T\mathbf{A}_{|T|} - \mathbf{I}$ where $\mathbf{I}$ is an identity matrix. The distribution of the maximum eigenvalue λ_{max} is estimated using the concentration of measure for random matrices developed in [?]. The RIP condition also implies a stable recovery of the signal $\boldsymbol{\theta}$ from the projections $\mathbf{A\theta}$ using an l_1 optimization algorithm [?]. Furthermore, the RIP can be used to determine bounds on the required number of measurements needed for successful CS reconstruction. These bounds depend on the structure of the underlying sensing matrix.

The first approach to characterize the RIP in CASSI was given in [?], where it was assumed that the RIP for the matrix $\mathbf{A}$ is satisfied for some constant δ_s, then conditions on the coded apertures were determined so that the RIP is better satisfied. These results, however, do not provide the explicit parameters for the bounds needed in the RIP, such as the probability of error, or the bound on the minimum number of FPA measurements for stable recovery. Results in [?] also do not exploit the RIP in the optimal design of the coded apertures. In fact, commonly used coded apertures in CASSI include Hadamard matrices $\mathbf{H}_N$ whose entries are $(H_N)_{ij} \in \{-1, 1\}^{N \times N}$, Hadamard S matrices $\mathbf{S}_N$ where $\mathbf{S}_N = 1/2(1 - \mathbf{H}_N)$ [?], cyclic S-matrices consisting of cyclic permutations of a single master codeword [?], and Bernoulli random matrices [?, ?]. The use of these coded apertures in CASSI has been principally motivated by the realization that they are well conditioned when used in least square estimation [?, ?]. However, these code designs do not fully exploit the rich theory of CS. In particular, they do not exploit the RIP condition or the concentration of measure of the respective random submatrices of $\mathbf{A}$ to define optimal coded aperture sets.

The set of optimal coded apertures under the criterion of euclidian and ℓ_1 distances are coined here as ℓ_1 coded apertures. There are several types of ℓ_1 codes, boolean ($H_{ij} \in \{0, 1\}$), binary ($H_{ij} \in \{-1, 1\}$), grayscale ($H_{ij} \in \{\frac{0}{K-1}, \frac{1}{K-1}, \ldots, 1\}$ and $H_{ij} \in \{-1, \frac{1-(K-1)/2}{(K-1)/2}, \frac{2-(K-1)/2}{(K-1)/2}, \ldots, 1\}$), and other possible combinations. The optimal ℓ_1-coded apertures are also designed for spectral selectivity. Spectral selectivity is of interest in many applications, including wide-area airborne surveillance, remote sensing, and tissue spectroscopy in medicine. The optimal spectral bands in airborne surveillance, for instance, depend on atmospheric conditions, time of day, the targets of interest, and the background against which the targets are viewed [?]. In these applications, the spectral signatures of interest live in a spectral band subspace. Efforts placed on acquiring the entire spectral image cube, to then throw away a large portion of this data is wasteful in many regards.

A first approach for spectral selectivity is developed when the selective spectral profiles are limited

to periodic patterns and the minimum number of shots is restricted to the periodicity of the spectral pattern. In most practical applications, however, the spectral profiles of interest are not periodic and the number of shots is restricted by the application. Then a second approach is developed which establishes a more general and more effective mathematical framework for multi-shot CASSI and the corresponding algorithms for ℓ_1-selective coded aperture optimization that allow the reconstruction of arbitrary subset of bands, periodic or aperiodic, whilst minimizing the required number of shots.

The organization of the document is as follows:

Chapter 1 describes the principal theoretical concepts involved in the project. The concept of sparsity is illustrated and the physical phenomenon in CASSI is presented. The techniques to recover the underlying signal and the Restricted Isometry Property are also presented.

Chapter 2 presents the coded aperture design for spectral selectivity in CASSI. In many applications selective spectral imaging is sought since relevant information often lies within a subset of spectral bands. Capturing and reconstructing all the spectral bands in the observed image cube, to then throw away a large portion of this data is inefficient. To this end, this chapter extends the concept of CASSI to a system admitting multiple shot measurements which leads not only to higher quality of reconstruction, but also to spectrally selective imaging when the sequence of code aperture patterns is optimized. The coded aperture optimization problem is shown to be analogous to the optimization of a constrained multichannel filter bank. The optimal coded apertures allow the decomposition of the CASSI measurement into several subsets, each having information from only a few periodical selected spectral bands. The rich theory of compressive sensing is used to effectively reconstruct the spectral bands of interest from the measurements. A number of simulations are developed to illustrate the spectral imaging characteristics attained by optimal coded aperture. This chapter limits the spectral desired bands to periodical patterns, one more generalized method is presented in Chapter 3.

Chapter 3 extends the selective coded apertures developed in Chapter 2 to admit periodical and non-periodical desired spectral profiles. More specifically, a new coded aperture design framework for multi-frame Code Aperture Snapshot Spectral Imaging (CASSI) system is presented. It aims at the optimization of coded aperture sets such that a group of compressive spectral measurements is constructed, each with information from a specific subset of bands. A matrix representation of CASSI is introduced permitting the optimization of spectrally selective coded aperture sets. Further, each coded aperture set forms a matrix such that rank minimization is used to reduce the number of CASSI shots needed. Conditions for the coded apertures are identified such that a Restricted Isometry Property in the CASSI compressive measurements is satisfied with higher probability. Simulations show higher quality of spectral image reconstruction than those attained by systems using Hadamard or random coded aperture sets.

Chapter 6 presents a more precise model for the phenomenon in CASSI. The compressive CASSI measurements are often modeled as the summation of coded and shifted versions of the spectral voxels of the underlying scene. This coarse approximation of the analog CASSI sensing phenomena is then compensated by calibration preprocessing prior to signal reconstruction. This Chapter develops a higher order precision model for the optical sensing phenomenon in CASSI that includes a more accurate discretization of the underlying signals, leading to image reconstructions less dependent on calibration. Further, the higher order model results in improved image quality reconstruction of the underlying scene than that achieved by the traditional model. The proposed higher precision computational model is also more suitable for reconfigurable multi-frame CASSI systems where multiple coded apertures are used sequentially to capture the hyperspectral scene. Several simulations and experimental measurements demonstrate the benefits of the new discretization model.

Chapter 5 discusses the implementation of the CS theory in building a testbed optical imaging system. This testbed is suitable for hyperspectral imaging applications wherein both the spatial and spectral information of the imaging scene are of interest. We demonstrate the feasibility of this testbed by developing a Digital-Micromirror-Device-based Snapshot Spectral Imaging (DMD-SSI) system, which implements CS measurement processes on the 3D spatial/spectral information of the imaging scene.

Tens of spectral images can be reconstructed from the DMD-SSI system simultaneously without any mechanical or temporal scanning processes.

Impact of Research and Contribution

The contributions of the project are mainly related with the optimal design of coded apertures in compressive spectral imaging and its corresponding testbed implementation. The innovation of the code design presented here is the design of the coded aperture based not only the ℓ_2 norm but also based on the ℓ_1 distance. The coded apertures ensembles are calculated to obtain spectral selectivity, minimum RIP constants, minimum number of shots. Further the codes are also designed to be used in applications as compressive classification, spatial and spectral super-resolution. The optimization of the coded apertures consists on to determine the spatial structure of the patterns to obtain the maximum quality in the reconstructed images while it uses the minimum number of measurements. Additionally, a more precise discretization model for CASSI is developed. The new model is more suitable for the calibration of the coded apertures in multi-frame CASSI.

Chapter 1

Compressive Spectral Imaging

1.1   Sparsity

Compressive sensing exploits the fact that most of the signals are sparse in some representation basis $\mathbf{\Psi}$. Hyperspectral images are sparsified using a separate basis for the spatial axes $\mathbf{\Psi}_{2D}$ and other for the spectral axis $\mathbf{\Psi}_{1D}$ [?]. Commonly, the 2D wavelet transform is used to sparsify the images at a specific wavelength. The spectral axis can be sparsified using a 1D Wavelength Transform or the Cosine Transform. Thus, the hyperspectral image $\mathbf{f}$ is expressed as $\mathbf{f} = \mathbf{\Psi}_{2D} \otimes \mathbf{\Psi}_{1D} \boldsymbol{\theta}$ where $\otimes$ is the Kronecker product. Other basis can also be used as the Principal Component Vectors or pre-trained dictionaries, however, these representations require previous knowledge about the underlying signals. Figures 1.1 and 1.2 illustrate the sparse representation coefficients for three different basis representation and two different data bases. The first representation (Figures 1.1(b) and 1.2(b)) uses a 1D Wavelet Transform to represent the data cubes, thus $\mathbf{f} = \mathbf{\Psi}_{1D} \boldsymbol{\theta}$. The second case (Figures 1.1(c) and 1.2(c)) uses a 2D Wavelet Transform is used such that $\mathbf{f} = \mathbf{\Psi}_{2D} \boldsymbol{\theta}$. The third approach uses the Kronecker of the 2D wavelet basis and the Cosine Transform. It can be observed clearly that the Kronecker basis produces the most sparse representation (Figures 1.1(d) and 1.2(d)).

(a) Original datacube   (b) 1D Wavelet basis   (c) 2D Wavelet basis   (d) Kronecker basis
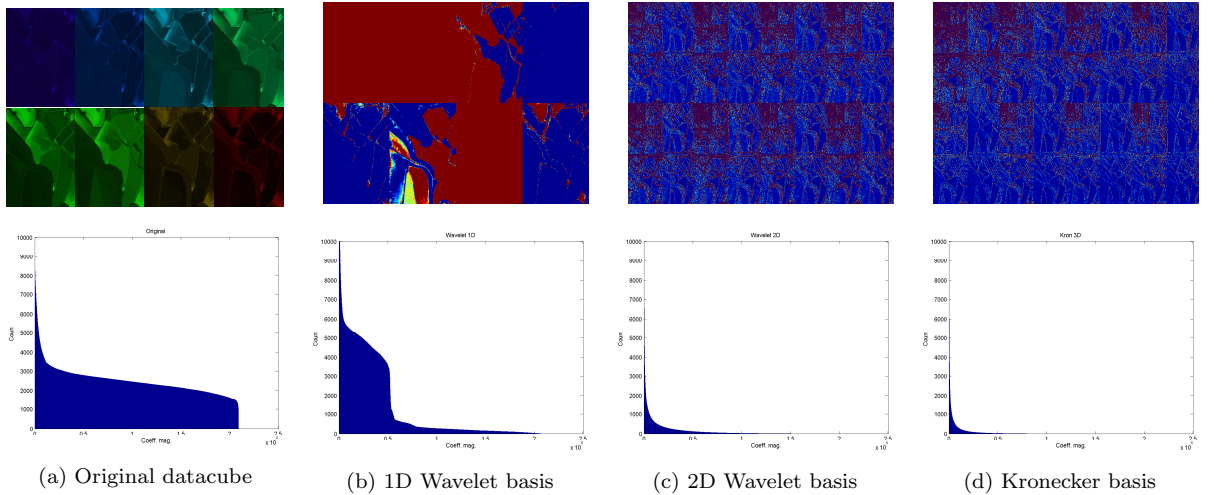
Figure 1.1: Compression basis comparison. (b) 1D Wavelet, (c) 2D Wavelet, and (d) Kronecker (DCT-2D Wavelet) basis representation.

To illustrate the effect of the sparse basis representation, Figures 1.4 - 1.10 depict approximations of hyperspectral images using different levels of sparsity. These approximations are calculated by expressing the underlying signal in a determined representation basis, then the estimated coefficients are sorted by magnitude. A given percentage of the sorted coefficients are held and the remanning are set to zero.

(a) Original datacube   (b) 1D Wavelet basis   (c) 2D Wavelet basis   (d) Kronecker basis
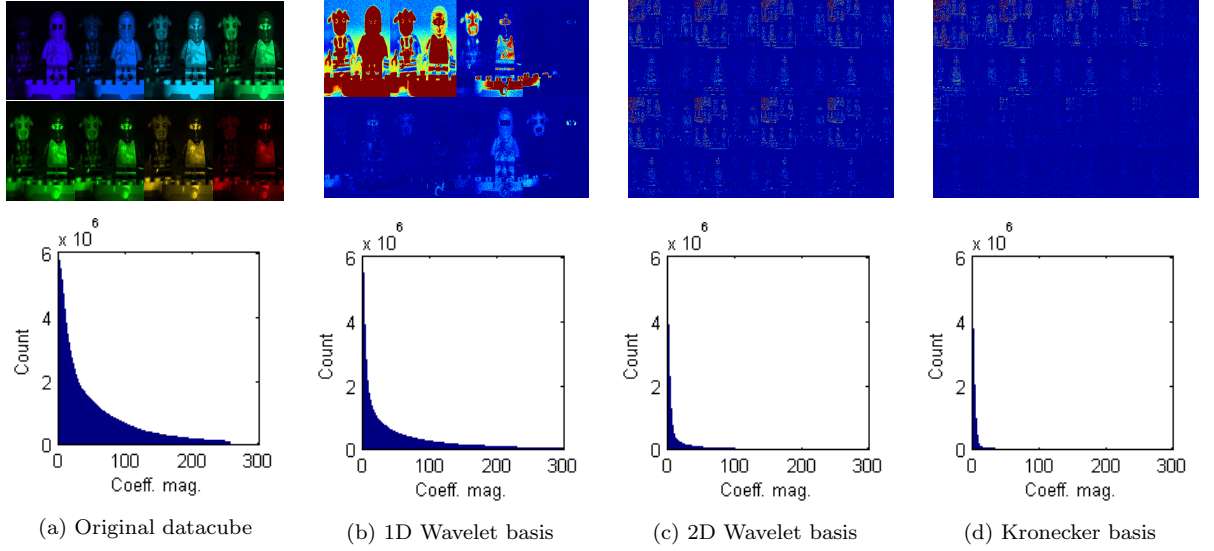
Figure 1.2: Compression basis comparison. (a) Original scene. (b) 1D Wavelet. (c) 2D Wavelet. (d) Kronecker (DCT-2D Wavelet)

The resulting coefficients are transformed back to the original space to generate the approximate signal. Specifically, Figures 1.3 and 1.7 depicts two data cubes used to illustrate the sparsity concepts. Figures 1.4-Figures 1.6 illustrate the results for the first data cube, and Figures 1.8-Figures 1.10 shows the results for the second data cube. The sparsity results are shown for the spectral bands 1, 3, 5 and 7 of the original data cubes.

Figures 1.4(b)-(d) illustrate the approximations by holding only the 1, 5, and 10 percent of the samples of the underlying signals in the first data cube. Figures 1.4(b)-(d) use the 1D Wavelet as representation function. Figures 1.5(b)-(d) and Figures 1.6(b)-(d) illustrate the results for the 2D Wavelet and Kronecker representation, respectively. Figures 1.8(b)-(d) illustrate the approximations by holding only the 1, 5, and 10 percent of the samples of the signals in the second data cube. Again, Figures 1.8(b)-(d) use the 1D Wavelet as representation function. Figures 1.9(b)-(d) and Figures 1.10(b)-(d) illustrate the results for the 2D Wavelet and Kronecker representation, respectively. Notice as the images can be approximated with high quality using only a small percentage of the original number of samples. Compressive spectral imaging takes advantages of this sparsity phenomenon to solve the inverse problem of recovering a given signal from its random projections.

1.2 Sensing Problem

The sensing physical phenomena in CASSI is strikingly simple, yet it adheres to the incoherence principles required in CS. In its simplest form, CASSI measurements are realized optically by a coded aperture, a dispersive element such as a prism, and a focal plane array detector [?, ?]. The coding is applied to the (spatial-spectral) image source density $f_0(x; y; \lambda)$ by means of a coded aperture $T(x; y)$ as realized by the CASSI system depicted in Fig. 1.11, where $(x; y)$ are the spatial coordinates and λ is the wavelength [?]. The resulting coded field $f_1(x; y; \lambda)$ is subsequently modified by a dispersive element before it impinges onto the FPA detector. The compressive measurements across the FPA are realized by the integration of the dispersed field $f_2(x; y; \lambda)$ over the detector's spectral range sensitivity.

It was shown in [?, ?] that the discretized output at the detector follows

$$Y_{j\ell} = \sum_{k=0}^{L-1} \mathcal{F}_{j(\ell+k)(k)} T_{j(\ell+k)} + \omega_{j\ell} \tag{1.1}$$

where $Y_{j\ell}$ is the intensity measured at the j, ℓ position of the detector whose dimensions are $N \times (N+L-1)$,

17
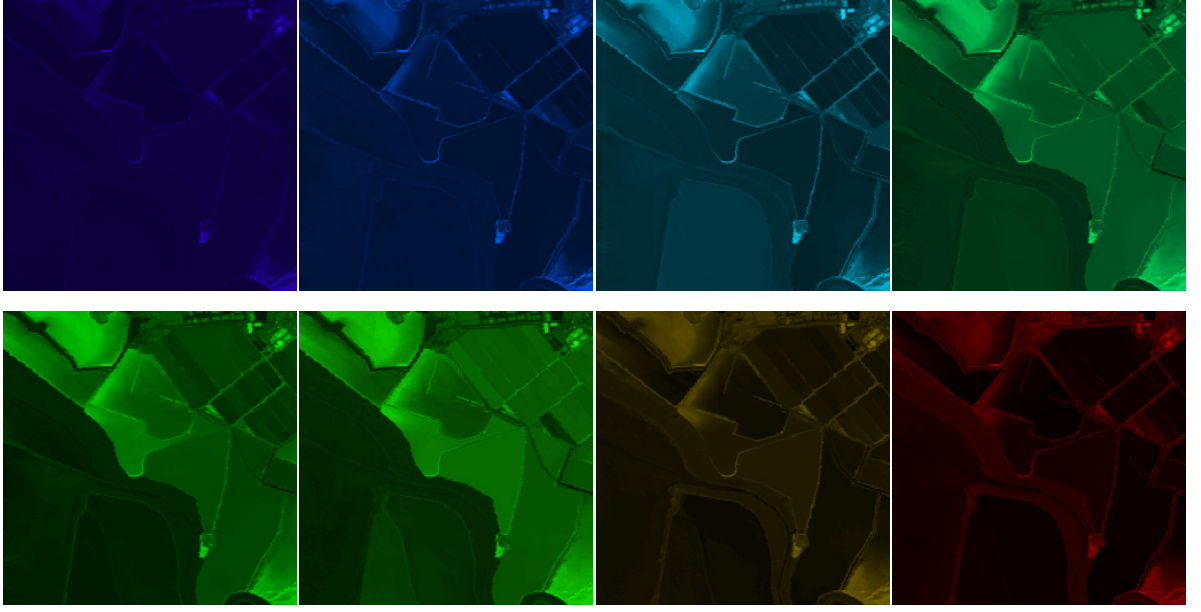
Figure 1.3: Original hyperspectral signal. The first row contains the spectral bands 1- 4, and the second row contains the spectral bands 5-8.

$\mathcal{F}$ is the discretized spectral data cube, L is the number of spectral bands, $T_{j\ell}$ is the coded aperture, and $\omega^i_{j\ell}$ is the noise of the system. Assume that the band-pass filter of the instrument limits the spectral components between λ_1 and λ_2. If the pixel width of the detector and of the coded aperture are both equal to Δ, then the number of resolvable bands L is limited by $L = \alpha \frac{\lambda_2 - \lambda_1}{\Delta}$ where $\alpha\lambda$ is the dispersion induced by the prism. The spectral resolution is limited by $\frac{\Delta}{\alpha}$. The horizontal and vertical spatial resolutions are limited by Δ and the number of spatially resolvable pixels of the underlying scene is $N \times N$.

The sensing mechanism is illustrated in Fig. 1.12 and further described as follows. Since the spectral dispersion in the prism affects the field along one spatial dimension, a slice CASSI model is sufficient to characterize the sensor. Figure 1.12 shows a slice $\mathbf{F}$ of the data cube $\mathcal{F}$ along the spectral plane and the qth spatial dimension of dispersion. In this case (1.1) would represent the model of a slice of CASSI. The slice is first coded in amplitude by the coded aperture T where the code is "block"or "unblock". In essence, when a "block"code aperture element is encountered, the energy along the entire row of the slice is "punched out". The coded field is then sheared along the spectral dimension as it transverse the prism as illustrated in Fig. 1.12. Finally, the coded and dispersed field is "collapsed" in the spectral dimension by integration in the FPA detector. Notice how the various optical phenomena realize compressive linear projections onto the detector. To attain the 2D CASSI sensor model, one must then replicate the above slice model for all the remaining slices of the cube, to a complete 2D detector.

For spectrally rich scenes or very detailed spatial scenes, a single shot FPA measurement is not sufficient and additional shots are required, each with a distinct code aperture that remains fixed during the integration time of the detector. Time-varying coded apertures can be realized by a spatial light modulator (SLM) or by a lithographic mask actioned by a piezoelectric device [?, ?, ?]. It was also shown in [?, ?] that the ensemble of say $K << L$ FPA shots in 1-D vectorized form $\mathbf{y} = \left[\mathbf{y}_0^T, \dots, \mathbf{y}_{K-1}^T\right]^T$ can be rewritten in the standard form of an underdetermined system of linear equations

$$\mathbf{y} = \mathbf{A}\boldsymbol{\theta} = \mathbf{H}\boldsymbol{\Psi}\boldsymbol{\theta} + \boldsymbol{\omega} \tag{1.2}$$

where $\mathbf{A} = \mathbf{H}\boldsymbol{\Psi} \in \mathbb{R}^{KN^2 \times LN^2}$ is the CASSI sensing matrix, $\boldsymbol{\theta}$ is a sparse representation of the data cube in a 3-dimensional base $\boldsymbol{\Psi}$, and $\boldsymbol{\omega}$ represents the noise of the system. The matrix $\mathbf{H}$ in (1.2) accounts for the effects of the coded aperture and the prism. The sensing matrix $\mathbf{A}$ thus couples $\mathbf{H}$ with the representation basis $\boldsymbol{\Psi}$. The coded aperture is considered binary and the dispersive element is considered linear. In practice, it is necessary take into account the various optical artifacts and non-ideal characteristic of the optical system. The underlying computational concepts are general and are thus, in
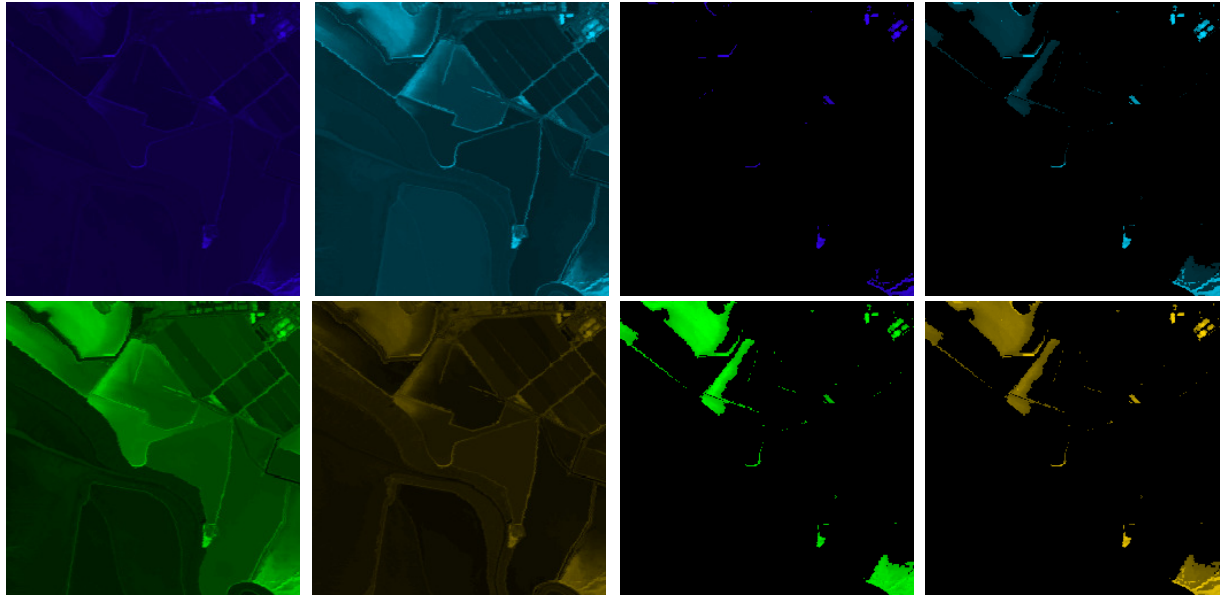
(a) Original spectral bands   (b) W1D (1%)
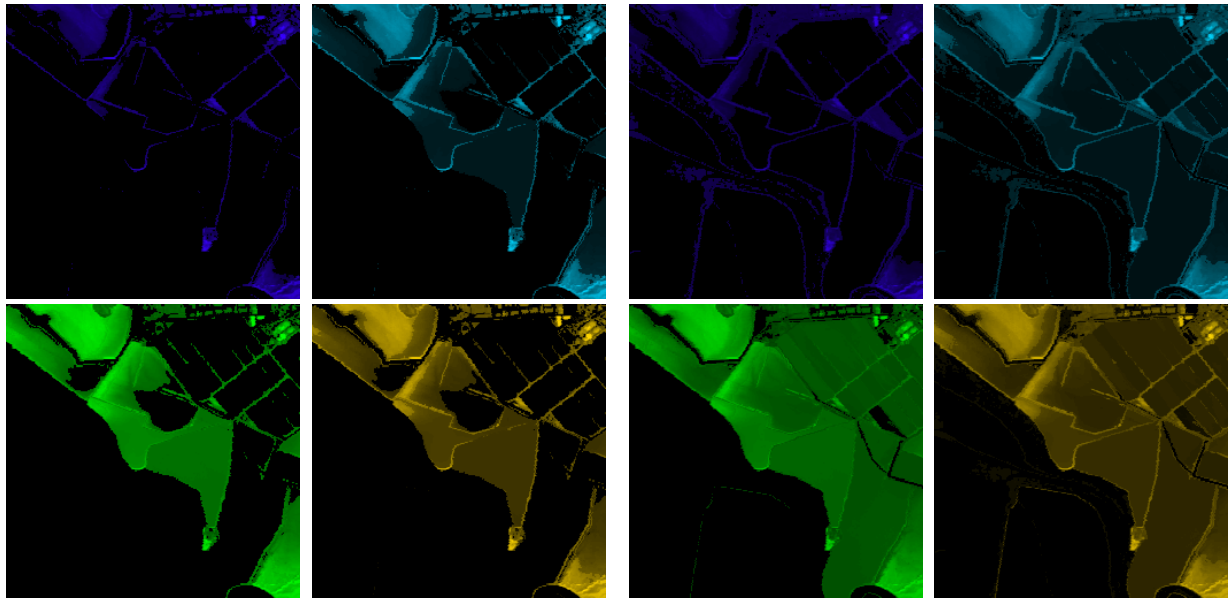
(c) W1D (5%)   (d) W1D (10%)

Figure 1.4: Sparse hyperspectral signal representation using the 1D Wavelet basis function. The spectral bands in (a) are represented using (b) 1% (c) 5%, and (d) 10% of the sparse representation coefficients.

(a) Original spectral bands　　　　　　　　(b) W2D (1%)

(c) W2D (5%)　　　　　　　　(d) W2D (10%)
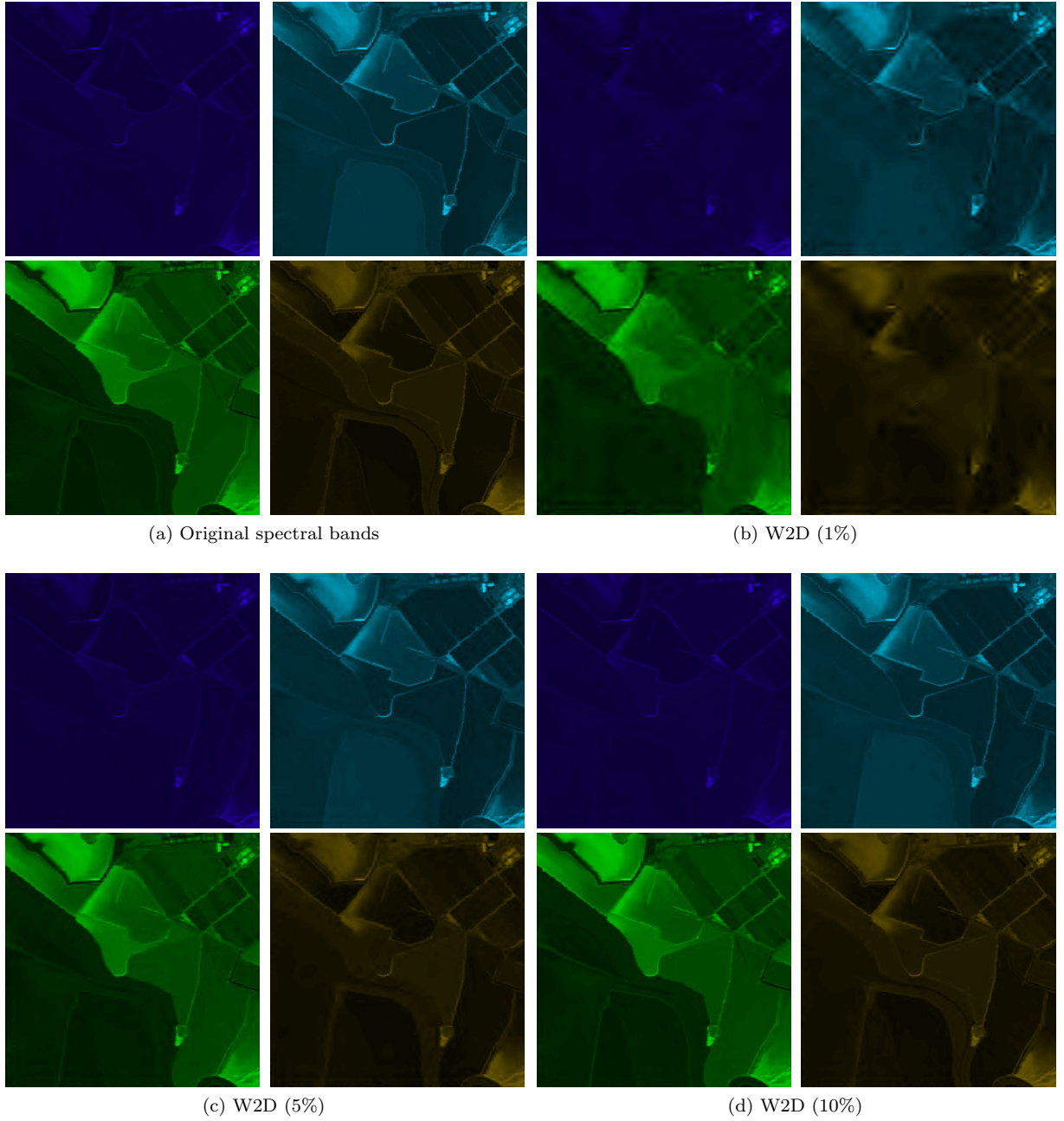
Figure 1.5: Sparse hyperspectral signal representation using the 2D Wavelet basis function. The spectral bands in (a) are represented using (b) 1% (c) 5%, and (d) 10% of the sparse representation coefficients.

(a) Original spectral bands

(b) Kronecker (1%)

(c) Kronecker (5%)
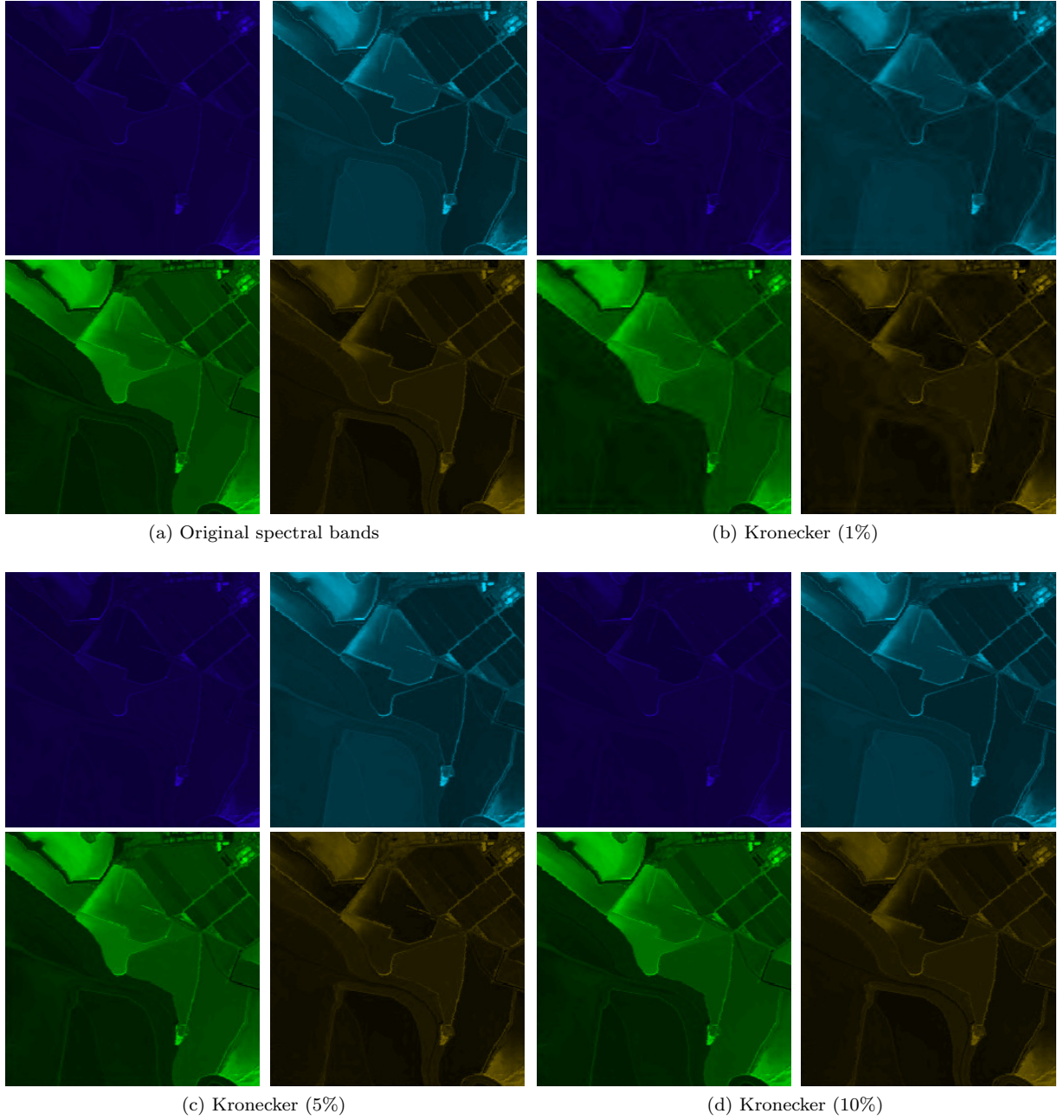
(d) Kronecker (10%)

Figure 1.6: Sparse hyperspectral signal representation using the Kronecker basis function (DCT-2D Wavelet). The spectral bands in (a) are represented using (b) 1% (c) 5%, and (d) 10% of the sparse representation coefficients.
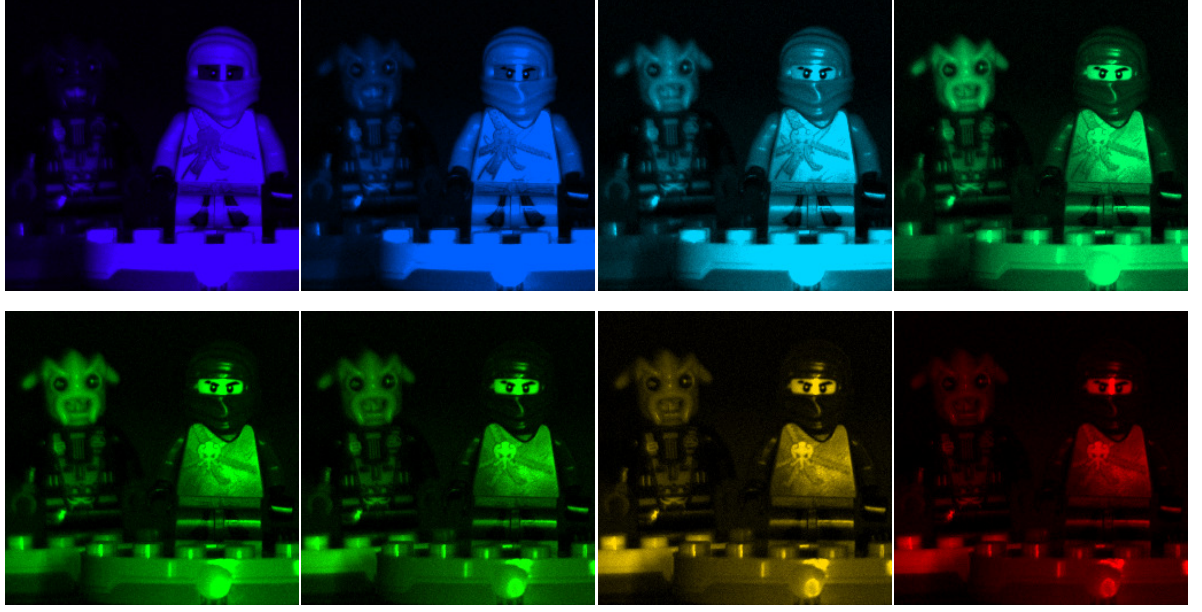
(a) Original datacube

Figure 1.7: Original hyperspectral signal. The first row contains the spectral bands 1- 4, and the second row contains the spectral bands 5-8.

principle, applicable to imaging with FPAs sensitive to any region of the visible and IR electromagnetic spectrum.

1.3   Reconstruction

The underlying hyperspectral signal $\mathbf{f} \in \mathbb{R}^{N^2 L}$ must be recovered from the set of random projections $\mathbf{y} = \mathbf{A}\mathbf{f} \in \mathbb{R}^m$ where $m << N^2 L$. Thus, the signal recovery in CASSI entails solving an underdetermined linear system of equations. More specifically, the signal $\mathbf{f}$ is estimated as

$$\tilde{\mathbf{f}} = \mathbf{\Psi} \left(\min_{\boldsymbol{\theta}} ||\mathbf{y} - \mathbf{H}\mathbf{\Psi}\boldsymbol{\theta}||_2 + \tau ||\boldsymbol{\theta}||_1 \right) \tag{1.3}$$

where $\mathbf{H} = \left[\mathbf{H}_0^T, \ldots, \mathbf{H}_{K-1}^T\right]^T$, $\boldsymbol{\theta}$ is an S sparse representation of $\mathbf{f}$ on the basis $\mathbf{\Psi}$, and τ is a regularization constant. Solving (1.3) relies on the rich theory of CS which offers a number of efficient reconstruction algorithms, including Matching Pursuit type algorithms [?] or interior-point methods such as GPSR [?, ?]. In the GPSR algorithm, for example, each iteration requires in the order of $O(KN^4L)$ operations. Hence, the computational complexity scales rapidly with N and L. The probability of correct reconstruction of the signal $\mathbf{f}$ is completely determined by the structure of the sensing matrix $\mathbf{A} = \mathbf{H}\mathbf{\Psi} \in \mathbb{R}^{KN^2 \times LN^2}$ where N^2 is the size of the FPA sensor, L is the number of spectral bands, and K is the number of measurement shots, with $K << L$. Increasing the number of FPA random projections yields to a less ill-posed problem, however, each additional snapshot requires more integration time at the detector. The additional time required to sense the supplemental FPA projections can be prohibited in applications such as hyperspectral sensing at video rates [?]. Increasing the number of FPA projections also reduces the compression advantage of CSI. Minimizing the required number of FPA projections is thus of interest in CSI applications. The required number of projections in CASSI to correct image reconstruction is determined by the Restricted Isometry Property (RIP) of the matrix $\mathbf{A}$. The RIP property can be modified by designing the set of coded aperture patterns. The optimal set of code aperture patterns is designed such that the RIP property is satisfied using the minimum number of patterns.

A more appropriate alternative to increase the probability of correct reconstruction is by designing

(a) Original spectral bands

(b) W1D (1%)

(c) W1D (5%)

(d) W1D (10%)
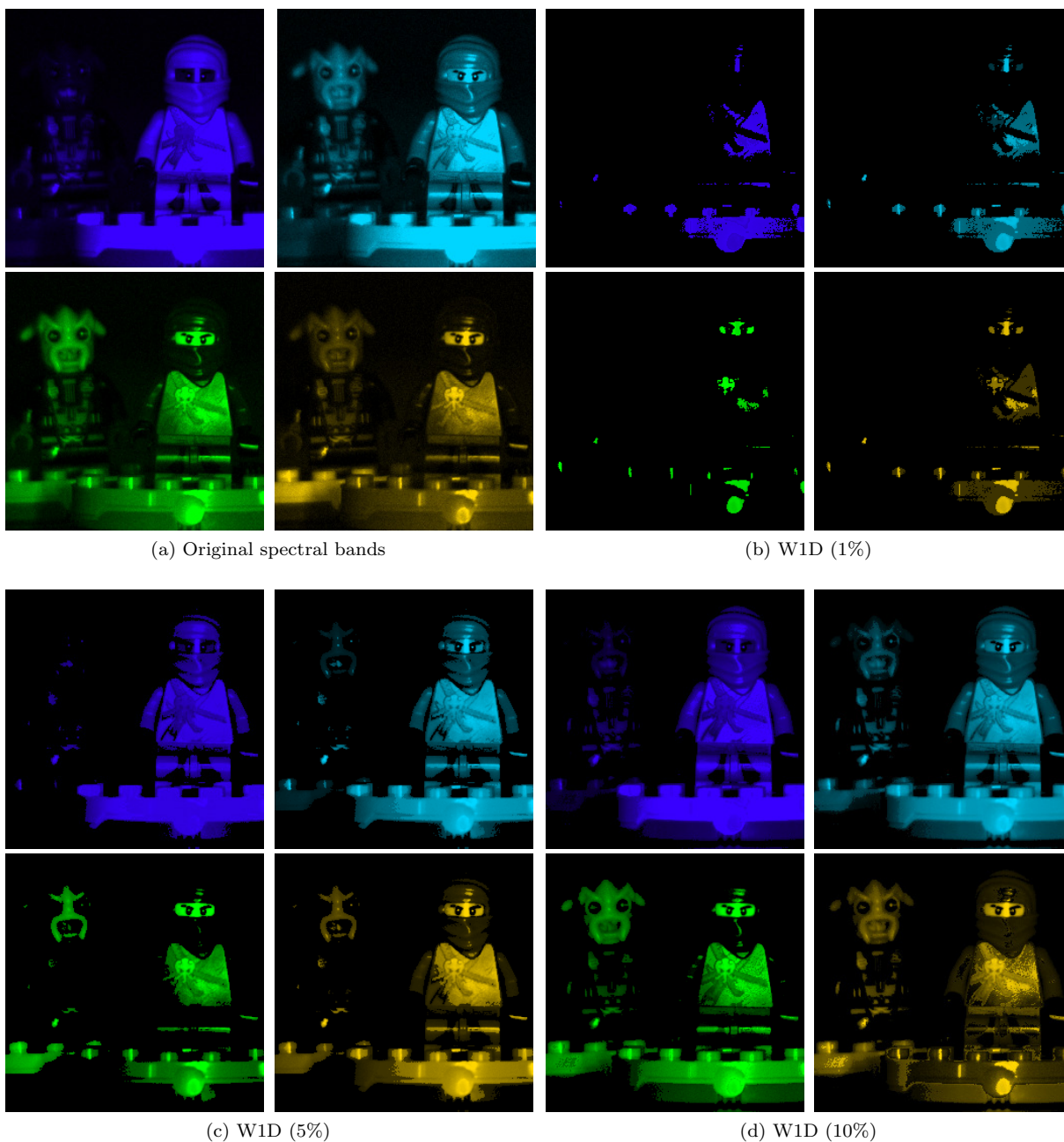
Figure 1.8: Sparse hyperspectral signal representation using the 1D Wavelet function. The spectral bands in (a) are represented using (b) 1% (c) 5%, and (d) 10% of the sparse representation coefficients.

(a) Original spectral bands   (b) W2D (1%)

(c) W2D (5%)   (d) W2D (10%)
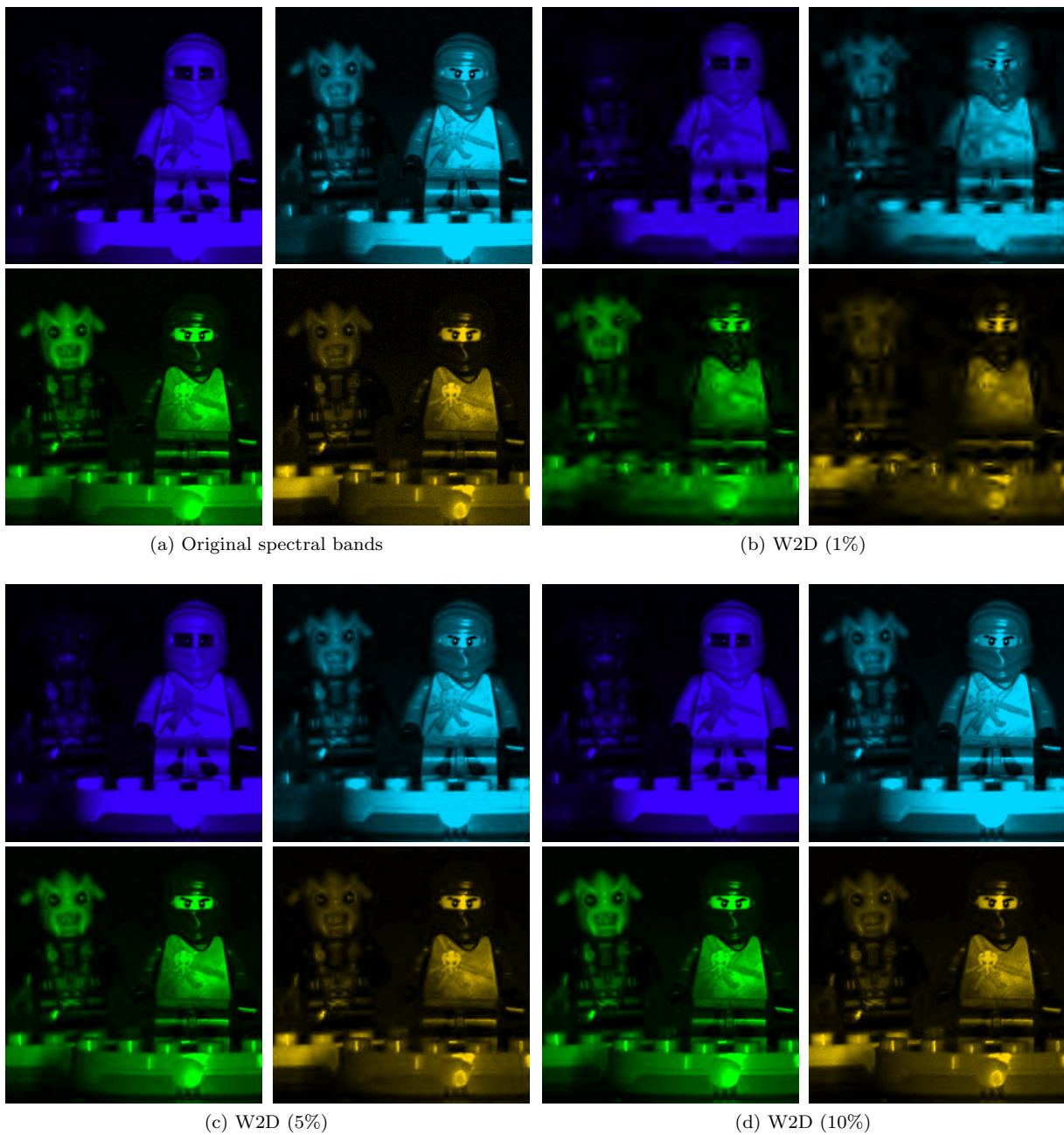
Figure 1.9: Sparse hyperspectral signal representation using the 2D Wavelet function. The spectral bands in (a) are represented using (b) 1% (c) 5%, and (d) 10% of the sparse representation coefficients.

(a) Original spectral bands   (b) Kronecker (1%)

(c) Kronecker (5%)   (d) Kronecker (10%)

Figure 1.10: Sparse hyperspectral signal representation using the Kronecker (DCT-2D Wavelet) function. The spectral bands in (a) are represented using (b) 1% (c) 5%, and (d) 10% of the sparse representation coefficients.
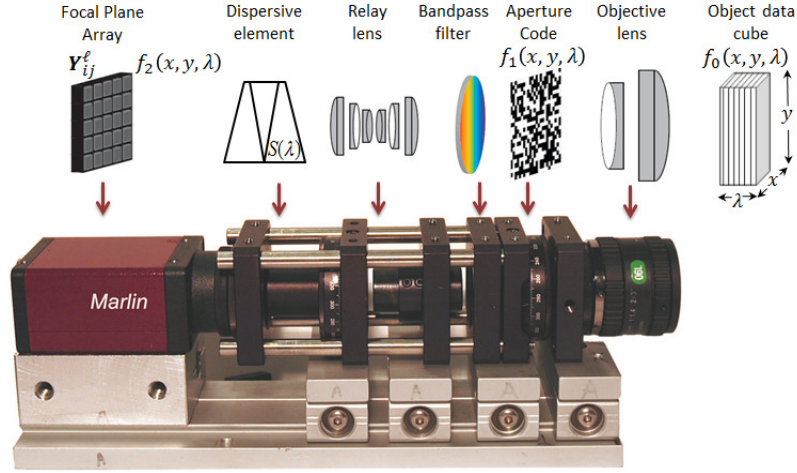
Figure 1.11: Compressive CASSI sensor components developed at Duke University.
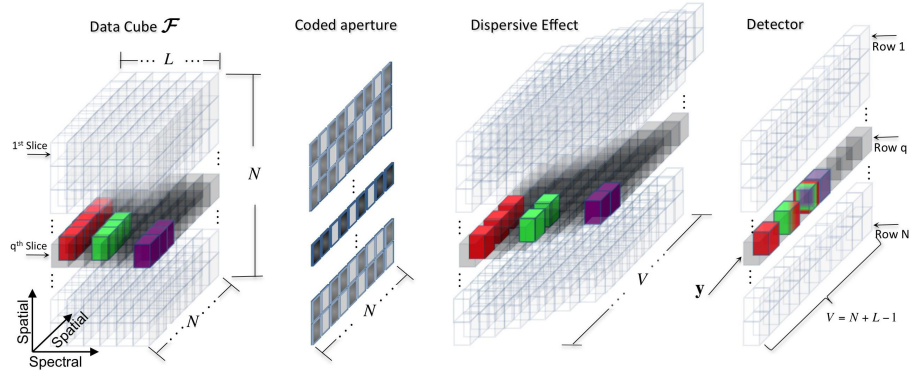
Figure 1.12: Illustration of the spectral data flow in CASSI. The qth slice of the data cube $\mathcal{F}$ with 11 spectral components is coded by a row of the code aperture $\tilde{\mathbf{t}}$ and dispersed by the prism. The detector captures the intensity $\mathbf{y}$ by integrating the coded light.

the structure of the sensing matrix $\mathbf{A} \triangleq \mathbf{H\Psi}$ as it ultimately determines the attainable quality of reconstruction. While the optical architecture in CASSI partially imposes a well defined sparse structure to the sensing matrix $\mathbf{A}$, the coded apertures used in each measurement shot, ultimately determine the structure of $\mathbf{A}$. The objective in CASSI is thus to optimally design the set of coded apertures so as to forge a structure on $\mathbf{A}$ that minimizes the number of FPA snapshots while attaining the highest quality reconstruction. To this end, this project explores the interplay between the Restricted Isometry Property and the set of coded apertures used in CASSI.

Chapter 2

Coded Aperture Optimization for Spectrally Agile Compressive Imaging

2.1 Introduction

Coded Aperture Snapshot Spectral Imaging (CASSI), first introduced in [?], is a remarkable imaging architecture that allows capturing spectral imaging information of a 3D cube with just a single 2D measurement of the coded and spectrally dispersed source field. The CASSI architecture has been studied extensively in [?, ?]. It turns out that the coded measurements are mathematically equivalent to compressive projections which are at the heart of the emerging field of compressive sensing (CS). In CS, traditional sampling is replaced by measurements of inner products with random vectors. In CASSI, the random projections are equivalent to spectrally dispersed coded fields that are integrated (projected) by array detectors with broad spectral response. The spectral images are then reconstructed by solving an inverse problem such as a linear program or a greedy pursuit in a basis where the under sampled signals admit sparse representations. The key idea in CS reconstruction is the realization that most signals encountered in practice are sparse in some domain and the theory of CS exploits such sparsity to dictate that far fewer sampling resources than traditional approaches are needed [?, ?, ?].

Spectral image cubes are particularly well suited for sparse representation as images across different wavelengths exhibit strong correlation [?, ?, ?]. More formally, suppose a hyperspectral signal $\mathbf{F} \in \mathcal{R}^{N \times M \times L}$, or its vector representation $\mathbf{f} \in \mathcal{R}^{N \cdot M \cdot L}$, is S sparse on some basis $\Psi = \Psi_1 \otimes \Psi_2 \otimes \Psi_3$, such that $\mathbf{f} = \Psi\theta$ can be approximated by a linear combination of S vectors from Ψ with $S \ll (N \cdot M \cdot L)$. The operator $\otimes$ is the Kronecker product and Ψ is the Kronecker basis representation of $\mathbf{f}$[?]. $N \times M$ represents the spatial dimensions and L is the spectral depth of the image cube. The theory of compressive sensing shows that $\mathbf{f}$ can be recovered from m random projections with high probability when $m \lesssim S \log(N \cdot M \cdot L) \ll (N \cdot M \cdot L)$. The dimension of the Kronecker basis set Ψ is $\mathcal{R}^{N \cdot M \cdot L \times N \cdot M \cdot L}$ such that $\Psi_1 \in \mathcal{R}^{N \times N}$, $\Psi_2 \in \mathcal{R}^{M \times M}$ and $\Psi_3 \in \mathcal{R}^{L \times L}$. The projections are given by $\mathbf{g} = \mathbf{H}\Psi\theta$, where $\mathbf{H}$ is an $N(M + L - 1) \times (N \cdot M \cdot L)$ random measurement matrix with its rows incoherent with the columns of Ψ. Commonly used random measurement matrices for CS are random Gaussian matrices ($\mathbf{H}_{ij} \in \{\mathcal{N}(0, 1/n)\}$), Rademacher matrices ($\mathbf{H}_{ij} \in \{\pm 1/n^{1/2}\}$) and partial Fourier matrices. The random projection matrices in CASSI are realized by the coded aperture and the dispersive element. Figure 2.1 illustrates the principles behind CASSI, where a $6 \times 6 \times 8$ spectral data cube with 16 non zero spectral components is depicted. The spectral components are coded by a coded aperture where the white pixels block the impinging light and black pixels permit light to pass through. A prism disperses the coded light and a detector integrates the intensity of the wave light. The pixel measurements at the detector are proportional to the linear combinations of the coded spectral components.

This chapter extends the CASSI spectral imaging concept to a spectral imaging architecture admitting
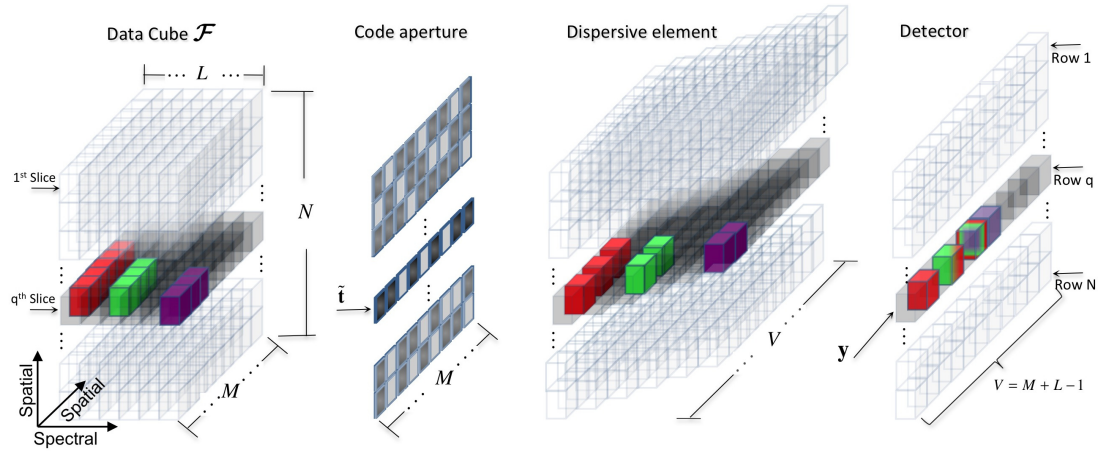
Figure 2.1: The principles behind CASSI imaging. A $6 \times 6 \times 8$ spectral data cube with 16 non zero spectral components is coded by the coded aperture and dispersed by the prism. The detector integrates the intensity of the resulting light wave. Each pixel at the detector contains a coded linear combination of the spectral information from the respective data cube slice.

multiple measurement shots. The multiple measurements are attained as separate FPA measurements, each with a distinct coded aperture that remains fixed during the integration time of the detector. There are several advantages to multiple shots [**?**]. First, the number of compressive measurements in CASSI may not meet the minimum needed for adequate reconstruction. Compressive sensing dictates that the number of measurements must be in excess of $S \log(N \cdot M \cdot L)$. Failure to collect a sufficient number of measurements leads to a severely underdetermined inverse problem and to inadequate signal reconstruction. With each shot, CASSI invariably collects $N \cdot M$ additional measurements regardless of the spectral depth and sparsity of the source. For spectrally rich scenes or very detailed spatial scenes, a single shot CASSI measurement may not provide a sufficient number of compressive measurements. Increasing the number of measurement shots will multiply the number of measurements, thus rapidly overcoming such limitations.

A second advantage to multiple shots is that spectral selectivity can be attained by coded aperture design. Notably, the coded aperture patterns can be designed so as to maximize the information content on a pre-specified subset of spectral bands of particular interest. Spectral selectivity is a characteristic of interest in many applications, including wide-area airborne surveillance, remote sensing, and tissue spectroscopy in medicine. The optimal spectral bands in airborne surveillance, for instance, depend on atmospheric conditions, time of day, the targets of interest, and the background against which the targets are viewed. The development of dynamically programable multi-spectral imaging sensors are of significant interest, particularly for their use in small unmanned aerial vehicles. Similarly, spectrally selective imaging is becoming widely used in medicine. Spectral imaging of the retina, for instance, offers a route to non-invasive characterization of the biochemical and metabolic processes within the retina retinopathies [**?**]. In the applications described above, and in many other applications, the spectral signatures of interest live in a spectral band subspace. Efforts placed on acquiring the entire spectral image cube, to then throw away a large portion of this data is wasteful in many regards. This Chapter focuses on overcoming these inefficiencies, by developing an optimization framework for the design of coded apertures for spectrally selective imaging.

In order to fully exploit the advantages of multishot coded apertures, this Chapter also develops a new model describing the coded aperture optical system. The original CASSI model describes the output of the system as a matrix operation acting on the input source field, where all the optical effects are implicitly embedded in the matrix operation. The CASSI model derived here describes the output of the system as a function of a "code-aperture vector" that explicitly acts on a "reordered" input source. In particular, a vector representation of a slice of the data cube is re-ordered into a matrix
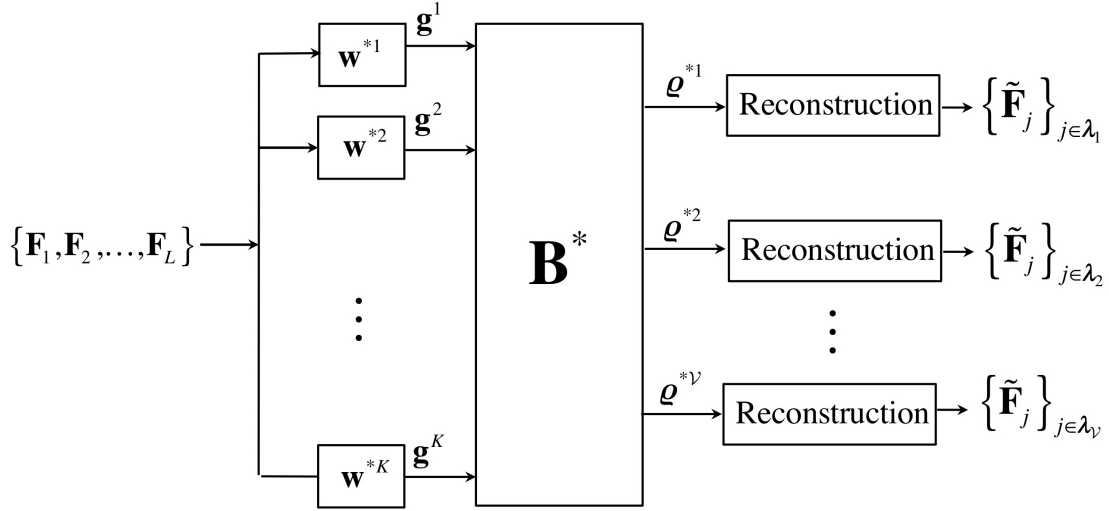
Figure 2.2: The CAASI system seen as a multi-channel filter bank. A set of measurements $\{\mathbf{g}^i\}$ are captured with a corresponding set of optimal aperture codes $\{\mathbf{w}^1, \ldots, \mathbf{w}^K\}$. The mapping $\mathbf{B}$ reorders the K sets of measurements $\{\mathbf{g}^i\}$ into the $\mathcal{V}$ sets $\{\boldsymbol{\varrho}^i\}$. Each subset $\{\boldsymbol{\varrho}^i\}$ is sufficient to independently reconstruct the desired spectral band subset $\{\tilde{\mathbf{F}}_{\lambda_i}\}$.

structure, implicitly accounting for the spectral shearing operator of the CASSI system. The reordering operator, in turn, decouples the code-aperture effects of CASSI from the spectral shearing, thus allowing the representation of the output of the CASSI system as a simple matrix multiplication of the reordered input data with a vector whose elements are the coded aperture variables to be optimized. In this manner, the coded aperture optimization problem is shown to be analogous to a multi-channel digital filter bank optimization problem where the filter coefficients represent the aperture codes and, consequently, the optimization is constrained to produce binary-valued outputs. The solution to the optimization problem at hand is made feasible by the new CASSI system representation. Using the resultant optimal coefficients, a filter bank decomposition of the data cube can be realized such that it is possible to assemble a reduced set of compressive measurements which are sufficient to reconstruct a desired subset of spectral bands, and at the same time attain higher signal to noise ratio. Figure 2.2 illustrates this concept where a set of K measurements $\{\mathbf{g}^i\}$ are taken with a corresponding K set of optimal aperture codes $\{\mathbf{w}^i\}$ where i indexes the ith measurement. The mapping $\mathbf{B}$ reorders the set of measurements $\{\mathbf{g}^i\}$ into the $\mathcal{V} \leq K$ sets $\{\boldsymbol{\varrho}^i\}$ containing only information of the spectral bands given by λ_i. Each subset $\{\boldsymbol{\varrho}^i\}$ is sufficient to independently reconstruct the desired spectral band subset $\{\tilde{\mathbf{F}}_{\lambda_i}\}$. The new coded aperture agile spectral imaging (CAASI) system described in this Chapter allows multiple measurement shots and, consequently, it has the aforementioned advantages over CASSI. The new capabilities, however, come at the expense of more complexity in the hardware implementation. Multishot measurements can be attained by successively shifting, along the horizontal axis, the fixed coded aperture in CASSI. A novel piezo-electrical implementation of this approach is described in [?, ?]. An approach more suitable for dynamic selectivity in real-time is to implement the time-varying aperture codes on a spatial light modulator [?, ?, ?, ?]. Device implementation, calibration, wavelength range of operation, and other hardware considerations are critical but fall outside the scope of this Chapter. These will be considered in depth in a separate publication. The methods developed here are mathematical in nature and thus are applicable on any hardware platform capable of acquiring multiple shots, each with a distinct aperture code pattern.

2.2 Coded Aperture Characterization in CASSI

The coded aperture single shot spectral imaging system is depicted in Fig. 2.3 [?]. The coding is realized by the coded aperture $T(x, y)$ as applied to the spatio-spectral density source $f_0(x, y; \lambda)$ where (x, y) are the spatial coordinates and λ is the wavelength resulting in the coded field $f_1(x, y, \lambda)$. The coded
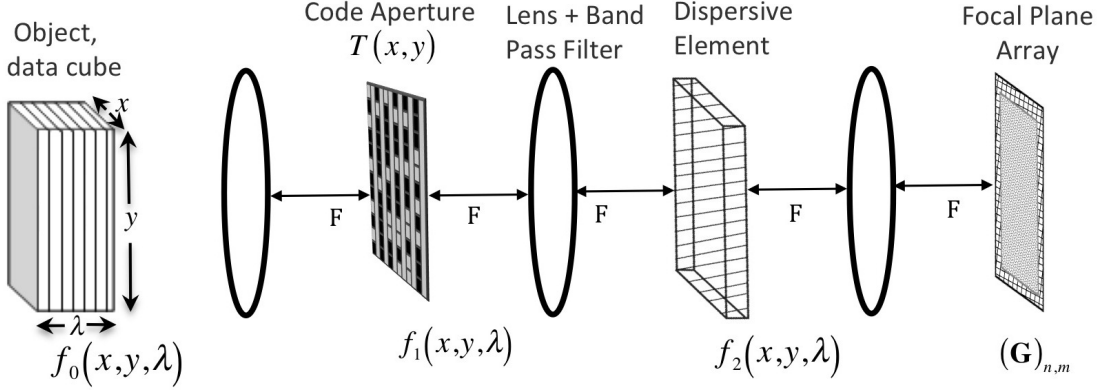
Figure 2.3: Representation of the CASSI.

density is spectrally dispersed by a dispersive element before it impinges on the focal plane array (FPA) as $f_2(x, y, \lambda)$,

$$f_2(x, y, \lambda) = \int \int T(x', y') f_0(x', y', \lambda) h(x' - \alpha\lambda - x, y' - y) dx' dy' \qquad (2.1)$$

where $T(x', y')$ is the transmission function representing the coded aperture, $h(x' - \alpha\lambda - x, y' - y)$ is the optical impulse response of the system, and $\alpha\lambda$ is the dispersion induced by the prism assuming a linear dispersion. Each spectral slice of the data cube $f_0(x, y; \lambda)$ is thus spatially modulated by the coded aperture and dispersed by the dispersive element[?]. The compressive measurements across the FPA are realized by the integration of the field $f_2(x, y, \lambda)$ over the detector's spectral range sensitivity. The source $f_0(x', y', \lambda)$ can be written in discrete form as $(\mathbf{F}_k)_{nm}$ where n and m index the spatial coordinates, and k determines the kth spectral plane. Assuming that the band pass filter of the instrument limits the spectral components between λ_1 and λ_2 and the side length of the square detector pixel is Δ_d, the number of resolvable bands L is limited by $L = \alpha\frac{\lambda_2 - \lambda_1}{\Delta_d}$. The spectral resolution is limited by $\frac{\Delta_d}{\alpha}$. Additionally, it is assumed that the side length of the coded aperture square pixel Δ_c satisfies $k\Delta_c = \Delta_d$, where $k \geq 1$ is an integer. The horizontal and vertical spatial resolutions are thus limited by Δ_d. The height N of the resolvable data cube is limited by $N = \min(\frac{U_h}{k\Delta_c}, \frac{V_h}{\Delta_d})$ where U_h and V_h are the vertical physical dimensions of the coded aperture and the detector respectively. The width M of the resolvable data cube is limited by $M = \min(\frac{U_w}{k\Delta_c}, \frac{V_w}{\Delta_d} - L + 1)$ where U_w and V_w are the horizontal physical dimensions of the coded aperture and the detector respectively. Following the mathematical model in [?], the coding is realized by an aperture pattern $(\mathbf{T})_{nm}$.

The compressed sensing measurements at the focal plane array can be written in the following matrix form:

$$(\mathbf{G})_{nm} = \sum_{k=1}^{L} (\mathbf{F}_k)_{n,m+k} (\mathbf{T})_{n,m+k} + (\boldsymbol{\omega})_{n,m} \qquad (2.2)$$

where $\boldsymbol{\omega}$ represents white noise, L is the number of spectral bands, and n, m index the pixels on the detector. A typical example of the measurement process using (2.2) is shown in Fig. 2.1. The expression in (2.2) can be expressed as

$$\mathbf{g} = \mathbf{Hf} + \boldsymbol{\omega} = \mathbf{H\Psi\theta} + \boldsymbol{\omega} \qquad (2.3)$$

where $\mathbf{g}$ and $\mathbf{f}$ are vector representations of $\mathbf{G}$ and $\mathbf{F}$, respectively [?]. These vector representations will be described shortly. $\mathbf{H}$ is the projection matrix that takes into account the effects of the coded aperture and the dispersive element. Ψ is a Kronecker basis representation, and $\boldsymbol{\theta}$ is a sparse coefficient vector representing $\mathbf{f}$. The characteristics of $\mathbf{H}$ in relation to incoherence and the restricted isometry property (RIP), needed for signal reconstruction in a set of undetermined system of linear equations are studied in [?]. If the aperture code pattern is fixed and only one snap-shot is detected, the resultant spectral imager is the so-called single disperser, or single-shot, CASSI architecture [?]. In this case, the entire 3-D multispectral image cube is compressed into a single 2-D compressive image measurement at the FPA. The spectral image cube $\mathbf{f}$ can be reconstructed by solving the optimization problem
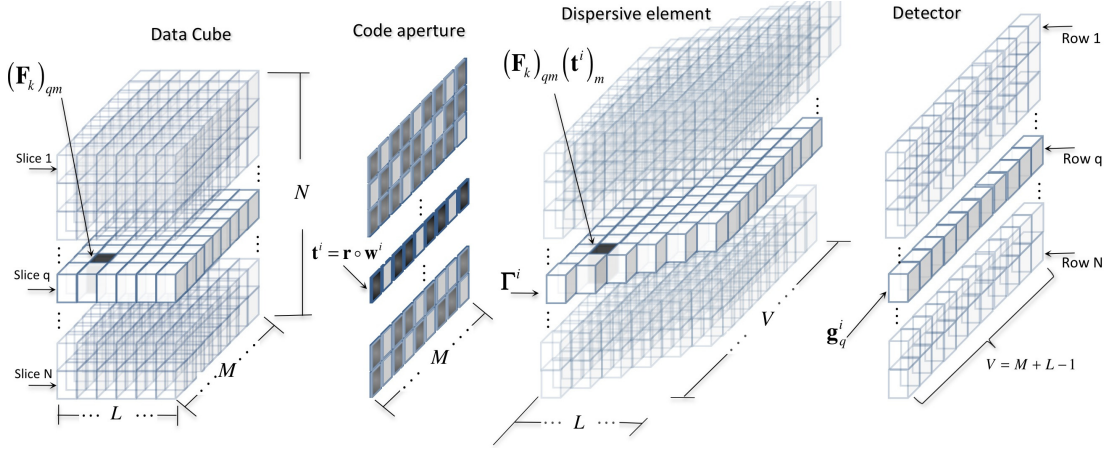
Figure 2.4: Model equations for a row measurement. A slice of the data cube $\mathbf{f}_q$ impinges on a row of the coded aperture $\mathbf{t}^i = \mathbf{r} \circ \mathbf{w}^i$ to produce the coded slice $\boldsymbol{\mathcal{W}}^i \boldsymbol{\mathcal{R}}^i \mathbf{f}_q$. The elements of the coded slice are reordered into the matrix $\boldsymbol{\Gamma}^i$. The detector output $\mathbf{g}_q^i = \boldsymbol{\Gamma}^i \mathbf{u}_L$ sums the columns of $\boldsymbol{\Gamma}^i$.

$\hat{\mathbf{f}} = \Psi\{\mathrm{argmin}_{\theta'} \|\mathbf{g} - \mathbf{H}\Psi\theta'\|_2^2 + \tau\|\theta'\|_1\}$ where $\tau > 0$ is a regularization parameter that balances the conflicting tasks of minimizing the least square of the residuals while, at the same time, yielding a sparse solution. Several algorithms exist in the compressive sensing literature to solve this inverse problem [?, ?, ?, ?].

$\mathbf{H}$ in (2.3) is an $N \cdot (M + L - 1) \times N \cdot M \cdot L$ matrix mapping the vector $\mathbf{f}$, which indexes the 3D data cube, into the vector $\mathbf{g}$. Note from (2.2) and (2.3) that the matrix $\mathbf{H}$ embeds both, the coded aperture $\mathbf{T}$ and the shifting operation of the dispersive element. Since the aperture code is hidden in $\mathbf{H}$ and since it is not directly observed in (2.2) and (2.3), its optimization is difficult using this CASSI formulation. Given that this analysis only considers the dispersive and the coded aperture effects, the matrix $\mathbf{H}$ is binary; however, due to non-linearity in the dispersive element, non ideal optical instruments and misalignments between the detector pixels and the spatial light modulator, these matrices have real values in practice [?]. For the purposes of this Chapter a binary $\mathbf{H}$ is used. Additionally, the model used does not consider noise. The modifications on $\mathbf{H}$ to address the physical limitations of the optical system can be readily done but omitted here in order to better illustrate the aperture code optimization problem.

Since the dispersive element shifts the propagating light along the horizontal dimension only, the spectral coding in CASSI is independent from one row to another. Hence, it is possible to construct an aperture code model for just one row of the measurement matrix, which is then replicated for all rows of the detector. To this end, define the vector $\mathbf{f}_q$ that indexes one slice of the data cube $(\mathbf{F}_k)_{nm}$ when the index n is fixed to q. More specifically,

$$(\mathbf{f}_q)_{(k-1)\cdot M+m} = (\mathbf{F}_k)_{qm}, \qquad \text{for} \quad m = 1, \ldots, M \quad k = 1, \ldots, L. \tag{2.4}$$

Note that the elements of $\mathbf{f}_q$ are the only elements of the source $\mathbf{f}$ having an impact on the qth row of $\mathbf{G}$. Let the qth row of $\mathbf{G}$ be $\mathbf{g}_q$. The projection of $\mathbf{f}_q$ into $\mathbf{g}_q$ is then represented as

$$\mathbf{g}_q = \mathbf{H}_q \mathbf{f}_q. \tag{2.5}$$

for $q = 1, \ldots, N$. Figure 2.4 illustrates the various vector representations in (2.4) and (2.5) of the source data cube. Since the spectral coding along rows of $\mathbf{G}$ are mutually independent, the vectors $\mathbf{g}_q$, can be arranged as in (2.3) where $\mathbf{g}$ and $\mathbf{H}$ are unfolded showing the mutual independence of the row

measurements as

$$
\overbrace{\begin{bmatrix} \mathbf{g}_1 \\ \vdots \\ \mathbf{g}_q \\ \vdots \\ \mathbf{g}_N \end{bmatrix}}^{\mathbf{g}} = \overbrace{\begin{bmatrix} \mathbf{H}_1 & \mathbf{0} & \cdots & & \mathbf{0} \\ \mathbf{0} & \ddots & \ddots & & \vdots \\ \vdots & \ddots & \mathbf{H}_q & & \\ & & & \ddots & \\ \mathbf{0} & \cdots & & & \mathbf{H}_N \end{bmatrix}}^{\mathbf{H}} \overbrace{\begin{bmatrix} \mathbf{f}_1 \\ \vdots \\ \mathbf{f}_q \\ \vdots \\ \mathbf{f}_N \end{bmatrix}}^{\mathbf{f}}
\tag{2.6}
$$

where the matrices $\mathbf{0}$ have $(M+L-1) \times M \cdot L$ zero elements, the NML-long vector $\mathbf{f} = \begin{bmatrix} \mathbf{f}_1^T & \mathbf{f}_2^T & \ldots & \mathbf{f}_N^T \end{bmatrix}^T$ is the concatenation of the vectors $\mathbf{f}_q$ in (2.4), and the vector $\mathbf{g} = \begin{bmatrix} \mathbf{g}_1 & \mathbf{g}_2 & \ldots & \mathbf{g}_N \end{bmatrix}^T$ is the concatenation of the row vectors $\mathbf{g}_q$ representing the qth row at the detector. The matrix $\mathbf{H}_q$ represents the effect of the dispersive element, the coded aperture, and the integration on the detector for the qth row of the measurement matrix $\mathbf{G}$. The $\mathbf{H}_q$ matrix is given by

$$
\mathbf{H}_q = \begin{bmatrix} \mathrm{diag}\{(\mathbf{T})_{q,1}, \ldots, (\mathbf{T})_{q,M}\} & \mathbf{0}_{1 \times M} & \cdots & \mathbf{0}_{1 \times M} \\ \mathbf{0}_{1 \times M} & \mathrm{diag}\{(\mathbf{T})_{q,1}, \ldots, (\mathbf{T})_{q,M}\} & \cdots & \vdots \\ \vdots & \mathbf{0}_{1 \times M} & \ddots & \vdots \\ \vdots & \vdots & \ddots & \mathbf{0}_{1 \times M} \\ \mathbf{0}_{1 \times M} & \mathbf{0}_{1 \times M} & & \mathrm{diag}\{(\mathbf{T})_{q,1}, \ldots, (\mathbf{T})_{q,M}\} \end{bmatrix}
\tag{2.7}
$$

where $\mathrm{diag}\{(\mathbf{T})_{q,1}, (\mathbf{T})_{q,2}, \ldots, (\mathbf{T})_{q,M}\}$ is an $M \times M$ diagonal matrix with the elements of the qth row of $\mathbf{T}$ in its diagonal. Observe that the specific structure of $\mathbf{H}_q$ determines the structure of $\mathbf{H}$ in (2.6) and (2.3). In order to separate the effects of the various optical elements, the representation $\mathbf{H}_q$ can be expressed as $\mathbf{H}_q = \mathbf{D}\boldsymbol{\mathcal{T}}$, where the matrix $\mathbf{D}$ represents the mapping operation of the dispersive element. The matrix $\mathbf{D}$ has at most L non zero elements in each row. The specific structure of the $(M+L-1) \times ML$ matrix $\mathbf{D}$ is given by

$$
\mathbf{D} = \begin{bmatrix} \mathbf{I}_M & \mathbf{0}_{1 \times M} & \cdots & \mathbf{0}_{1 \times M} \\ \mathbf{0}_{1 \times M} & \mathbf{I}_M & \cdots & \mathbf{0}_{1 \times M} \\ \vdots & \vdots & \ddots & \vdots \\ \mathbf{0}_{1 \times M} & \mathbf{0}_{1 \times M} & & \mathbf{I}_M \end{bmatrix}
\tag{2.8}
$$

where $\mathbf{I}_M$ is an $M \times M$ identity matrix and $\mathbf{0}_{1 \times M}$ are zero-valued row vectors. The matrix $\boldsymbol{\mathcal{T}}$ represents the effect of the coded aperture $\mathbf{T}$ on $\mathbf{f}_q$ and has the following structure

$$
\boldsymbol{\mathcal{T}} = \mathbf{I}_L \otimes \mathrm{diag}\{(\mathbf{T})_{q,1}, (\mathbf{T})_{q,2}, \ldots, (\mathbf{T})_{q,M}\}
\tag{2.9}
$$

where $\mathbf{I}_L$ is an $L \times L$ identity matrix. $\boldsymbol{\mathcal{T}}$ is thus an $M \cdot L \times M \cdot L$ diagonal matrix whose elements are L repetitions of the elements in the qth row of $\mathbf{T}$. The mapping of $\mathbf{f}_q$ into $\mathbf{g}_q$ in (2.5) is then written as

$$
\mathbf{g}_q = \mathbf{D}\boldsymbol{\mathcal{T}}\mathbf{f}_q.
\tag{2.10}
$$

The vector representation in (2.10), characterizing CASSI, will be critical in formulating the aperture code optimization problem described in the following sections.

2.3 Coded Aperture Agile Spectral Imaging System (CAASI)

The spectral selectivity is determined by the aperture codes used in each shot. The mathematical model of the ith measurement shot of the CAASI system is identical to that shown in (2.2) for the CASSI system

$$
(\mathbf{G}^i)_{n,m} = \sum_{k=1}^{L} (\mathbf{F}_k)_{n,m+k} (\mathbf{T}^i)_{n,m+k} + (\boldsymbol{\omega}^i)_{n,m}
\tag{2.11}
$$

for $i = \{1, \ldots, K\}$, where K is the number of shots, except that the ith aperture code pattern $\mathbf{T}^i$ used to sense $\mathbf{G}^i$ is different from one shot to another. Notice that the coded aperture $\mathbf{T}^i$ can be seen as

two separate coded apertures applied in tandem. The first coded aperture $\mathbf{R}$ is a random binary code necessary to attain randomized measurement in CASSI. The second coded aperture $\mathbf{W}^i$ is the ith code optimized to achieve a specific spectral band selectivity. $\mathbf{T}^i$ is thus represented as the Hadamard product $(\mathbf{T}^i)_{n,m} = (\mathbf{R})_{n,m}(\mathbf{W}^i)_{n,m}$ where $\mathbf{W}^i$ is the time varying element in each CAASI measurement. In matrix form, the CAASI system of equations results in

$$\mathbf{g}^i = \mathbf{H}^i\mathbf{f} + \boldsymbol{\omega}^i \quad i \in 1,\dots,K. \tag{2.12}$$

As in the single shot CASSI system, the row measurements $\mathbf{g}_q^i$ are decoupled from one another such that the $\mathbf{H}^i$ matrices in (2.12) are block diagonal. The qth row of $\mathbf{G}^i$ is then given by $\mathbf{g}_q^i = \mathbf{H}_q^i\mathbf{f}_q$, or equivalently

$$\mathbf{g}_q^i = \mathbf{D}\boldsymbol{\mathcal{T}}^i\mathbf{f}_q. \tag{2.13}$$

Note in (2.13) that the source vector $\mathbf{f}_q$ does not contain the index i, since we assume that the source remains stationary during the time interval when the K shots are measured. The only difference at this point, between the static case of the CASSI equation in (2.10) and the CAASI equation in (2.13), is that the matrix $\boldsymbol{\mathcal{T}}^i$ changes with each shot. The matrices $\boldsymbol{\mathcal{T}}^i$ have the structure given in (2.9), but in this case, the qth row of $\mathbf{T}^i$ can be expressed as $\mathbf{t}^i = \mathbf{r} \circ \mathbf{w}^i$ where $\circ$ denotes the Hadamard multiplication of $\mathbf{r}$ and $\mathbf{w}^i$, the qth row of the matrices $\mathbf{R}$ and $\mathbf{W}^i$, respectively. Figure 2.4 depicts the interaction of the vector $\mathbf{t}^i$ with the incoming wave $\mathbf{f}_q$. In the static case of (2.9), $\mathbf{T}$ does not have a time varying term and thus $\mathbf{t} = \mathbf{r}$. The matrix $\boldsymbol{\mathcal{T}}^i$ can be expressed as $\boldsymbol{\mathcal{T}}^i = \mathbf{I}_L \otimes \mathrm{diag}\{(\mathbf{w}^i)_1(\mathbf{r})_1,\dots,(\mathbf{w}^i)_M(\mathbf{r})_M\}$. Using the product property of the Kronecker product, $\boldsymbol{\mathcal{T}}^i$ is written as

$$\boldsymbol{\mathcal{T}}^i = \underbrace{\left(\mathbf{I}_L \otimes \mathrm{diag}\{(\mathbf{w}^i)_1,\dots,(\mathbf{w}^i)_M\}\right)}_{\boldsymbol{\mathcal{W}}^i}\underbrace{\left(\mathbf{I}_L \otimes \mathrm{diag}\{(\mathbf{r})_1,\dots,(\mathbf{r})_M\}\right)}_{\boldsymbol{\mathcal{R}}} \tag{2.14}$$

where $\boldsymbol{\mathcal{W}}^i$ represents the component of the coded aperture $\mathbf{w}^i$ and $\boldsymbol{\mathcal{R}}^i$ reflects the effect of $\mathbf{r}$. While the random matrix $\boldsymbol{\mathcal{R}}$ is not tunable in this design, the matrix $\boldsymbol{\mathcal{W}}^i$ contains weight elements of the coded aperture that will be optimized. $\boldsymbol{\mathcal{R}}$ is attained via Bernoulli random realizations, however, random matrices such as a scrambled Hadamard can be used to construct this random component. Using (2.14) in (2.13) we obtain $\mathbf{g}_q^i = \mathbf{D}\boldsymbol{\mathcal{W}}^i\boldsymbol{\mathcal{R}}\mathbf{f}_q$. Letting $\boldsymbol{\rho} = \boldsymbol{\mathcal{R}}\mathbf{f}_q$ be the effect of the vector $\mathbf{r}_q$ on the source $\mathbf{f}_q$, then $\mathbf{g}_q^i$ can be written as

$$\mathbf{g}_q^i = \mathbf{D}\boldsymbol{\mathcal{W}}^i\boldsymbol{\rho}. \tag{2.15}$$

Making some matrix indexes manipulations, Eq. (2.15) can be written as

$$\mathbf{g}_q^i = \boldsymbol{\Gamma}^i\mathbf{u}_L \tag{2.16}$$

where $\mathbf{u}_L$ is the L long vector $\mathbf{u}_L = [1,\dots,1]^T$ and the matrix $\boldsymbol{\Gamma}^i$ is given by

$$\boldsymbol{\Gamma}^i = \begin{bmatrix} \rho_1(\mathbf{w}^i)_1 & \rho_2(\mathbf{w}^i)_2 & \cdots & \rho_L(\mathbf{w}^i)_L & \cdots & \rho_M(\mathbf{w}^i)_M & 0 & \cdots & 0 \\ 0 & \rho_{M+1}(\mathbf{w}^i)_1 & \cdots & \rho_{M+L-1}(\mathbf{w}^i)_{L-1} & \cdots & \rho_{2M-1}(\mathbf{w}^i)_{M-1} & \rho_{2M}(\mathbf{w}^i)_M & \cdots & 0 \\ 0 & 0 & \ddots & \rho_{2M+L-2}(\mathbf{w}^i)_{L-2} & \cdots & \rho_{3M-2}(\mathbf{w}^i)_{M-2} & \rho_{3M-1}(\mathbf{w}^i)_{M-1} & \cdots & 0 \\ \vdots & \vdots & & \vdots & \cdots & \vdots & \vdots & \ddots & \\ 0 & 0 & 0 & \rho_{(L-1)M+1}(\mathbf{w}^i)_1 & \cdots & \rho_{LM-(L-1)}(\mathbf{w}^i)_{M-L+1} & & \cdots & \rho_{LM}(\mathbf{w}^i)_M \end{bmatrix}^T \tag{2.17}$$

where ρ_j is the jth element of $\boldsymbol{\rho}$. It can be observed that the $(\mathbf{w}^i)_l$ terms have a circular shift on l within each row of $\boldsymbol{\Gamma}^i$. Additionally, only L pixels in the detector are affected by a point source in the data cube. Hence, only L elements of $\mathbf{w}^i$ in (2.17) need to be optimized. Define the L-long sub-segments of $\mathbf{w}^i$ as $\overline{\mathbf{w}}^i$, such that $\mathbf{w}^i$ is formed by the modulo repetition operator

$$(\mathbf{w}^i)_m = (\overline{\mathbf{w}}^i)_{mod(m,L)} \qquad \text{for} \quad m = 1,\dots,M \quad \text{and} \quad L < M. \tag{2.18}$$

Equation (2.18) can be expressed in matrix form as

$$\mathbf{w}^i = \mathbf{u}_{M'} \otimes \overline{\mathbf{w}}^i \tag{2.19}$$

33

where $M' = \frac{M}{L}$ is the length of the one element vector $\mathbf{u}_{M'}$. If the integral part of $\frac{M}{L}$ is not an integer then the first $L\lfloor\frac{M}{L}\rfloor$ elements of $\mathbf{w}^i$ are given by (2.19) and the remaining by, $(\mathbf{w}^i)_m = (\mathbf{w}^i)_{m-L}$, for $m = L\lfloor\frac{M}{L}\rfloor + 1, \ldots, M$. Reordering the elements of $\mathbf{\Gamma}^i$ in (2.17) such that the $(\mathbf{w}^i)_l$ terms appear in ascending order, and using the periodicity of $\mathbf{w}^i$ given in (2.18), we obtain

$$\overline{\mathbf{\Gamma}}^i = \begin{bmatrix} \rho_1(\overline{\mathbf{w}}^i)_1 & \rho_{M+1}(\overline{\mathbf{w}}^i)_1 & \cdots & \rho_{(L-1)M+1}(\overline{\mathbf{w}}^i)_1 & \cdots & \rho_{LM-(L-1)}(\overline{\mathbf{w}}^i)_1 & 0 & \cdots & 0 \\ 0 & \rho_2(\overline{\mathbf{w}}^i)_2 & \cdots & \rho_{(L-2)M+2}(\overline{\mathbf{w}}^i)_2 & \cdots & \rho_{(L-1)M-(L-2)}(\overline{\mathbf{w}}^i)_2 & \rho_{LM-(L-2)}(\overline{\mathbf{w}}^i)_2 & \cdots & 0 \\ 0 & 0 & \ddots & \rho_{(L-3)M+3}(\overline{\mathbf{w}}^i)_3 & \cdots & \rho_{(L-2)M-(L-3)}(\overline{\mathbf{w}}^i)_3 & \rho_{(L-1)M-(L-3)}(\overline{\mathbf{w}}^i)_3 & \cdots & 0 \\ \vdots & \vdots & & \vdots & \cdots & \vdots & \vdots & \ddots & \\ 0 & 0 & 0 & \rho_L(\overline{\mathbf{w}}^i)_L & \cdots & \rho_M(\overline{\mathbf{w}}^i)_L & \rho_{2M}(\overline{\mathbf{w}}^i)_L & \cdots & \rho_{LM}(\overline{\mathbf{w}}^i)_L \end{bmatrix}^T. \quad (2.20)$$

Note that the matrix product $\mathbf{\Gamma}^i\mathbf{u}_L$ in (2.16) and the product $\overline{\mathbf{\Gamma}}^i\mathbf{u}_L$ of the reordered matrices in (2.20) are identical. Hence (2.16) can be rewritten as $\mathbf{g}_q^i = \overline{\mathbf{\Gamma}}^i\mathbf{u}_L$. The expression for $\mathbf{g}_q^i$ can be further simplified by factoring out the elements $\overline{\mathbf{w}}^i$ in (2.20) leading to

$$\mathbf{g}_q^i = \mathbf{X}\,\overline{\mathbf{w}}^i \qquad (2.21)$$

where

$$\mathbf{X} = \begin{bmatrix} \rho_1 & \rho_{M+1} & \cdots & \rho_{(L-1)M+1} & \cdots & \rho_{LM-(L-1)} & 0 & \cdots & 0 \\ 0 & \rho_2 & \cdots & \rho_{(L-2)M+2} & \cdots & \rho_{(L-1)M-(L-2)} & \rho_{LM-(L-2)} & \cdots & 0 \\ 0 & 0 & \ddots & \rho_{(L-3)M+3} & \cdots & \rho_{(L-2)M-(L-3)} & \rho_{(L-1)M-(L-3)} & \cdots & 0 \\ \vdots & \vdots & & \vdots & \cdots & \vdots & \vdots & \ddots & \\ 0 & 0 & \cdots & \rho_L & \cdots & \rho_M & \rho_{2M} & \cdots & \rho_{L(M)} \end{bmatrix}^T \qquad (2.22)$$

is a matrix containing the spectral source elements multiplied by the random component of the aperture code, which are then spectrally shifted. Equation (2.21) is a compact expression for $\mathbf{g}_q^i$, where $\overline{\mathbf{w}}^i$ describes the effect of the optimizable part of the coded aperture. The effect of the others optical elements on the data cube is accounted for in the reordering of the data matrix $\mathbf{X}$. The complete vector $\mathbf{g}^i$ is now succinctly expressed as

$$\begin{bmatrix} \mathbf{g}_1^i \\ \vdots \\ \mathbf{g}_N^i \end{bmatrix} = \begin{bmatrix} \mathbf{X}_1\overline{\mathbf{w}}_1^i \\ \vdots \\ \mathbf{X}_N\overline{\mathbf{w}}_N^i \end{bmatrix} \qquad (2.23)$$

where the structure of the matrices $\mathbf{X}_j$ accounting for the jth data cube slice is given by (2.22), and $\overline{\mathbf{w}}_q^i$ is the designable component of the qth row of the coded aperture. In matrix notation (2.23) can be expressed as

$$\mathbf{g}^i = \boldsymbol{\mathcal{X}}\overline{\mathbf{W}}^i \qquad (2.24)$$

where $\overline{\mathbf{W}}^i = \{\overline{\mathbf{w}}_1^{i\,T}, \overline{\mathbf{w}}_2^{i\,T} \ldots \overline{\mathbf{w}}_N^{i\,T}\}^T$, and $\boldsymbol{\mathcal{X}} = \mathrm{diag}\{\mathbf{X}_1, \mathbf{X}_2, \ldots, \mathbf{X}_N\}$ is a block diagonal matrix. Equations (2.21) and (2.24) provide a new representation for the measurements of CAASI when multiple shots are admitted. The new formulation is illustrated in Fig. 2.5. In the traditional model (Fig. 2.5(a)), the input is the data cube $\mathbf{f}$ and the output $\mathbf{g}^i$ is characterized by the matrix $\mathbf{H}^i$. In the new representation (Fig. 2.5(b)), the input is the matrix $\boldsymbol{\mathcal{X}}$ and the output is obtained by varying the matrix $\overline{\mathbf{W}}^i$. The matrix $\boldsymbol{\mathcal{X}}$ represents a reordered version of the vector $\mathbf{f}$ so as to account for the spectral sheering and $\mathbf{R}$, the random term of the coded aperture. Note that the elements of $\overline{\mathbf{W}}^i$ in the new representation in (2.24) explicitly contains the components of the coded apertures that must be optimized. Observe that the matrices $\mathbf{H}^i$ in (2.12) have a total of $(N)(M+L-1) \times (N \cdot M \cdot L)$ elements each, compared to the $N(M+L-1) \times L$ elements of the matrix $\boldsymbol{\mathcal{X}}$ in (2.23). The new model is thus significantly more compact than that of (2.12) and consequently it is better suited for iterative optimization algorithms.
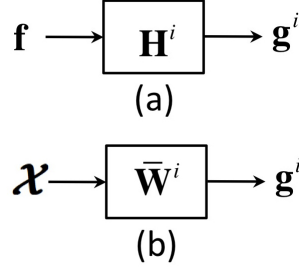
Figure 2.5: (a) The traditional model where the data cube $\mathbf{f}$ is processed with the highly sparse matrix $\mathbf{H}^i$. The coded aperture pattern is hidden in $\mathbf{H}^i$; (b) new model of CAASI: $\mathbf{f}$ is first re-ordered and expanded into the matrix $\boldsymbol{\mathcal{X}}$ which is then processed by the weight matrix $\mathbf{W}^i$ whose elements are the coded aperture patterns.

2.4   Aperture Code Optimization in Multishot CAASI

Each measurement in CAASI uses an optimized $\mathbf{W}^i$ coded aperture component. Since the spectral coding is mutually independent between the rows of the detector, it is sufficient to design one row of $\mathbf{W}^i$. The remaining rows are completed by shifted replicas of the first such that $\mathbf{W}^i = \mathbf{u}_N \otimes \mathbf{w}^i$. Furthermore, since $\mathbf{w}^i$ is a concatenation of several identical segments $\overline{\mathbf{w}}^i$, the optimization of the K $\mathbf{W}^i$ coded aperture matrices reduces to the optimization of K $\overline{\mathbf{w}}^i$ vectors.

Before the optimization problem is formulated, it is useful to first simplify the notation by deleting the subindex q in the above formulation, which indicates a particular slice of the CASSI system. It is also useful to note the similarities of the CAASI system to a multichannel filtering problem where the input signal is the data cube $\mathbf{f}$ and the filter coefficients are the elements of the coded aperture $\overline{\mathbf{w}}^i$. The filtering problem, in this case, aims at optimizing the coefficients (coded apertures) such that the linear combination of the outputs at each jth position at the detector is as close as possible to a desired response, one that only contains information of the specific bands of interest. The coded aperture design problem is thus analogous to finding the set of the optimal filter coefficients in filter design. More formally, given an input signal $\mathbf{f}^s$ and a desired output signal $\mathbf{d}$, then the objective is to find the K optimal filter weight vectors (aperture codes $\overline{\mathbf{w}}^1$, $\overline{\mathbf{w}}^2$,...,$\overline{\mathbf{w}}^K$) and a set of associated weights b_{ij} such that the error vector $\mathbf{e} = [e_1, e_2, \ldots, e_{M+L-1}]^T$ is minimized according to an error criterion. Figure 2.6 depicts the aperture code optimization problem as a filtering problem for the jth position on a detector row. To proceed with the filter design approach, a test image cube $\mathbf{f}^s$ is first created as follows. Define a sequence of distinct prime numbers $\{s_1, s_2, \ldots, s_L\}$ such that $s_l \neq s_j$ for all $l \neq j$. Choosing the set of primes properly, it is possible to guarantee that

$$\sum_{\substack{j=1 \\ j \neq l}}^{L} s_j z_j \neq s_l \tag{2.25}$$

for all l, where the coefficients z_j are binary, $z_j \in \{0, 1\}$. If a coefficient set $\{z_j\}_{j=1}^{L}$ is different from another $\{z'_j\}_{j=1}^{L}$ in at least one element, then from the properties of prime numbers it follows that $\sum_{j=1}^{L} z_j s_j \neq \sum_{j=1}^{L} z'_j s_j$. Given the set of prime numbers, the test data cube to be used in the filter design is then set to

$$(\mathbf{F}_k^s)_{nm} = s_k \quad \text{for all } m, n. \tag{2.26}$$

Hence $\mathbf{F}^s$, is a cube where each spectral slice takes on the constant value of s_k across all the spatial positions m and n. A slice of the data cube at $n = q$ in vector form is denoted by $\mathbf{f}^s$ across all m and k . Clearly $(\mathbf{F}_{k_1}^s)_{n,m} \neq (\mathbf{F}_{k_2}^s)_{n,m}$ if $k_1 \neq k_2$. The mapping operation converting $\mathbf{f}^s$ into $\mathbf{X}$ is shown in Fig. 2.6 as the re-indexing operation.
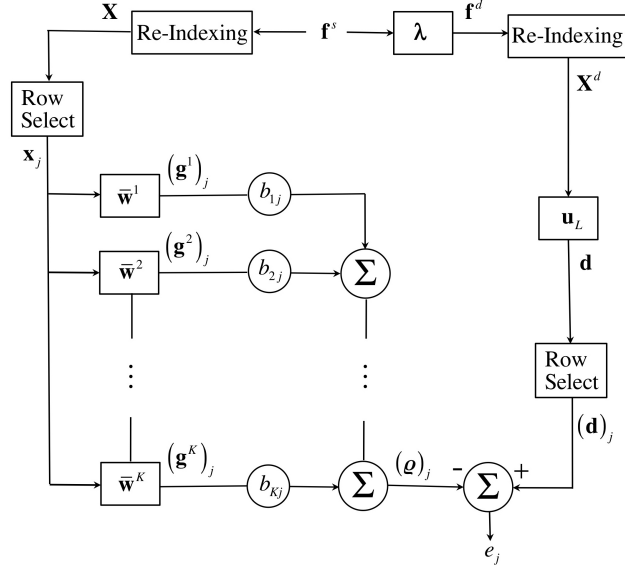
Figure 2.6: Code aperture optimization as a filter design problem. The input is a row of the data cube $\mathbf{f}^s$ and the desired signal is $\mathbf{f}^0$. The filter coefficients (aperture codes $\overline{\mathbf{w}}^1, \overline{\mathbf{w}}^2, \ldots, \overline{\mathbf{w}}^K$) and the coefficients b_{ij} are optimized by minimizing a cost function of the errors $e_1, e_2, \ldots, e_{M+L-1}$. The error at given j^{th} position at a row at the detector is the difference between the linear combination of the measurements $(\boldsymbol{\varrho})_j$ and $(\mathbf{d})_j$.

From (2.25) and the CAASI equation (2.21), given the detector measurements sequence at the detector, $\mathbf{g}^i$, it is possible to determine which spectral bands are present in the linear combination yielding $\mathbf{g}^i$. This is the case since $(\mathbf{F}_k^s)_{qm}$ and $\mathbf{X}$ are known. The desired signal $\mathbf{d}$, shown in Fig. 2.6, is created from $\mathbf{F}^d$ which contains only the desired bands and is given by

$$(\mathbf{F}_k^d)_{nm} = \begin{cases} (\mathbf{F}_k^s)_{nm} & \text{if } (\boldsymbol{\lambda})_k = 1 \\ 0 & \text{otherwise} \end{cases} \tag{2.27}$$

for all m, n and where the L-long binary vector $\boldsymbol{\lambda}$ indexes the subset of spectral channels of interest. In particular $(\boldsymbol{\lambda})_k$ is defined as

$$(\boldsymbol{\lambda})_k = \begin{cases} 1 & \text{if the } k^{th} \text{ spectral band is of interest} \\ 0 & \text{otherwise,} \end{cases} \tag{2.28}$$

for $k \in \{1, \ldots, L\}$. The qth slice of $\mathbf{F}^d$ is $\mathbf{f}^d$ which is thus forced to have only the spectral components of interest. The output at the detector, when the desired data cube $\mathbf{f}^d$ is sensed, is given by

$$\mathbf{d}^i = \mathbf{X}^d \tilde{\mathbf{w}}^i \tag{2.29}$$

where $\mathbf{X}^d$ is a matrix whose elements are obtained by the re-indexing of $\mathbf{f}^d$. Since $\mathbf{X}^d$ contains only information from the desired spectral bands, then the desired signal $\mathbf{d}^i$ can be calculated by a code $\tilde{\mathbf{w}}^i$ that simply adds the row elements of $\mathbf{X}^d$. This operation is analogous to using an "all pass" code $\tilde{\mathbf{w}}^i$ that permits to pass all the spectral information from $\mathbf{X}^d$. In this case, the all-pass code $\tilde{\mathbf{w}}^i = \mathbf{u}_L$, in effect, simply sums all elements of $\mathbf{X}^d$. The vector $\mathbf{d}^i$ in (2.29) does not depend of the coded aperture $\tilde{\mathbf{w}}^i$ and it is the desired output $\mathbf{d}$. Note that the desired signal $\mathbf{d}$ is unique in the sense that only the specific combination of spectral bands given by $\boldsymbol{\lambda}$ can generate the output of CAASI equal to $\mathbf{d}$. This is precisely the motivation of using the set of prime numbers in (2.25) as elements of the data cube $\mathbf{f}^s$. To further illustrate the underlying concepts, Fig. 2.7 shows a typical slice of the data cube $\mathbf{f}^s$ and the corresponding structure of the matrix $\mathbf{X}$. Observe that the elements of the output $\mathbf{g}^i$ are calculated by the Hadamard product of the coded aperture $\mathbf{w}^i$ and each row of $\mathbf{X}$. In Fig. 2.6 the operation of extracting $\mathbf{x}_j$ the jth
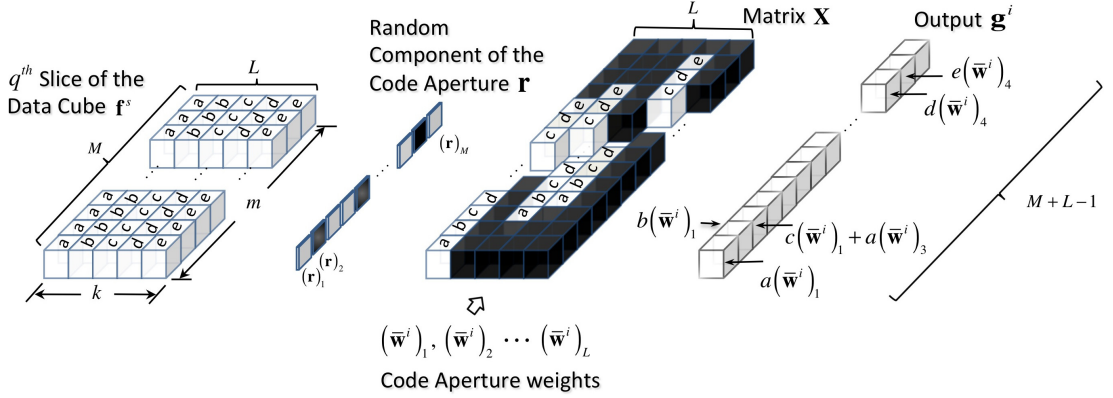
Figure 2.7: A slice of the data cube $\mathbf{f}^s$ is modulated by the vector $\mathbf{r}$ and then reorganized into the matrix $\mathbf{X}$. The output at the detector is calculated as $\mathbf{g}^i = \mathbf{X}\overline{\mathbf{w}}^i$.

row of $\mathbf{X}$ is indicated with the "Row-Select" operation. From Fig. 2.6, the error at j^{th} position in the detector is

$$e_j = (\mathbf{d})_j - (\boldsymbol{\varrho}^i)_j \qquad j = 1, \ldots, M + L - 1 \tag{2.30}$$

where $(\boldsymbol{\varrho})_j = \sum_{i=1}^{K} b_{ij}\mathbf{x}_j^T\overline{\mathbf{w}}^i$. Notice that $\mathbf{d}$ and $\mathbf{x}_j$ are known terms and $\overline{\mathbf{w}}^i$ represents the unknown aperture codes pattern to be designed. The coefficients b_{ij} permit to use all the information available from the K shots to minimize the jth component at a row at the detector. The coefficients b_{ij} are restricted to the three values $\{-1, 0, 1\}$ that the value -1 indicates the subtraction of a set of bands, 0 indicates the suppression of a set of bands, and 1 indicates the summation of a set of bands. The errors originated from the measurements in (2.30) are concatenated into the common array $\mathbf{e}' = [e_1, e_2, \ldots, e_{M+L-1}]$.

The component-wise squared error metric is first calculated such as $\mathbf{e} = \mathbf{e}' \circ \mathbf{e}'$. The jth element of $\mathbf{e}$ can be expressed as a function of the coded aperture as $(\mathbf{e})_j = \left((\mathbf{d})_j - \sum_{i=1}^{K} b_{ij}\mathbf{x}_j^T\overline{\mathbf{w}}^i\right)^2$. Note that $(\mathbf{e})_j = 0$ occurs only when the coded apertures are able to exactly extract the desired bands $\boldsymbol{\lambda}$ in the jth position in the detector. Note also that when $(\mathbf{e})_j > 0$ then there are additional spectral bands included, or not all desired bands are present in the jth entry of the $\boldsymbol{\varrho}$ vector. Given that the spectral selectivity consists on obtaining at each position in the detector exclusively the desired spectral components, it is equivalent to maximizing the number of elements $(\mathbf{e})_j$ equal to zero. In other words, it is equivalent to minimizing the L_0 norm of the vector $\mathbf{e}$. Hence, one seeks to obtain the vectors $\mathbf{W} = \left[\overline{\mathbf{w}}^1, \ldots, \overline{\mathbf{w}}^K\right]$ and the coefficients $\mathbf{B} = \left[\{b_{11}, \ldots, b_{K1}\}^T, \ldots, \{b_{1(M+L-1)}, \ldots, b_{K(M+L-1)}\}^T\right]$ such that

$$\arg\min_{\mathbf{W}, \mathbf{B}} \qquad \|\mathbf{e}\|_0 \tag{2.31}$$

$$\text{subject to} \quad (\mathbf{W})_{ki} \in \{0, 1\} \qquad k = 1, \ldots, L, \quad i = 1, \ldots, K$$
$$(\mathbf{B})_{ij} \in \{-1, 0, 1\} \qquad j = 1, \ldots, M + L - 1.$$

Since the measurements $\mathbf{g}^i$ contain complementary information between them, the functionality of the coefficients b_{ij} is to increase the number of solutions in (2.31) such that an iterative algorithm can converge more easily. Since the elements of $\overline{\mathbf{w}}^i$ and b_{ij} are binary and ternary, respectively, solving (2.31) is an NP hard problem. An approximate solution, however, can be sought using a heuristic approximation such as a genetic algorithm (GA) [?]. GAs are specially well suited to solve optimization problems that involves binary variables. This optimization technique has already been used in several optics optimization problems [?, ?]. The genetic algorithm (GA) approach to solve (2.31) is shown in Table 2.1. The stopping criterion to solve (2.31) is that $\|\mathbf{e}\|_0 = 0$. Notice that this stopping criterion conduces to a solution where the optimal codes lead to measurements containing exclusively the desired bands. A measurement containing the desired components can be constructed from the results of the

optimization as

$$\boldsymbol{\varrho}^* = \left[\sum_{i=1}^{K} (\mathbf{B}^*)_{i1} \mathbf{x}_1^T \overline{\mathbf{w}}^{*i}, \quad \sum_{i=1}^{K} (\mathbf{B}^*)_{i2} \mathbf{x}_2^T \overline{\mathbf{w}}^{*i}, \dots, \sum_{i=1}^{K} (\mathbf{B}^*)_{i(M+L-1)} \mathbf{x}_{M+L-1}^T \overline{\mathbf{w}}^{*i} \right] \qquad (2.32)$$

where $\mathbf{B}^*$ contains the optimal linear coefficients and $\overline{\mathbf{w}}^{*i}$ are the optimal coded apertures attained in (2.31).

Table 2.1: Iterative Optimization of coded apertures $\{\overline{\mathbf{w}}^{*1}, \dots, \overline{\mathbf{w}}^{*K}\}$ and the optimal matrix $\mathbf{B}^*$.

Inputs	Desired spectral bands $\boldsymbol{\lambda}$, Number of shots K, Prime numbers s_k, Population size $\mathcal{S}$, Number of iterations $\mathcal{N}$, Mutation percentage p_m.
Initialize	Data Cube $s_k \to \mathbf{f}^s \to \mathbf{X}^s$. Desired Signal $(s_k, \boldsymbol{\lambda}) \to \mathbf{f}^d \to \mathbf{X}^d \to \; \to \mathbf{d} \to \boldsymbol{\mathcal{D}} = \mathbf{d} \otimes \mathbf{u}_{\mathcal{K}}^T$. $\boldsymbol{\mathcal{B}} = \{\mathbf{b}^1, \dots, \mathbf{b}^{\mathcal{K}}\}$, where $\mathcal{K} = 3^K$, and $\mathbf{b}^{m_1} \neq \mathbf{b}^{m_2}$ for each $m_1 \neq m_2$, $m_1 = 1, \dots, \mathcal{K}$, and $m_2 = 1, \dots, \mathcal{K}$. Global minimum $\xi^* = M + L - 1$. Population: For $\ell = 1, \dots, \mathcal{S}$ compute: $\mathbf{P}_\ell^{(0)} = \{\overline{\mathbf{w}}_\ell^1, \dots, \overline{\mathbf{w}}_\ell^K\}$, $\qquad$ where $(\overline{\mathbf{w}}_\ell^i)_k$=Bernoulli(0.5).
Iteration	While, $n < \mathcal{N}$ and $\xi^* > 0$ $\quad$ For $\ell = 1, \dots, \mathcal{S}$ compute $\qquad \mathbf{G}_\ell^{(n)} = \mathbf{X} \mathbf{P}_\ell^{(n)}, \quad \boldsymbol{\mathcal{G}}_\ell^{(n)} = \mathbf{G}_\ell^{(n)} \boldsymbol{\mathcal{B}}, \; \mathbf{E}_\ell^{(n)} = \left(\boldsymbol{\mathcal{D}} - \boldsymbol{\mathcal{G}}_\ell^{(n)} \right) \circ \left(\boldsymbol{\mathcal{D}} - \boldsymbol{\mathcal{G}}_\ell^{(n)} \right)$ $\qquad (\hat{\mathbf{e}}_\ell^{(n)})_j = \min_m \left(\mathbf{E}_\ell^{(n)} \right)_{jm}, (\boldsymbol{\xi}^{(n)})_\ell = \|\hat{\mathbf{e}}_\ell^{(n)}\|_0, (\boldsymbol{\mathcal{L}}^{(n)})_{\ell j} = \arg\min_m \left(\mathbf{E}_\ell^{(n)} \right)_{jm}$. $\quad$ End For $\quad \ell* = \arg\min_\ell (\boldsymbol{\xi}^{(n)})_\ell$. $\quad$ If $(\boldsymbol{\xi}^{(n)})_{\ell*} < \xi^*$, then : $\qquad \xi^* = (\boldsymbol{\xi}^{(n)})_{\ell*}, \{\overline{\mathbf{w}}^{*1}, \dots, \overline{\mathbf{w}}^{*K}\}^T = \mathbf{P}_{\ell*}^{(n)}, (\mathbf{B}^*)_{kj} = (\boldsymbol{\mathcal{B}})_{k(\boldsymbol{\mathcal{L}}^{(n)})_{\ell*j}}$. $\quad$ End If $\quad \{\mathbf{P}_1^{(n+1)}, \dots, \mathbf{P}_{\mathcal{S}}^{(n+1)}\} = \text{Mu} \left(\text{Cr} \left(\text{Sl} \left(\{\mathbf{P}_1^{(n)}, \dots, \mathbf{P}_{\mathcal{S}}^{(n)}\}, \boldsymbol{\xi}^{(n)} \right) \right) \right)$. End While
Output	Optimal aperture codes $\overline{\mathbf{w}}^{*1}, \dots, \overline{\mathbf{w}}^{*K}$. Optimal linear coefficient $\mathbf{B}^*$.
Note	$j = 1, \dots, M + L - 1$ and $k = 1, \dots, L$.

A property of the optimized aperture codes is that if the codes $\overline{\mathbf{w}}^{*1}, \dots, \overline{\mathbf{w}}^{*K}$ and their respective optimal coefficient matrix $\mathbf{B}^*$ can extract the spectral bands given by $\boldsymbol{\lambda}$, then the same codes with a different coefficient matrix $\mathbf{B}^{n*}$ can extract the spectral bands given by $\boldsymbol{\lambda}_n$ with

$$(\boldsymbol{\lambda}_n)_k = (\boldsymbol{\lambda})_{(\langle k-n \rangle_L)}, \qquad k = 1, \dots L \qquad (2.33)$$

where $\langle k - n \rangle_L$ indicates the $k - n$ modulo L operation or equivalently a n circular shift of period L. This property requires that $\boldsymbol{\lambda}$ has some circular period $\mathcal{N}$ and that the ratio $\frac{L}{\mathcal{N}}$ is an integer. Finding the new matrix $\mathbf{B}^{n*}$ involves simple algebraic operations. The optimized aperture codes are thus circular shift invariant to the vector $\boldsymbol{\lambda}$.

2.5 Simulations and Results

2.5.1 Coded Aperture Optimization

To test the methodology developed in Section 2.4, the algorithm in Table 2.1 is used to find the optimal aperture codes for several desired spectral band sets $\boldsymbol{\lambda}$, for increasing number of measurement shots. The experiments use a test data cube F^s with $L = 24$ spectral bands in 504nm-757nm and 256×256 spatial dimensions. A set of 24 prime numbers s_k is generated such that (2.25) is satisfied. The other parameters of the algorithm in Table 1 are: population size $\mathcal{S} = 100$, mutation percentage $p_m = 0.01$, and maximum number of iterations $\mathcal{N} = 5000$. In the experiment, the following desired spectral bands $\boldsymbol{\lambda}$ are used in

the optimization

$$\boldsymbol{\lambda}^1 = [100010100000000000110000] \qquad \boldsymbol{\lambda}^2 = [100010001000100010001000]$$
$$\boldsymbol{\lambda}^3 = [101000101000101000101000] \qquad \boldsymbol{\lambda}^4 = [110000001100000011000000] . \qquad (2.34)$$

From numerous simulations, it can be observed that the algorithm converges for $K < L$ when the vector
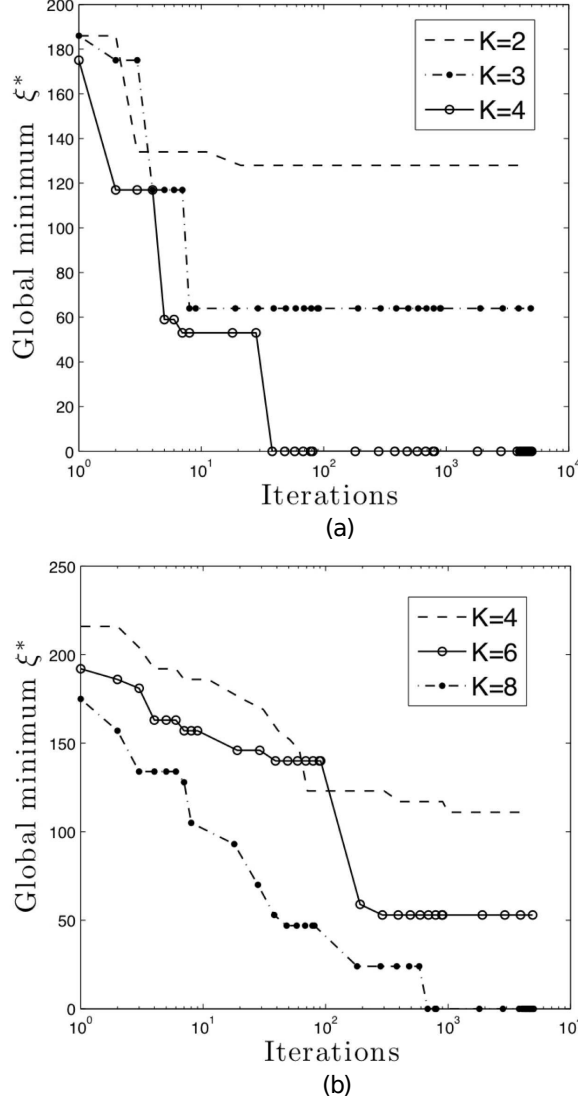
Figure 2.8: Performance evolution ξ^* as a function of the iterations when the vectors (a) $\boldsymbol{\lambda}^2$ and (b) $\boldsymbol{\lambda}^4$ in (2.34) are used as input of the GA.

$\boldsymbol{\lambda}$ is circularly periodic. When $\boldsymbol{\lambda}$ is aperiodic, the algorithm converges for $K = L$. Figure 2.8 shows the performance evolution ξ^* as a function of the iterations when the vectors $\boldsymbol{\lambda}^2$ and $\boldsymbol{\lambda}^4$ are used as input of the AG. Figure 2.9 illustrates the optimal aperture codes $\overline{\mathbf{w}}^{*i}$ when the vectors $\boldsymbol{\lambda}^1$, $\boldsymbol{\lambda}^2$, λ^3, and $\boldsymbol{\lambda}^4$ are used as input to the optimization algorithm. Additionally, Fig. 2.10 shows an 128×128 matrix whose elements are constructed by replicates of the optimal coded apertures and coded by a random component. Each row of these matrices is constructed by selecting randomly an optical code $\overline{\mathbf{w}}^i$, such that the entire matrix contains information of the all optimal codes. In addition to the optimal codes, the optimization provides the optimal coefficient matrix $\mathbf{B}^*$ used to construct the elements of the optimal virtual measurement $\boldsymbol{\varrho}^*$. Figure 2.11 illustrates the optimal matrix $\mathbf{B}^*$ when $\boldsymbol{\lambda}^4$ is used; due to space limitations only a portion of this matrix is shown. Note that the patterns in Fig. 2.11 exhibit periodicity,

except in the beginning and end which exhibit edge structures that are different from that of the main region.
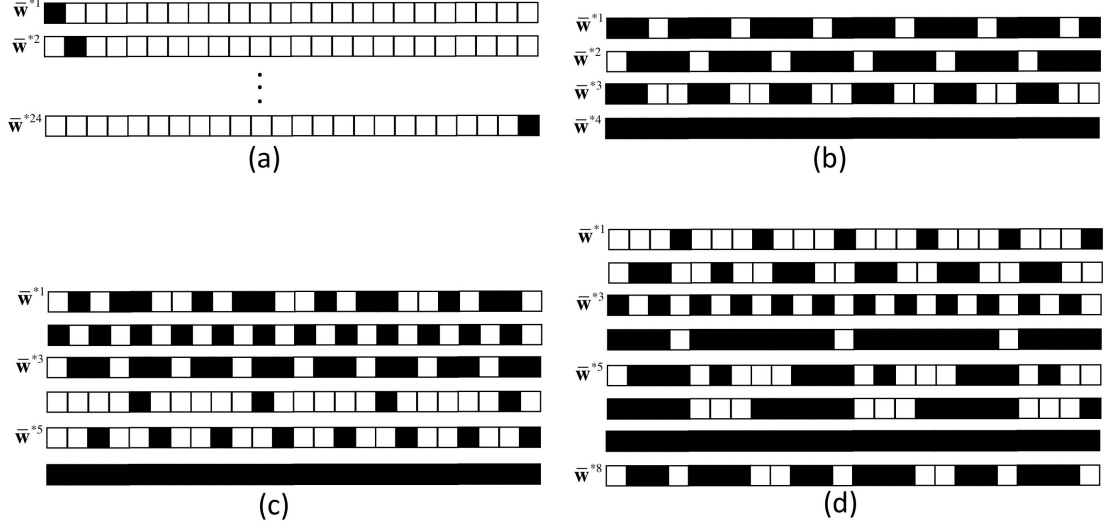
Figure 2.9: Optimal coded apertures $\overline{\mathbf{w}}^{*i}$ for the vectors (a) $\boldsymbol{\lambda}^1$, (b) $\boldsymbol{\lambda}^2$, (c) $\boldsymbol{\lambda}^3$, and (d) $\boldsymbol{\lambda}^4$ indicated in (2.34).
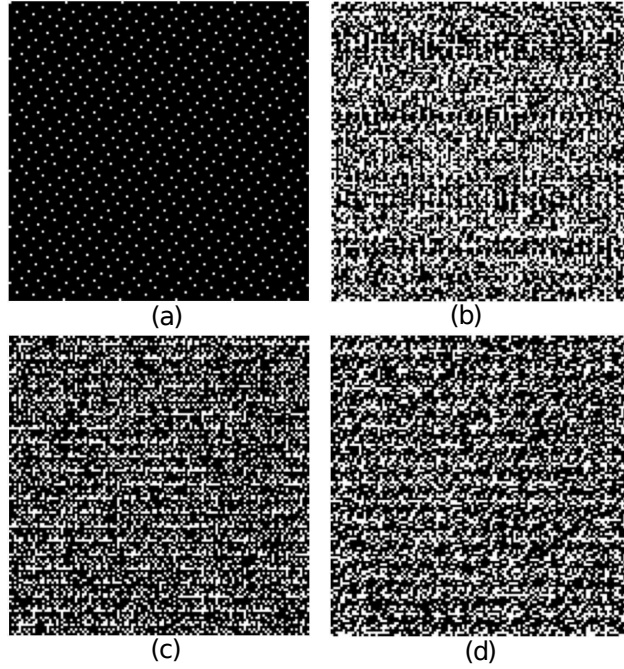
Figure 2.10: An 128×128 realization of the optimal coded apertures for the vectors (a) $\boldsymbol{\lambda}^1$, (b) $\boldsymbol{\lambda}^2$, (c) $\boldsymbol{\lambda}^3$, (d) $\boldsymbol{\lambda}^4$ given in (2.34).

2.5.2   Filter Bank Representation

The filter bank spectral model aims at reconstructing the entire data cube from the $\mathcal{V}$ compressive measurements where each measurement has information only from one of $\mathcal{V}$ disjoint spectral subsets with the constraint of using only $K \leq L$ shots. Each subset can be reconstructed separately and the results can
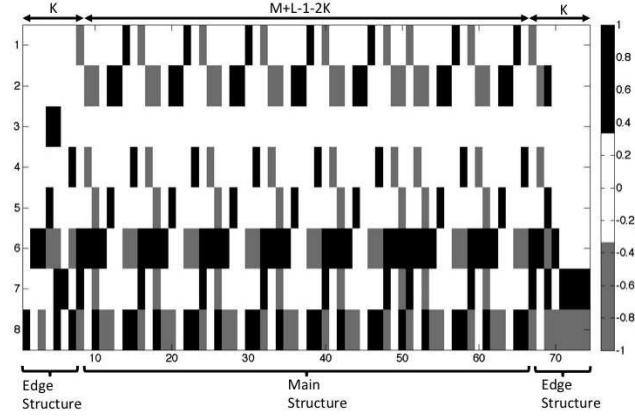
Figure 2.11: A part of the matrix $\mathbf{B}^*$ is shown. The lth column of $\mathbf{B}^*$ represents the optimal coefficient to construct the measurement element $(\boldsymbol{\varrho}^*)_l$. The vector $\boldsymbol{\lambda}^4$ is used as input of the optimization algorithm.

be merged. The disjoint spectral subsets are specifically designed such that the shift invariance property of the coded apertures developed in previous sections is used. More specifically, suppose that the L long vector $\boldsymbol{\lambda}$ has circular period $\mathcal{N}$, define $\mathcal{U}$ as the maximum number of consecutive one elements in a period of $\boldsymbol{\lambda}$, and define $\mathcal{V}$ as $\mathcal{V} = \lceil \frac{\mathcal{N}}{\mathcal{U}} \rceil$. Then the complete data cube can be reorganized in $\mathcal{V}$ compressive measurements with information only from the bands given by $\{\boldsymbol{\lambda}_0, \boldsymbol{\lambda}_1, \ldots, \boldsymbol{\lambda}_{\mathcal{V}-1}\}$ where the elements of each subset $\boldsymbol{\lambda}_n$ is given by

$$(\boldsymbol{\lambda}_n)_k = (\boldsymbol{\lambda})_{(\langle k-n\mathcal{U}\rangle)_L} \quad k = 1, \ldots, L. \tag{2.35}$$

The filter bank representation is attained as follows: (a) generate a set of vectors $\{\boldsymbol{\lambda}_0, \ldots, \boldsymbol{\lambda}_{\mathcal{V}-1}\}$ where each vector $\boldsymbol{\lambda}_i$ is a shifted version of $\boldsymbol{\lambda}_0 = \boldsymbol{\lambda}$; (b) verify that $\boldsymbol{\lambda}_0 \vee \boldsymbol{\lambda}_1 \vee \ldots \vee \boldsymbol{\lambda}_{\mathcal{V}-1} = \mathbf{u}_L$ where $\vee$ is the boolean sum; (c) The spectral components given by the different $\boldsymbol{\lambda}_i$ can be reconstructed separately and the results can be merged with the other reconstructions. Since $[\overline{\mathbf{w}}^{*1}, \ldots, \overline{\mathbf{w}}^{*K}]$ are the optimal codes and $\mathbf{B}^*$ is the optimal coefficient matrix to recover $\boldsymbol{\lambda}$, then each combination $\{[\overline{\mathbf{w}}^{*1}, \ldots, \overline{\mathbf{w}}^{*K}]^T, \mathbf{B}^{i*}\}$ can be seen as a compressive filter bank to recover $\boldsymbol{\lambda}_i$, where $\mathbf{B}^{i*}$ is a reordered version of the matrix $\mathbf{B}^*$. A representation of this technique was illustrated in Fig. 2.2. Define the "mod_p" $\boldsymbol{\lambda}$ pattern which elements are given by

$$(\boldsymbol{\lambda})_k = \text{mod}(k, p) \quad k = 1, \ldots, L \tag{2.36}$$

where mod is the modulo operation, p is the circular period of $\boldsymbol{\lambda}$, and L is the total number of bands. Here, it is assumed that the ratio $\frac{L}{p}$ is an integer. These "mod_p" patterns can be used to decompose the data cube in the subsets $\{\boldsymbol{\lambda}_0, \boldsymbol{\lambda}_1, \ldots, \boldsymbol{\lambda}_{p-1}\}$ where $\boldsymbol{\lambda}_0$ is equal to $\boldsymbol{\lambda}$ in (2.36) and the others $\boldsymbol{\lambda}_i$ are given by (2.35) with $\mathcal{U} = 1$. Notice that the $\boldsymbol{\lambda}_i$ subsets satisfy the above (b) condition necessary to apply the filter bank decomposition. Decompose the data cube in the "mod_p" subsets requires p shots. The respective optimal coded apertures to select the mod_p patterns is referred to as "mod_p filter bank coded apertures". For example, referring to Eq. (2.34), $\boldsymbol{\lambda}^2$ is a mod_4 pattern and the codes of Fig. 2.9(b) are a mod_4 filter bank coded apertures.

2.5.3 Reconstruction Algorithm

A number of CS reconstruction algorithm are available in the literature [?, ?, ?, ?]. The Gradient Projection for Sparse Reconstruction algorithm (GPSR) [?] was used to reconstruct the spectral data cubes in our simulations as it exhibits faster computational speed. This algorithm reconstructs of the data cube $\mathbf{f}$ by solving the minimization $\hat{\mathbf{f}} = \Psi\{\arg\min_{\theta'} \|\boldsymbol{\varrho}^* - \mathbf{H}\Psi\theta'\|_2^2 + \tau\|\theta'\|_1\}$, where $\boldsymbol{\varrho}^*$ are the optimized measurements. The operation that involves the sparse matrix $\mathbf{H}$ are implemented through the indexes of non-zero elements of the matrix $\mathbf{H}$ instead of using it directly. The base representation Ψ is the Kronecker product of three basis $\Psi = \Psi_1 \otimes \Psi_2 \otimes \Psi_3$, where the combination $\Psi_1 \otimes \Psi_2$ is the 2D-Wavelet Symmlet 8 basis and Ψ_3 is the Cosine basis [?]. A data cube of satellite images is used, it has 24 spectral

channels and 256×256 pixels of spatial resolution. Reconstruction was realized using a desktop with 3.06 GHz Intel Core 2 Duo processor, and 4GByte 1067 MHz DDR3 RAM. The simulation tool was Matlab 2007a version 7.4.0 for MacOS version 10.6.4. The simulations were realized using double numerical precision. The maximum number of iterations in the GPSR algorithm is 700 and the stopping criterion as recommend in [?] is the objective function. Figure 2.12(b), Fig. 2.12(c), and Fig. 2.12(d) depict the reconstruction results for the first spectral band of the data cube applying the technique of compressive filter bank. The mod_2, mod_{12}, and mod_{24} filter bank coded apertures are used in the decomposition. Clearly the SNR increases with the number of shots used.
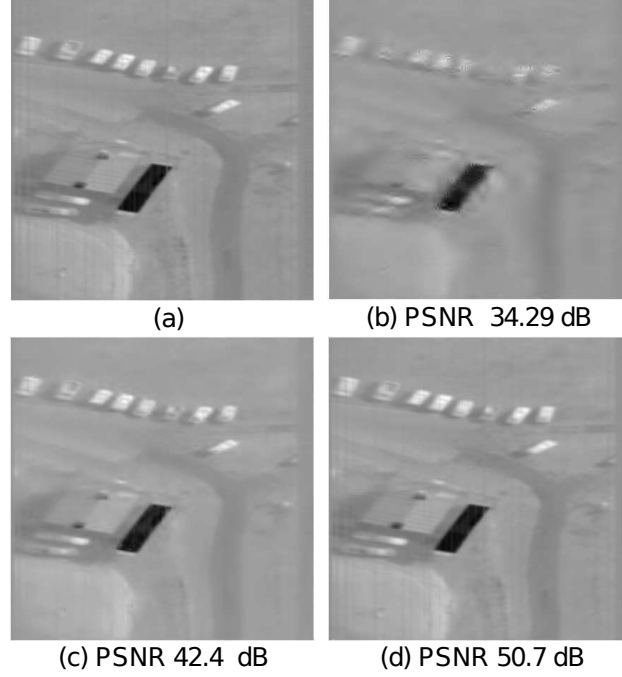
Figure 2.12: Reconstruction of the first spectral band of the 24 spectral band data cube. (a) Original; reconstruction using (b) mod_4 filter bank coded apertures, 4 shots; (c) mod_{12} filter bank coded apertures, 12 shots; (d) mod_{24} filter bank coded apertures, 24 shots.

A comparison between the compressive filter bank technique and a random multishot approach was realized. The random multishot technique consists on using random coded aperture patterns to realize the compressive measurements [?, ?]. In that technique, no optimization of the coded apertures was carried out. Figures 2.13(b), 2.13(c), and 2.13(d) show the reconstruction of the same first band of the data cube using the random codes for K equal to 2, 12 and 24 shots. Figure 2.14 illustrates the general results in terms of SNR for the multishot and filter bank approaches as a function of the number of shots K. Notice that in the multishot case, the complete spectral data cube is reconstructed at once. In the filter bank approach, on the other hand, the complete data cube is divided in K disjoints subsets where the nth subset $\boldsymbol{\lambda}_n$ is given by

$$(\boldsymbol{\lambda}_n)_j = \begin{cases} 1 & \text{for } j = n, K+n, 2K+n, \ldots, (\frac{L}{K}-1)K+n \\ 0 & \text{otherwise.} \end{cases} \tag{2.37}$$

where $n = 0, \ldots, K-1$. Each desired subset is reconstructed independently from others. The reconstructed subset bands are then merged and the total SNR is calculated. The results show that when the number of shots increases, the filter bank approach is superior in quality of reconstruction. Figure 2.15 shows the respective reconstruction time for the same coded apertures used in Fig. 2.14. For the reconstruction technique Random Multishot, the reconstruction time decreases with increasing number of shots because when more shots are used the system of equations are less undetermined and the objective function decreases more quickly through the iterations. In the filter bank case the reconstruction times

(a)

(b) PSNR 33.08 dB

(c) PSNR 34.68 dB

(d) PSNR 34.74 dB
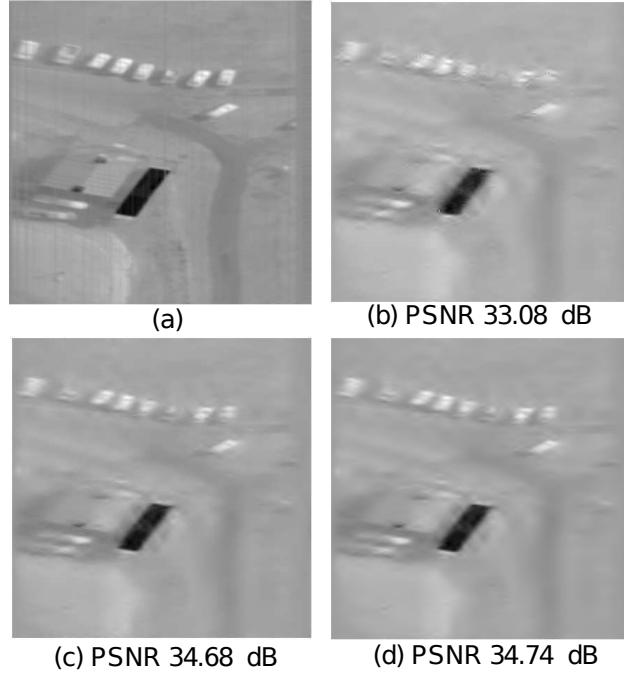
Figure 2.13: Reconstruction of the first spectral band of the 24 spectral band data cube. (a) Original; (b) random coded aperture, 4 shots; (c) random coded aperture, 12 shots; and (d) random coded aperture, 24 shots.
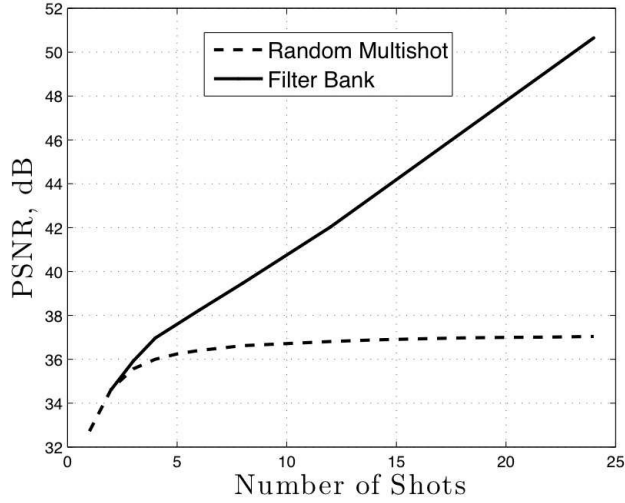
Figure 2.14: Mean PSNR for the reconstructed data cube as a function of the number of shots. The techniques of random multishot and compressive mod_p filter bank are shown.

are shown using both a single processor and a processor for the reconstruction of each subset of bands. The approach using several processors is coined "parallel filter bank". The parallel filter bank approach provides up to two orders of magnitude faster reconstruction than the random multishot approach. In the second experiment, we observe the spectral selectivity of the optimized coded apertures. In this case the reconstruction of the 1st and 18st bands are of interest. The vector $\boldsymbol{\lambda}_4$ in (2.34) is used as input of the optimization algorithm. In this experiment, the results for K equal to 4, 8, 12, and 16 shots are shown in Figs. 2.16(c)-2.16(d), 2.16(e)-2.16(f), 2.17(a)-2.17(b), and 2.17(c)-2.17(d) respectively. Note that in Fig. 2.8(b) shows a minimum number of $K = 8$ shots for convergence of the optimization algorithm. However, Figs 2.16(c)-2.16(d) show that it is possible to reconstruct the desired spectral bands with fewer number
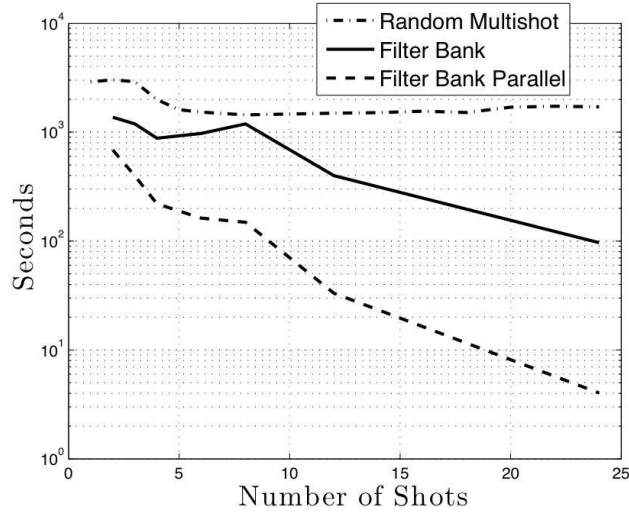
Figure 2.15: Reconstruction times for the full data cube as a function of the number of shots when is used (a) pure random coded apertures (Random Multishot); (b) $\mod_p$ filter bank optimized coded apertures (Filter Bank); and (c) $\mod_p$ filter bank coded apertures using a processor for each subset of bands (Filter Bank Parallel).

of shots.

2.6 Conclusions

We have developed the underlying theory and optimization framework for a new Coded Aperture Agile Spectral Imaging System (CAASI) which adds the spectral selectivity property to CASSI. The mathematical model of CAASI expresses the output signal as the product of a reordered version of the source input and the coded aperture. Using the new CAASI representation, an optimization algorithm is developed which finds the optimal coded apertures to be used in a multishot system such that spectrally selective compressive measurements are attained. The optimization aims at minimizing the L_0 norm between a data cube and a desired cube containing only the spectral bands of interest. A Genetic Algorithm solves the L_0 optimization problem and finds the minimum number of shots for convergence. The optimization algorithm converges to $K < L$ shots when the subset of desired bands exhibits some circular periodicity which is originated because any assumption is made over the random component of the coded aperture. The designed coded apertures exhibits a circular shift invariance property that permits to divide the reconstruction of the complete data cube in $\mathcal{V} \leq K$ less complex reconstructions problems. This property of the optimal codes can be seen as a compressive filter bank decomposition. The filter bank approach reconstructs either the complete data cube, or a selective subset of bands, with higher PSNR and takes up to two orders of magnitude less processing time than the traditional multishot approach with random coded apertures.
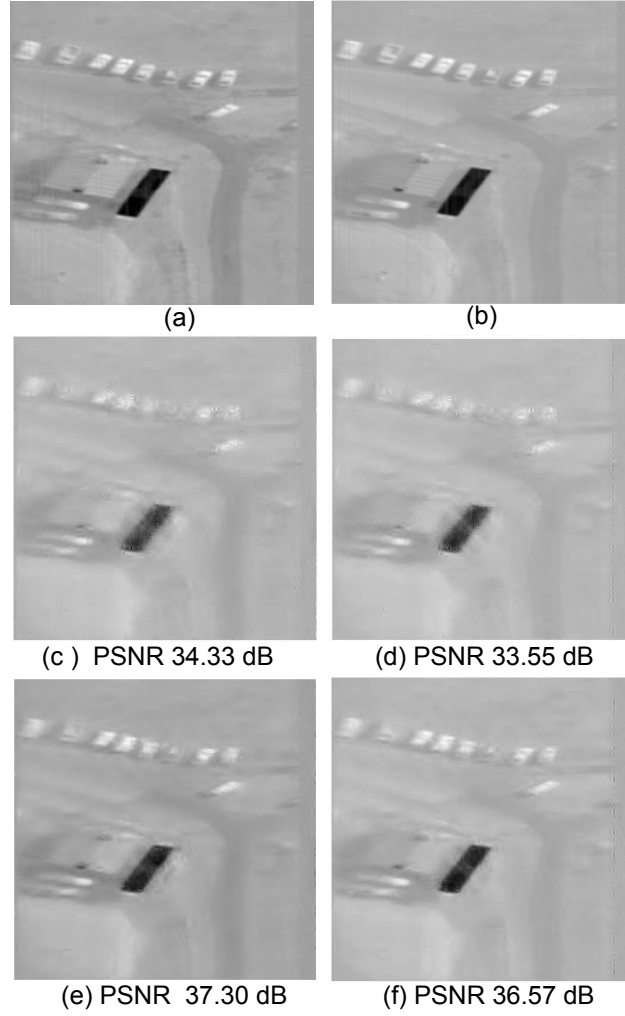
Figure 2.16: Reconstruction of the 1st and 18th spectral band of the 24 band data cube. (a) Original 1st band (b) original 18th band; reconstruction of the respective band using the vector $\boldsymbol{\lambda}_4$ in (2.34). (c), (d) 4 shots ; (e), (f) 8 shots.

(a) PSNR 39.00 dB   (b) PSNR 38.91 dB

(c) PSNR 39.59 dB   (d) PSNR 39.63 dB
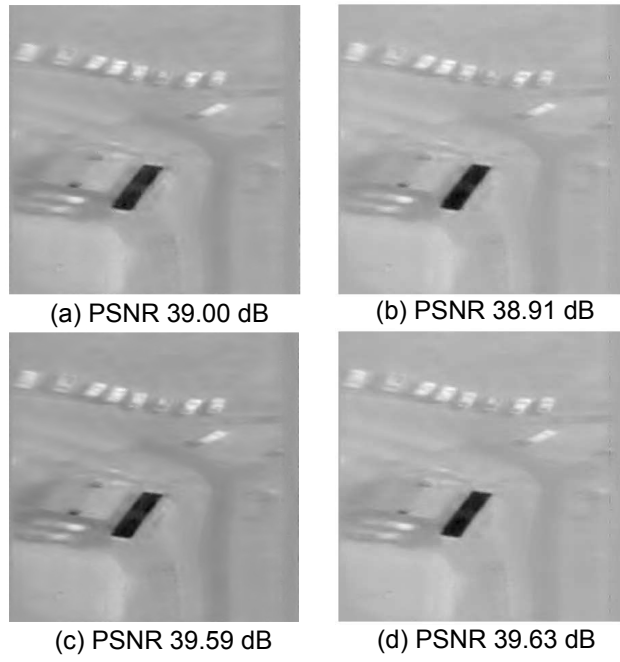
Figure 2.17: Reconstruction of the 1st and 18th spectral bands indicated in Fig. 2.16(a) and 2.16(b). Reconstruction of the respective band using the vector $\boldsymbol{\lambda}_4$ in (2.34) for (c), (d) 12 shots; (e), (f) 16 shots.

Chapter 3

Rank Minimization Coded Aperture Design for Spectrally Selective Compressive Imaging

3.1 Introduction

Consider again the Code Aperture Snapshot Spectral Imaging (CASSI) system that allows capturing spectral imaging information of a 3D cube with just a single 2D measurement of the coded and spectrally dispersed source field [?]. More formally, suppose a hyperspectral signal $\mathcal{F} \in \mathbb{R}^{N \times M \times L}$, or its vector representation $\boldsymbol{f} \in \mathbb{R}^{N \cdot M \cdot L}$, is S sparse on some basis $\boldsymbol{\Psi}_{3D}$, such that $\boldsymbol{f} = \boldsymbol{\Psi}_{3D}\boldsymbol{\rho}$ can be approximated by a linear combination of S vectors from $\boldsymbol{\Psi}_{3D}$ with $S \ll (N \cdot M \cdot L)$. Here, $N \times M$ represents the spatial dimensions and L is the spectral depth of the image cube. Compressive sensing shows that $\boldsymbol{f}$ can be recovered from m random projections with high probability when $m \gtrsim S \log(N \cdot M \cdot L) \ll (N \cdot M \cdot L)$. The CASSI projections are given by $\mathbf{y}_t = \mathbf{H}\boldsymbol{\rho}$, where $\mathbf{H} = \boldsymbol{\Phi}\boldsymbol{\Psi}_{3D}$ is an $N(M + L - 1) \times (N \cdot M \cdot L)$ matrix and $\boldsymbol{\Phi}$ is a random measurement matrix determined by the coded apertures and the dispersive element used in CASSI.

Recently, the CASSI spectral imaging architecture has been extended to admit multiple measurement shots [?, ?, ?]. The multiple measurements are attained as separate FPA measurements, each with a distinct coded aperture that remains fixed during the integration time of the detector. There are several advantages to multiple shots. First, the number of compressive measurements in CASSI may not meet the minimum needed for adequate reconstruction. CS dictates that the number of measurements must be in excess of $S \log(N \cdot M \cdot L)$. Failure to collect a sufficient number of measurements leads to inadequate signal reconstruction. With each FPA shot, CASSI collects $N(M + L - 1)$ additional measurements. For spectrally rich scenes or very detailed spatial scenes, a single shot CASSI measurement may not provide a sufficient number of compressive measurements. Increasing the number of measurement shots will multiply the number of measurements, thus rapidly overcoming such limitations.

A second advantage to multiple shots is that spectral selectivity can be attained by coded aperture design. Notably, the coded aperture patterns can be designed so as to maximize the information content on a pre-specified subset of spectral bands of particular interest in the CASSI compressive measurements. Spectral selectivity is of interest in many applications, including wide-area airborne surveillance, remote sensing, and tissue spectroscopy in medicine. The optimal spectral bands in airborne surveillance, for instance, depend on atmospheric conditions, time of day, the targets of interest, and the background against which the targets are viewed [?]. In these applications, the spectral signatures of interest live in a spectral band subspace. Efforts placed on acquiring the entire spectral image cube, to then throw away a large portion of this data is wasteful in many regards.

Chapter 2 provided the first approach for spectral selectivity in multi-shot CASSI; however, the selec-

tive spectral profiles were limited to periodic patterns and the minimum number of shots was restricted to the periodicity of the spectral pattern. In most practical applications, however, the spectral profiles of interest are not periodic and the number of shots is restricted by the application. The main contribution of this Chapter is the development of a more general and more effective mathematical framework for multi-shot CASSI and the corresponding algorithms for coded aperture optimization that allow the reconstruction of arbitrary subset of bands, periodic or aperiodic, whilst minimizing the required number of shots.

The CASSI model is first developed for a slice at the detector. It is then used to build a generalized 2D CASSI model. The output at a slice in the detector is expressed as the product of a matrix accounting for the dispersed spatio-spectral source density and a vector accounting for the coded aperture. The coded aperture for the ith measurement, denoted as $\mathbf{t}^i$, is seen as two separate coded apertures applied in tandem which simplifies their optimization. The first coded aperture $\mathbf{w}^i$ is a structured code optimized to attain the spectral band selectivity. The second coded aperture $\mathbf{r}^i$ is a pseudorandom binary code necessary to attain randomized measurements in CASSI. The coded aperture used in each measurement is obtained by the Hadamard product $\mathbf{t}^i = \mathbf{w}^i \circ \mathbf{r}^i$. The coded aperture optimization is divided in two parts. First the tunable components $\mathbf{w}^i$ are optimized to achieve spectrally selective measurements. The required number of shots K is dictated by the rank of a matrix containing the $\mathbf{w}^i$ codes. Second, the pseudorandom components of the coded apertures $\mathbf{r}^i$ are optimized so as to minimize the required number of shots. This is achieved by minimizing the rank of the matrix containing the set of codes $\mathbf{t}^i$. The optimized set of coded apertures leads to spectrally selective compressed measurements with improved characteristics for meeting Restricted Isometry Property (RIP) of the projections used in CASSI. The compressed measurements are then used to reconstruct the desired spectral cube using a gradient based reconstruction algorithm for sparse signals.

Notation: The following font notation is used hereafter. Bold uppercase Roman and Greek letters represent matrices. Bold lower case Roman and Greek letters represent column vectors. The entries of the matrix $\mathbf{Y}$ are Y_{ij} or $(\mathbf{Y})_{ij}$ and the entries of the vector $\mathbf{y}$ are y_j or $(\mathbf{y})_j$. Subindices, upper indices and calligraphic fonts are used to represent distinct variables. Hence, the variables $\mathbf{y}_V$ and $\mathbf{y}_V^k$ are distinct column vectors. The variables $\mathbf{Y}_i$ and $\mathbf{y}_i$ for different i are distinct matrices and column vectors respectively. $\mathbf{y}^T$ is a row vector and $\mathbf{Y}^T$ is the transpose of the matrix $\mathbf{Y}$. The power of a matrix is presented using parenthesis, thus the power two of the matrix $\mathbf{\Theta}_L$ is $(\mathbf{\Theta}_L)^2$.

3.2 Matrix-Based CASSI Modeling

The coded aperture single shot spectral imaging system is depicted in Fig. 2.3 [**?**]. The coding is realized by the coded aperture $T(x, y)$ as applied to the spatio-spectral density source $f_0(x, y, \lambda)$ where (x, y) are the spatial coordinates and λ is the wavelength resulting in the coded field $f_1(x, y, \lambda)$. The coded density is spectrally dispersed by a dispersive element before it impinges on the focal plane array (FPA) as $f_2(x, y, \lambda)$,

$$f_2(x,y,\lambda)=\iint T(x',y')f_0(x',y',\lambda)h(x'-\alpha\lambda-x,y'-y)dx'dy'$$

where $T(x', y')$ is the transmission function representing the coded aperture, $h(x' - \alpha\lambda - x, y' - y)$ is the optical impulse response of the system, and $\alpha\lambda$ is the dispersion induced by the prism assuming a linear dispersion. Each spectral slice of the data cube is thus spatially modulated by the coded aperture and dispersed by the dispersive element [**?**]. The compressive measurements across the FPA are realized by the integration of the field $f_2(x, y, \lambda)$ over the detector's spectral range sensitivity. The source $f_0(x, y, \lambda)$ can be written in discrete form as $\mathcal{F}_{ijk}$ where i and j index the spatial coordinates, and k determines the kth spectral plane. Assuming that the band-pass filter of the instrument limits the spectral components between λ_1 and λ_2 and the side length of the square detector pixel is Δ_d, the number of resolvable bands L is limited by $L = \alpha \frac{\lambda_2 - \lambda_1}{\Delta_d}$. The spectral resolution is limited by $\frac{\Delta_d}{\alpha}$. Additionally, it is assumed that the side length of the coded aperture square pixel Δ_c satisfies $\kappa\Delta_c = \Delta_d$, where $\kappa \geq 1$ is an integer.
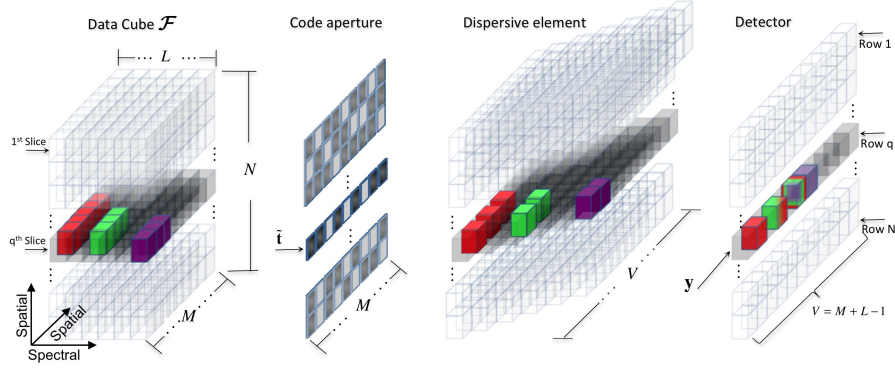
Figure 3.1: Illustration of the spectral data flow in CASSI. The qth slice of the data cube $\mathcal{F}$ with 11 spectral components is coded by a row of the coded aperture $\tilde{\mathbf{t}}$ and dispersed by the prism. The detector captures the intensity $\mathbf{y}$ by integrating the coded light.

The horizontal and vertical spatial resolutions are thus limited by Δ_d. The discretized output at the detector is given by

$$G_{jk} = \sum_{i=0}^{L-1} \mathcal{F}_{j(k+i)(k)} T_{j(k+i)} + \omega_{jk} \tag{3.1}$$

where G_{jk} is the intensity at the j, k position at the detector whose dimensions are $N \times (M + L - 1)$. $\mathcal{F}$ is an $L \times N \times M$ spectral data cube, T is the coded aperture and ω is the white noise of the sensing system. The output G_{jk} can be written in matrix notation as

$$\mathbf{y}_t = \mathbf{\Phi}\boldsymbol{f} + \boldsymbol{\omega} \tag{3.2}$$

where $\mathbf{y}_t$ is a vector representation of $\mathbf{G}$ and $\boldsymbol{f}$ is the vector representation of the data cube $\mathcal{F}$. Notice that $\boldsymbol{f}$ is represented as $\boldsymbol{f} = \mathbf{\Psi}_{3D}\boldsymbol{\rho}$ where $\boldsymbol{\rho}$ are the sparse coefficients of representation on the basis $\mathbf{\Psi}_{3D}$ [?]. In this Chapter, the coded aperture is considered binary and the dispersive element is considered linear. In practice, it is necessary take into account the various optical artifacts and non-ideal characteristic of the optical system. Observe in (3.1) that the spatial dimension j can be fixed to a specific value, for example $j = q$ represents the qth row measurement. In this case (3.1) would represent the model of a slice of CASSI. Figure 3.1 shows a typical slice model where a slice $\mathbf{F}$ of the data cube $\mathcal{F}$ is coded by the coded aperture $\tilde{\mathbf{t}}$, dispersed by the prism, and the resulting light is integrated at the detector resulting in the measurement $\mathbf{y}$. The vectorization of $\mathbf{F}$ is $\mathbf{f}$. Given the separability in slices of (3.1), a slice model of the instrument is developed first. The results are thereafter generalized to a complete 2D detector. Observe that the coded aperture effects are embedded in the matrix $\mathbf{\Phi}$ in (3.2), then a more suitable matrix-based model than that given by (3.2) needs to be developed in order to optimize the coded aperture. This is developed in the remainder of this section. To begin, let $\mathbf{\Theta}_L$ be the $L \times L$ cyclic permutation matrix

$$\mathbf{\Theta}_L = \begin{bmatrix} 0 & 0 & \ldots & 0 & 1 \\ 1 & 0 & \ldots & 0 & 0 \\ 0 & 1 & \ldots & 0 & 0 \\ \vdots & 0 & \ddots & 0 & 0 \\ 0 & 0 & \ldots & 1 & 0 \end{bmatrix}. \tag{3.3}$$

Next, define the matrix $\mathbf{J}_L$ as the $L \times L$ matrix having only one non-zero element in the coordinate $(1,1)$ as

$$\mathbf{J}_L = \begin{bmatrix} 1 & 0 & \ldots & 0 \\ 0 & 0 & \ldots & 0 \\ \vdots & \vdots & \ddots & 0 \\ 0 & 0 & \ldots & 0 \end{bmatrix}. \tag{3.4}$$

To simplify the notation define the matrix $\mathbf{P}_{L;k}$ as

$$\mathbf{P}_{L;k} = \mathbf{\Theta}_L^k \mathbf{J}_L (\mathbf{\Theta}_L^T)^k. \tag{3.5}$$

49
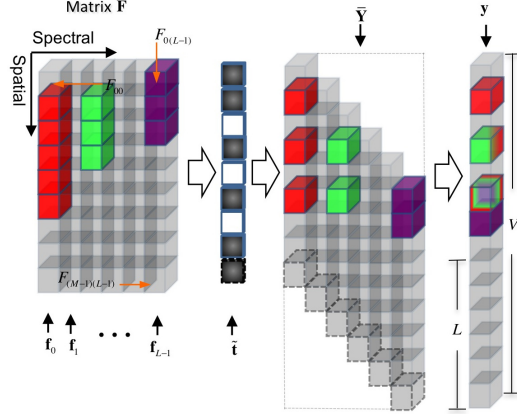
Figure 3.2: The qth slice of the data cube $\mathcal{F}$ is represented by the matrix $\mathbf{F}$. Each F_{jk} element is pictorially represented as a small cube where the gray color indicates a zero value.

Notice that multiple applications of the matrix in (3.3) perform the same cyclic permutation several times. The matrix $\mathbf{P}_{L;k}$ in (3.5) will be used to select an specific row or column of a matrix. Finally, define the reversing order matrix $\mathbf{C}$ as

$$\mathbf{C} = \begin{bmatrix} 0 & 0 & \ldots & 1 \\ \vdots & & \ddots & 0 \\ 0 & 1 & & \vdots \\ 1 & 0 & \ldots & 0 \end{bmatrix}. \tag{3.6}$$

3.2.1 Slice Model of the Spectral Data Cube

The qth slice of $\mathcal{F}$ is created as

$$F_{jk} = \mathcal{F}_{qjk} \quad j = 0, \ldots, M-1, \quad k = 0, \ldots, L-1. \tag{3.7}$$

Notice that each column of $\mathbf{F}$ contains spatial information at a given wavelength and each row of $\mathbf{F}$ consists of all spectral components at a specific spatial position. Figure 3.2 depicts a typical matrix $\mathbf{F}$ representing a slice of a spectral data cube and the respective elements present in CASSI. The kth column of $\mathbf{F}$ is denoted as $\mathbf{f}_k$, then the matrix $\mathbf{F}$ can be expressed as $\mathbf{F} = [\mathbf{f}_0, \mathbf{f}_1, \ldots, \mathbf{f}_{L-1}]$. Observe that $\mathbf{F}$ can be decomposed into L matrices as

$$\mathbf{F} = \sum_{k=0}^{L-1} \mathbf{F}_k \tag{3.8}$$

where $\mathbf{F}_k = [\overbrace{\mathbf{0}_M, \ldots, \mathbf{0}_M}^{k}, \mathbf{f}_k, \overbrace{\mathbf{0}_M, \ldots, \mathbf{0}_M}^{N-1-k}]$ and $\mathbf{0}_M$ is an M long column vector with zero elements. Observe that $\mathbf{F}_k$ can be written more succinctly as

$$\mathbf{F}_k = \mathbf{F}\mathbf{P}_{L;k} \tag{3.9}$$

where $\mathbf{P}_{L;k}$ is given in (3.5). The slice $\mathbf{F}$ can then be rewritten as

$$\mathbf{F} = \sum_{k=0}^{L-1} \mathbf{F}\mathbf{P}_{L;k}. \tag{3.10}$$

3.2.2 Coded Aperture Effect Model

Consider the slice $\mathbf{F}$ in (3.10) impinging on a row of the 2D coded aperture $\mathbf{T}$, as depicted in Fig. 3.1. This row of the coded aperture, represented by the vector $\tilde{\mathbf{t}} = \left[\tilde{t}_0, \ldots, \tilde{t}_{M-1}\right]$, modulates the columns of

F. The output after the coded aperture can be represented by $\overline{\mathbf{F}} = \mathbf{TF}$ where $\mathbf{T} = \mathrm{diag}\left(\tilde{t}_0, \ldots, \tilde{t}_{M-1}\right)$ is an $M \times M$ diagonal matrix containing the respective row of the coded aperture. As mentioned previously, the coded aperture $\tilde{\mathbf{t}}$ is defined as the Hadamard product of two vector components as $\tilde{\mathbf{t}} = \tilde{\mathbf{r}} \circ \tilde{\mathbf{w}}$, where $\tilde{\mathbf{r}} = [\tilde{r}_0, \ldots, \tilde{r}_{M-1}]$ accounts for a pseudorandom component and $\tilde{\mathbf{w}} = [\tilde{w}_0, \ldots, \tilde{w}_{M-1}]$ accounts for an adjustable component of $\tilde{\mathbf{t}}$. $\mathbf{T}$ can thus be expressed as $\mathbf{T} = \mathbf{RW}$ where $\mathbf{R} = \mathrm{diag}\left(\tilde{r}_0, \ldots, \tilde{r}_{M-1}\right)$ and $\mathbf{W} = \mathrm{diag}\left(\tilde{w}_0, \ldots, \tilde{w}_{M-1}\right)$. Figure 3.2 shows that in CASSI only L pixels at the detector are affected by a point source in the spectral data cube. More specifically, in Fig. 3.2 the component of the coded aperture $(\tilde{\mathbf{t}})_{M-1}$ with the dashed outline affects only L pixels at the detector $\mathbf{y}$. Hence, both the adjustable component $\tilde{\mathbf{w}}$ and the random component $\tilde{\mathbf{r}}$ can be modeled as L-long vectors repeated via a modulo operator to span the length M of the detector. More specifically the elements of $\tilde{\mathbf{w}}$ and $\tilde{\mathbf{r}}$ are calculated as

$$
\begin{aligned}
\tilde{w}_j &= w_{\mathrm{mod}_L(j)} & j &= 0, \ldots, M-1 \\
\tilde{r}_j &= r_{\mathrm{mod}_L(j)} & j &= 0, \ldots, M-1
\end{aligned}
\tag{3.11}
$$

where $\mathbf{w}$ and $\mathbf{r}$ are L-long vectors. Notice that the coded aperture elements can be expressed as $\tilde{t}_j = t_{\mathrm{mod}_L(j)}$ for $j = 0, \ldots, M-1$ where the vector $\mathbf{t}$ is $\mathbf{t} = \mathbf{r} \circ \mathbf{w}$. These vectors can thus be written as

$$
\begin{aligned}
\tilde{\mathbf{w}} &= \mathbf{u}_{M'} \otimes \mathbf{w} \\
\tilde{\mathbf{r}} &= \mathbf{u}_{M'} \otimes \mathbf{r} \\
\tilde{\mathbf{t}} &= \mathbf{u}_{M'} \otimes \mathbf{t}
\end{aligned}
\tag{3.12}
$$

where $\otimes$ is the Kronecker product, and $\mathbf{u}_{M'}$ is the one-valued vector of length $M' = \frac{M}{L}$[1]. From (3.12) $\mathbf{W}$ and $\mathbf{R}$ can be expressed as $\mathbf{W} = \mathrm{diag}\left(\mathbf{u}_{M'} \otimes \mathbf{w}\right)$ and $\mathbf{R} = \mathrm{diag}\left(\mathbf{u}_{M'} \otimes \mathbf{r}\right)$. The matrix $\overline{\mathbf{F}}$, representing the coded slice $\mathbf{F}$, can thus be expressed as

$$
\overline{\mathbf{F}} = \mathbf{RWF}.
\tag{3.13}
$$

3.2.3 Dispersive Element Effect Model

Given the matrix representation of the coded slice at the source in (3.13), here we show the effect of the dispersive element over this matrix. Observe that each column of $\overline{\mathbf{F}}$ represents a given spectral band spatially coded by the coded aperture. The effect of the dispersive element can then be modeled as a shift of each column of $\overline{\mathbf{F}}$ in k units where k expresses the kth wavelength (column). Further, the matrix $\overline{\mathbf{F}}$ needs to be augmented by $L - 1$ rows to correctly model the prism's effect. Let the matrix $\overline{\mathbf{Y}}$ model the output of the dispersive element when the input is the matrix $\overline{\mathbf{F}} = \left[\overline{\mathbf{f}}_0, \ldots, \overline{\mathbf{f}}_{L-1}\right]$ in (3.13). $\overline{\mathbf{Y}}$ is then given by

$$
\overline{\mathbf{Y}} =
\begin{bmatrix}
\overline{\mathbf{f}}_0 & \mathbf{0}_1 & \ldots & \\
& \overline{\mathbf{f}}_1 & \ldots & \mathbf{0}_{L-1} \\
& & \ddots & \\
\mathbf{0}_{L-1} & \mathbf{0}_{L-2} & \ldots & \overline{\mathbf{f}}_{L-1}
\end{bmatrix}
\tag{3.14}
$$

where $\mathbf{0}_i = 0.\mathbf{u}_i$ is an $i-$long zero-valued column vector. Figure 3.2 illustrates the formation of $\overline{\mathbf{Y}}$. Define V as $V = M + L - 1$. In order to express the matrix $\overline{\mathbf{Y}}$ compactly, the $V \times L$ matrix $\overline{\mathbf{F}}_k$ is defined as

$$
\overline{\mathbf{F}}_k =
\begin{bmatrix}
\mathbf{0}_{V \times k} & \begin{matrix} \overline{\mathbf{f}}_k \\ \mathbf{0}_{(L-1) \times 1} \end{matrix} & \mathbf{0}_{V \times (L-k-1)}
\end{bmatrix}
\tag{3.15}
$$

where $\mathbf{0}_{V \times k}$ and $\mathbf{0}_{V \times (L-k-1)}$ are matrices of $V \times k$ and $V \times (L - k - 1)$ zero elements respectively. Then the matrix $\overline{\mathbf{Y}}$ can be written as

$$
\overline{\mathbf{Y}} = \sum_{k=0}^{L-1} (\boldsymbol{\Theta}_V)^k \overline{\mathbf{F}}_k
\tag{3.16}
$$

---

[1]If $\frac{M}{L}$ is not an integer then the first $L\left\lfloor \frac{M}{L} \right\rfloor$ elements of $\tilde{\mathbf{w}}$ and $\tilde{\mathbf{r}}$ are given by (3.12) and the remaining by, $\tilde{w}_j = w_{j-L}$, and $\tilde{r}_j = r_{j-L}$ for $j = L\left\lfloor \frac{M}{L} \right\rfloor, \ldots, M-1$.

where the $V \times V$ matrix $\boldsymbol{\Theta}_V$ has the same purpose and structure of $\boldsymbol{\Theta}_L$ in (3.3). Defining the matrix $\bar{\mathbf{I}}$ as

$$\bar{\mathbf{I}} = \begin{bmatrix} \mathbf{I}_{M \times M} \mathbf{0}_{M \times (L-1)} \end{bmatrix}^T \tag{3.17}$$

where $\mathbf{I}_{M \times M}$ is an $M \times M$ identity matrix, $\overline{\mathbf{F}}_k$ in (3.15) can be expressed as

$$\overline{\mathbf{F}}_k = \bar{\mathbf{I}} \mathbf{R} \mathbf{W} \mathbf{F}_k \tag{3.18}$$

where $\mathbf{F}_k$ is given by (3.9). Replacing (3.9) and (3.18) in (3.16) the matrix representation of the prism effect on $\mathbf{F}$ is

$$\overline{\mathbf{Y}} = \sum_{k=0}^{L-1} (\boldsymbol{\Theta}_V)^k \bar{\mathbf{I}} \mathbf{R} \mathbf{W} \mathbf{F} \mathbf{P}_{L;k}. \tag{3.19}$$

Observe that the jth row of $\overline{\mathbf{Y}}$ contains the spectral information that is integrated in the jth pixel detector.

Table 3.1: CASSI Equations Model Summary.

	Dimensions	Complementary Equations
Data Cube		
Full Data Cube $\mathcal{F}$	$N \times M \times L$	$F_{jk} = \mathcal{F}_{qjk},$
Slice $\mathbf{F} = \sum_{k=0}^{L-1} \mathbf{F} \mathbf{P}_{L;k}$	$M \times L$	$\mathbf{F} = [\mathbf{f}_0 \dots \mathbf{f}_{L-1}].$
Coded Aperture		
2D Coded Aperture $\mathbf{T}$	$N \times M$	$\mathbf{R} = \mathrm{diag}\,(\tilde{\mathbf{r}}), \mathbf{W} = \mathrm{diag}\,(\tilde{\mathbf{w}}),$
Slice Coded Aperture $\mathbf{t}$	L	$\mathbf{T} = \mathbf{R} \mathbf{W}, \tilde{\mathbf{w}} = \mathbf{u}_{M'} \otimes \mathbf{w},$
Random Component $\mathbf{r}$	L	$\tilde{\mathbf{r}} = \mathbf{u}_{M'} \otimes \mathbf{r}, \tilde{\mathbf{t}} = \mathbf{u}_{M'} \otimes \mathbf{t},$
Designable Component $\mathbf{w}$	L	$\mathbf{t} = \mathbf{r} \circ \mathbf{w}.$
Coded Aperture Output $\overline{\mathbf{F}} = \mathbf{R} \mathbf{W} \mathbf{F}$	$M \times L$	
Prism Output		$V = M + L - 1$
$\overline{\mathbf{Y}} = \sum_{k=0}^{L-1} (\boldsymbol{\Theta}_M)^k \bar{\mathbf{I}} \mathbf{R} \mathbf{W} \mathbf{F} \mathbf{P}_{L;k}$	$V \times L$	$\mathbf{P}_{L;k} = \boldsymbol{\Theta}_L^k \mathbf{J}_L (\boldsymbol{\Theta}_L^T)^k.$
Detector Output , two versions:		
$\mathbf{y} = \sum_{j=0}^{V-1} \mathbf{P}_{V;j} \sum_{k=0}^{L-1} (\boldsymbol{\Theta}_V)^k \bar{\mathbf{I}} \mathbf{F} \mathbf{P}_{L;k} \mathbf{C} (\boldsymbol{\Theta}_L^T)^{j+1} \mathbf{t}$	V	
$\mathbf{y} = \sum_{j=0}^{V-1} \mathbf{P}_{V;j} \sum_{k=0}^{L-1} (\boldsymbol{\Theta}_V)^k \bar{\mathbf{I}} \mathbf{R} \mathbf{F} \mathbf{P}_{L;k} \mathbf{C} (\boldsymbol{\Theta}_L^T)^{j+1} \mathbf{w}$	V	

3.2.4 Detector Measurements

The detector integrates all coded light that comes from the dispersive element. The vector of intensities at the detector can be calculated as

$$\mathbf{y} = \overline{\mathbf{Y}} \mathbf{u}_L \tag{3.20}$$

where $\mathbf{u}_L$ is a one-valued L long vector. Substituting (3.19) in (3.20), we obtain

$$\mathbf{y} = \sum_{k=0}^{L-1} (\boldsymbol{\Theta}_V)^k \bar{\mathbf{I}} \mathbf{R} \mathbf{W} \mathbf{F} \mathbf{P}_{L;k} \mathbf{u}_L. \tag{3.21}$$

Property 1 *Given a slice* $\mathbf{F}$ *as input to CASSI impinging onto the slice aperture code* $\mathbf{t}$*, the FPA measurement at the detector is*

$$\mathbf{y} = \sum_{j=0}^{V-1} \mathbf{P}_{V;j} \sum_{k=0}^{L-1} (\boldsymbol{\Theta}_V)^k \bar{\mathbf{I}} \mathbf{F} \mathbf{P}_{L;k} \mathbf{C} (\boldsymbol{\Theta}_L^T)^{j+1} \mathbf{t}. \tag{3.22}$$

Equivalently, the output is given by

$$\mathbf{y} = \sum_{j=0}^{V-1} \mathbf{P}_{V;j} \sum_{k=0}^{L-1} (\boldsymbol{\Theta}_V)^k \bar{\mathbf{I}} \mathbf{R} \mathbf{F} \mathbf{P}_{L;k} \mathbf{C} (\boldsymbol{\Theta}_L^T)^{j+1} \mathbf{w}, \tag{3.23}$$

where $\mathbf{P}_{V;j}$*,* $\boldsymbol{\Theta}_M$*,* $\bar{\mathbf{I}}$*,* $\mathbf{P}_{L;k}$*,* $\mathbf{C}$*, and* $\boldsymbol{\Theta}_L$ *are the shifting matrices defined in* (3.5)*,* (3.3)*,* (3.17)*, and* (3.6)*.*

Observe that (3.22) is specially suitable for the design of the coded aperture $\mathbf{t}$ since $\mathbf{t}$ appears at the right most element in (3.22). In contrast, the most right element in (3.23) is $\mathbf{w}$. Hence, Eq. (3.23) can be used to design the component $\mathbf{w}$ of the coded aperture when the random component $\mathbf{r}$ is assumed to remain fixed. Table 3.1 summarizes the principal results of the slice CASSI model.
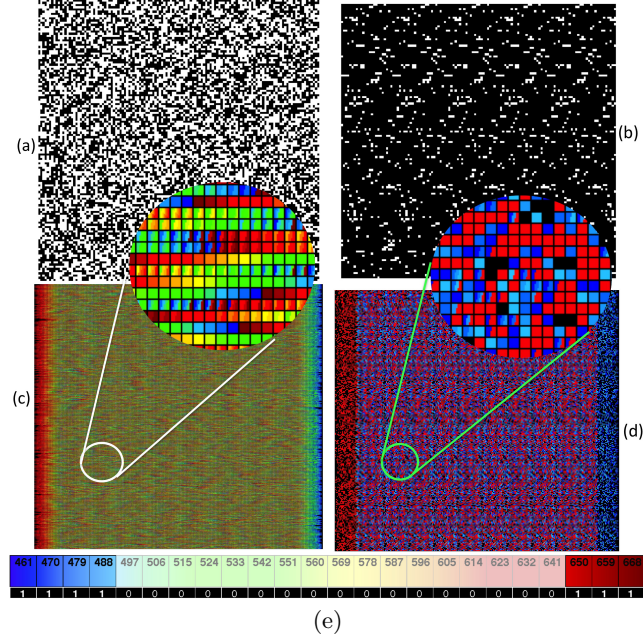
Figure 3.3: (a) A random coded aperture and (b) a spectrally selective optimal coded aperture for a 12 shot CASSI system. The corresponding FPA measurements are shown in (c) and (d). The zoomed areas illustrate the wavelengths present at each pixel measurement where the spectral selectivity of the optimal codes is clearly seen. The desired spectral profile $\boldsymbol{\lambda} \in [461\text{nm} - 471\text{nm}, \quad 641\text{nm} - 668\text{nm}]$ is illustrated in (e).

3.3 Optimal Codes for Spectral Band Selectivity

Spectral selectivity aims at designing coded aperture sets that obtain compressive measurements with only information from a given set of bands of interest. Furthermore, the optimization aims at the use of the smallest number of measurements. Figure 3.3 illustrates a sample of a spectrally selective optimal coded aperture and the respective FPA measurement. There, it is possible to observe that the FPA spectrally selective measurement contains only wavelengths from a specific set of bands. In particular, observe that each pixel in the zoom area in Fig 3.3(d) contains exclusively spectral components in the range $[461\text{nm} - 471\text{nm}, \quad 641\text{nm} - 668\text{nm}]$. In contrast, the zoom area in Fig. 3.3(c) shows that a CASSI measurement using random codes contains spectral components of the whole wavelength range. The coded aperture design developed hereafter can be summarized as follows: A) Obtain an expression for the desired spectrally selective compressive measurement signal $\mathbf{d}$ from the observation spectral image slice $\mathbf{F}$. B) Determine a set of K optimal weights $\{\mathbf{w}_{\alpha_j}\}_{j=0}^{K-1}$ such that the vector $\mathbf{g}_0 = \mathbf{d}$ can be constructed from the respective K compressive measurements $\{\mathbf{y}_{\alpha_j}\}_{j=0}^{K-1}$. C) Generalize the results in (3.3) by incorporating the random components of the coded aperture $\mathbf{r}_{\alpha_j}$ such that the set $\{\mathbf{g}_j\}_{j=0}^{\mathcal{U}-1}$ containing $\mathcal{U}$ different realizations of the desired signal $\mathbf{d}$ can be estimated. D) Optimize the realizations of the pseudorandom components $\mathbf{r}_{\alpha_j}$ such that the number of shots K in (3.3) is further reduced to a desired number $K' \leq K$.

3.3.1 Desired Compressive Measurements

The reference compressive measurement signal $\mathbf{d}$ is created by zeroing out all spectral bands at the input except those that are desired. More specifically, define the L long vector $\boldsymbol{\lambda}$ indexing the desired spectral bands as

$$\lambda_k = \begin{cases} 1 & \text{if the } k^{th} \text{ spectral band is of interest} \\ 0 & \text{otherwise.} \end{cases} \qquad (3.24)$$

Furthermore, let $\mathcal{L} = \|\boldsymbol{\lambda}\|_0$ be the number of desired bands, define the index of the jth nonzero component of $\boldsymbol{\lambda}$ as ϵ_j, and let $\boldsymbol{\Lambda} = \text{diag}\,(\lambda_0, \ldots, \lambda_{L-1})$ be the diagonal matrix containing the desired band indices

in (3.24). Given the slice $\mathbf{F}$, the matrix $\mathbf{F}\boldsymbol{\Lambda}$ contains only the spectral information from the desired bands. Fixing the random component $\mathbf{r}$ and making $\mathbf{w} = \mathbf{u}_L$, $\mathbf{y}$ in (3.23) results in the output containing the information from the spectral data cube $\mathbf{F}$ coded by the random component $\mathbf{r}$. In addition, if $\mathbf{F}$ is replaced by $\mathbf{F}\boldsymbol{\Lambda}$ then the output is a compressive spectral measurement containing only information of the spectral bands of interest coded by $\mathbf{r}$. More specifically, using (3.23) the desired output is

$$\mathbf{d} = \sum_{j=0}^{V-1} \mathbf{P}_{V;j} \sum_{k=0}^{L-1} (\boldsymbol{\Theta}_V)^k \bar{\mathbf{I}} \mathbf{RFP}_{L;k} \boldsymbol{\lambda}. \tag{3.25}$$

Notice that $\mathbf{d}$ in (3.25) is created by sensing the desired data cube $\mathbf{F}\boldsymbol{\Lambda}$ and by bypassing the effect of the coded aperture $\mathbf{w}$. The next sub-section aims at obtaining the same values of the vector $\mathbf{d}$ by sensing the complete data cube $\mathbf{F}$ using the CASSI system and by varying the term $\mathbf{w}$ in (3.23).

3.3.2 Coded Aperture Design for $\mathbf{w}$

Given the expressions for $\mathbf{y}$ and $\mathbf{d}$ in (3.23) and (3.25), respectively, the objective in the design of $\mathbf{w}$ in (3.23) is to make all the elements of $\mathbf{y}$ and $\mathbf{d}$ equal, where the random components of the coded aperture $\mathbf{r}$ are not yet considered, such that all the elements of $\mathbf{r}$ are set to one. In order to estimate the weights $\mathbf{w}$, the output in (3.23) is equated to that of the desired response in (3.25) resulting in

$$\boldsymbol{\lambda} = \mathbf{C}(\boldsymbol{\Theta}_L^T)^{j+1}\mathbf{w} \qquad j = 0, \ldots, V-1. \tag{3.26}$$

Solving (3.26) for $\mathbf{w}$ results in

$$\mathbf{w} = (\boldsymbol{\Theta}_L)^{j+1}\mathbf{C}^{-1}\boldsymbol{\lambda} \qquad j = 0, \ldots, V-1 \tag{3.27}$$

where it can be observed that a single vector $\mathbf{w}$ cannot satisfy (3.27) for all j. Hence, $V-1$ vectors must be used. Let these vectors be $\mathbf{w}_j$ for $j = 0, \ldots, V-1$. Let $\mathbf{y}_j$ be the CASSI output in (3.23) when the coded aperture $\mathbf{w}_j$ is used, then the element by element equality condition $(\mathbf{d})_j = (\mathbf{y})_j$ can be written as

$$(\mathbf{d})_j = (\mathbf{y}_j)_j \quad j = 0, \ldots, V-1. \tag{3.28}$$

Since $(\boldsymbol{\Theta}_L^T)^j = (\boldsymbol{\Theta}_L^T)^{j+L}$, then only L values of j are needed to be taken into account in (3.27), leading to

$$\mathbf{w}_j = (\boldsymbol{\Theta}_L)^{j+1}\mathbf{C}^{-1}\boldsymbol{\lambda} \qquad j = 0, \ldots, L-1$$

$$\mathbf{w}_{j+mL} = \mathbf{w}_j \qquad m = 0, 1 \ldots, \left\lfloor \frac{V}{L} \right\rfloor. \tag{3.29}$$

Consequently, (3.28) is modified to

$$(\mathbf{d})_j = (\mathbf{y}_{\text{mod}_L(j)})_j \quad j = 0, \ldots, V-1. \tag{3.30}$$

The condition in (3.30) can then be satisfied using L CASSI shots whose outputs are given by $\mathbf{y}_0, \ldots, \mathbf{y}_{L-1}$. Observe that some of coded apertures in (3.29) can be expressed as a linear combination of the others. Further, since $\mathbf{w}_j$ and $\mathbf{y}_j$ are linearly related, some of the outputs $\mathbf{y}_j$ can also be expressed as the linear combination of others. It is thus possible to calculate $\mathbf{d}$ in (3.30) using $K < L$ shots. To estimate the K linearly independent weight vectors, the coded apertures in (3.29) are arranged into the matrix $\mathbf{M}_w = [\mathbf{w}_0, \ldots, \mathbf{w}_{L-1}]$ or equivalently

$$\mathbf{M}_w = \left[\boldsymbol{\Theta}_L\mathbf{C}^{-1}\boldsymbol{\lambda}, (\boldsymbol{\Theta}_L)^2\mathbf{C}^{-1}\boldsymbol{\lambda}, \ldots, (\boldsymbol{\Theta}_L)^L\mathbf{C}^{-1}\boldsymbol{\lambda} \right]. \tag{3.31}$$

Then, the minimum number of shots K for a given set of bands of interest is the number of independent columns of $\mathbf{M}_w$. Hence,

$$K = \text{rank}\,(\mathbf{M}_w) \tag{3.32}$$

where rank($\mathbf{M}_w$) is the rank of the matrix $\mathbf{M}_w$. The K linear independent columns of $\mathbf{M}_w$ are the linear independent weight vectors $\mathbf{w}_{\alpha_k}$ for $k = 0, \ldots, K-1$. The remaining $L - K$ columns of $\mathbf{M}_w$ can be estimated using the ensemble of vectors $\boldsymbol{\mathcal{W}} = \left[\mathbf{w}_{\alpha_0}, \ldots, \mathbf{w}_{\alpha_{K-1}} \right]$. The jth vector $\mathbf{w}_j$ in (3.29) can be expressed as

$$\mathbf{w}_j = \sum_{k=0}^{K-1} \mathcal{C}_{kj}\mathbf{w}_{\alpha_k} \quad \text{for} \quad j = 0, \ldots, L-1 \tag{3.33}$$

where the coefficients $\mathcal{C}_{kj}$ are the elements of $\boldsymbol{\mathcal{C}} = \left(\boldsymbol{\mathcal{W}}^T\boldsymbol{\mathcal{W}} \right)^{-1} \boldsymbol{\mathcal{W}}^T\mathbf{M}_w$.

3.3.3 Spectrally Selective Image Measurements

Given the optimal coded aperture set $\boldsymbol{\mathcal{W}} = \left[\mathbf{w}_{\alpha_0}, \ldots, \mathbf{w}_{\alpha_{K-1}}\right]$ and the corresponding CASSI measurements of a scene $\mathbf{y}_{\alpha_0}, \ldots, \mathbf{y}_{\alpha_{K-1}}$, the goal is to re-order these measurements and select the entries which contain only the bands of interest. It turns out that the redundant representation of the weights shown in (3.33) provides a simpler structure in which to identify the entries of interest. To this end, the set of measurements $\{\mathbf{y}_{\alpha_j}\}_{j=0}^{K-1}$ is expanded into the set

$$\mathbf{y}_j = \sum_{k=0}^{K-1} \mathcal{C}_{kj} \mathbf{y}_{\alpha_k} \quad j = 0, \ldots, L-1 \tag{3.34}$$

where (3.34) uses the fact that there exists a linear relation between $\mathbf{w}_j$ and $\mathbf{y}_j$. Note that in obtaining (3.34), we are not taking additional measurements, we are only combining entries of the existing set of measurements $\{\mathbf{y}_{\alpha_j}\}$. Once the expanded measurement vectors $\{\mathbf{y}_j\}$ are available, the elements within this set that contain only the spectral component of interest must be identified. Let $\{\mathbf{g}_j\}_{j=0}^{K-1}$ be the K possible measurement vectors that satisfy the above condition obtained by selecting elements in (3.34). Property 2 describes the structure of the first vector $\mathbf{g}_0$.

Property 2 *Let $\mathbf{Z} = [\mathbf{y}_0, \ldots, \mathbf{y}_{L-1}]$ be the ensemble matrix containing the expanded measurements vectors in (3.34). The vector $\mathbf{g}_0 \in \mathbb{R}^V$ obtained from $\mathbf{Z}$ as $(\mathbf{g}_0)_i = (\mathbf{Z})_{i \bmod_L(i)}$ or equivalently $(\mathbf{g}_0)_i = (\mathbf{y}_{\bmod_L(i)})_i$ for $i = 0, \ldots, V-1$ contains measurements with spectral component of interest only, regardless of the value taken by the pseudorandom component $\mathbf{r}$.*

Proof: 1 *When the pseudorandom component is taken into account Eq. (3.27) is rewritten as*

$$\boldsymbol{\lambda} \circ \mathbf{r} = \mathbf{r} \circ \mathbf{C}(\boldsymbol{\Theta}_L^T)^{j+1}\mathbf{w} \qquad j = 0, \ldots, V-1. \tag{3.35}$$

The optimal set of weights when the pseudorandom component is taken into account is given by solving (3.35). Notice that if the set of vectors $\{\mathbf{w}_j\}_0^{L-1}$ solve (3.27) then they also solve (3.35). Hence, the optimal set of weights calculated without taking into account the random components can be used to solve (3.35). Consequently, equations (3.29) and (3.30) which were derived from (3.27) are valid regardless of the values taken by the pseudorandom components. From (3.30), note that $(\mathbf{d})_0 = (\mathbf{y}_0)_0$, $(\mathbf{d})_1 = (\mathbf{y}_1)_1$, and so on, such that it is possible to construct a selective measurement using the set $\{\mathbf{y}_i\}$. Let $\mathbf{g}_0$ be the selective measurement whose elements are given by

$$\mathbf{g}_0 = \left[y_{00}, y_{11}, \ldots, y_{(L-1)(L-1)}, y_{(0)L}, y_{1(L+1)}, \right.$$
$$\left. \ldots, y_{\bmod_L(V-1)(V-1)}\right]^T \tag{3.36}$$

where the element y_{ji} is $y_{ji} = (\mathbf{y}_j)_i$. Given the matrix $\mathbf{Z}$, Eq. (3.36) can be seen as $(\mathbf{g}_0)_i = (\mathbf{Z})_{i \bmod_L(i)}$ for $i = 0, \ldots, V-1$.

Note that the elements in $\mathbf{g}_0$ are the diagonal entries in $\mathbf{Z}$ as illustrated in Fig. 3.4(a). It is important to point out that many other elements in $\mathbf{Z}$ contain spectral components of interest, in addition to other spectral components that are not of interest. Note however that these undesirable spectral components may disappear, in some cases, when the pseudorandom component of the coded aperture is taken into account. In fact, the pseudorandom structure of $\mathbf{r}$ can be designed to improve the measurement process as described in Section 3.3.4. Figure 3.4 illustrates this observation where Fig. 3.4(a) depicts the elements in $\mathbf{Z}$ which contain spectral components of interest, regardless of the value taken by $\mathbf{r}$. Figure 3.4(b) depicts the elements in $\mathbf{Z}$ which contain spectral components of interest only, when $\mathbf{r}$ is taken into account and where $\mathbf{r}$ is a realization of a Bernoulli random variable with parameter $p = 0.6$. Note that the elements in Fig. 3.4(a) form a subset of the elements in Fig. 3.4(b). Figure 3.4(c) illustrates the elements of interest when $\mathbf{r}$ is a realization of a Bernoulli random variable with parameter $p = 0.3$. Note that as p decreases, the number of elements in $\mathbf{Z}$ containing the bands of interest increases. It will be shown shortly that an optimal p is obtained in the optimization of the codes. The entries in $\mathbf{Z}$ depicted in Fig. 3.4(a) are used to form the vector $\mathbf{g}_0$. Next, a procedure to select the entries depicted in Fig. 3.4(b)-(c) which were not already used in $\mathbf{g}_0$, is identified. Define the set of vectors $\boldsymbol{\lambda}_{i\ell}$ as

$$\boldsymbol{\lambda}_{i\ell} = \mathbf{C}(\boldsymbol{\Theta}_L^T)^{i+1}(\mathbf{w}_\ell \circ \mathbf{r}_\ell) \tag{3.37}$$
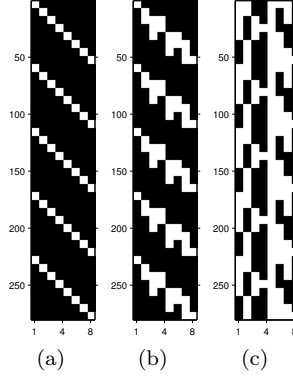
Figure 3.4: Three different versions of the $V \times L$ matrix $\mathbf{Z}$ as the value of p decreases. The elements available to construct the set of optimal measurements $\mathbf{d}_0, \ldots, \mathbf{d}_{\mathcal{U}}$ are shown in white squares representing elements containing only the desired bands. (a) The pseudorandom component is not considered, $p = 1$. The pseudorandom component is a realization of a Bernoulli variable with parameter (b) $p = 0.6$ and (c) $p = 0.3$. In this example: $L = 8$, $V = 280$.

Table 3.2: Spectral Selectivity Equations Summary.

	Size	Complementary Equations
Vector of desired bands, $\boldsymbol{\lambda}$	L	$\lambda_{\epsilon_k} = 1$, 0 otherwise. $\qquad \|\boldsymbol{\lambda}\|_0 = \mathcal{L}$
Optimal weight apertures $\mathbf{w}_j = (\boldsymbol{\Theta}_L)^{j+1}\mathbf{C}^{-1}\boldsymbol{\lambda}$	L	K Linearly independent columns
Matrix of weights		of $\mathbf{M}_w$: $\mathbf{w}_{\alpha_j}$
$\mathbf{M}_w = [\mathbf{w}_0, \ldots, \mathbf{w}_{L-1}]$	$L \times L$	$K = \text{rank}(\mathbf{M}_w)$
Optimized measurements $\mathbf{g}_j = \sum_{k=0}^{\mathcal{L}-1} \text{diag}(\mathbf{n}_{jk})\tilde{\mathbf{f}}_k$	V	$\{\tilde{\mathbf{t}}_j = \mathbf{u}_{M'} \otimes (\mathbf{r}_j \circ \mathbf{w}_j)\}_{j=0}^{L-1}$ $\{\tilde{\mathbf{t}}_j\}_{j=0}^{L-1} \rightarrow \{\tilde{\mathbf{t}}_j^{\epsilon_k}\}_{j=0,k=0}^{\mathcal{U}-1,\mathcal{L}-1}$ $\mathbf{n}_{jk} \triangleq (\boldsymbol{\Theta}_V)^{\epsilon_k}\bar{\mathbf{I}}(\tilde{\mathbf{t}}_j^{\epsilon_k})$ $\tilde{\mathbf{f}}_k \triangleq (\boldsymbol{\Theta}_V)^{\epsilon_k}\bar{\mathbf{I}}\mathbf{f}_{\epsilon_k}$
Ensemble of measurements $\left[\mathbf{g}_0^T, \ldots, \mathbf{g}_{\mathcal{U}-1}^T\right]^T = \boldsymbol{\mathcal{H}}\mathbf{b}$ $\boldsymbol{\mathcal{H}} = \left[\boldsymbol{\mathcal{H}}_0^T, \ldots, \boldsymbol{\mathcal{H}}_{\mathcal{U}-1}^T\right]^T$	$V \times \mathcal{U}$	$\left[\tilde{\mathbf{f}}_0, \ldots, \tilde{\mathbf{f}}_{\mathcal{L}-1}\right] = \boldsymbol{\Psi}\mathbf{b}$ $\boldsymbol{\mathcal{H}}_j = \sum_{k=0}^{\mathcal{L}-1}([1,0,\ldots,0]\boldsymbol{\Theta}_L^{\epsilon_k}) \otimes \ldots$ $\ldots \text{diag}(\mathbf{n}_{jk})\boldsymbol{\Psi}; \quad \mathbf{g}_j = \boldsymbol{\mathcal{H}}_j\mathbf{b}$

for $i = 0, \ldots, V - 1$ and $\ell = 0, \ldots, L - 1$, which indicates the spectral bands present in the $(i, \ell)^{th}$ entry of the matrix $\mathbf{Z}$. Using these vectors, the set of spectrally selective measurements $\{\mathbf{g}_j\}_{j=1}^{K-1}$ is obtained by forming the vectors $\mathbf{g}_j$ as

$$(\mathbf{g}_j)_i = \begin{cases} Z_{i\ell} & \{\exists \ell \in \{0, \ldots, L-1\} : \boldsymbol{\lambda}_{i\ell} \vee \boldsymbol{\lambda} - \boldsymbol{\lambda} = \mathbf{0} \\ 0 & \text{otherwise} \end{cases} \tag{3.38}$$

where $\mathbf{0}$ is a L-long zero valued vector and it is assumed that the elements of $\mathbf{Z}$ used to construct $\mathbf{g}_{j_1}$ are not used to construct $\mathbf{g}_{j_2}$ for $j_1 < j_2$. Notice that the number of linearly independent vectors in the set $\{\mathbf{g}_j\}_{j=0}^{K-1}$ is less or equal than K. Define the selectable parameter $\mathcal{U}$ as the number of the spectrally selective measurements. Then, the set of selective measurements is limited to $\{\mathbf{g}_j\}_{j=0}^{\mathcal{U}-1}$ where $\mathcal{U} \leq K$. The set of spectrally selective measurements $\{\mathbf{g}_j\}_{j=0}^{\mathcal{U}-1}$ in (3.36) and (3.38) can be interpreted as the output of a modified CASSI system similar to that in (3.21), with the difference that each spectral image slice $\mathbf{f}_k$ at the kth wavelength, is coded by a different coded aperture $\tilde{\mathbf{t}}^k$. This process is different than that of the traditional CASSI in (3.21) where each $\mathbf{f}_k$ is coded by the same coded aperture $\tilde{\mathbf{t}}$. Property 3 describes the above characteristic in the modified CASSI.

Property 3 *Given the set of spectral bands $\{\mathbf{f}_k\}_{k=0}^{L-1}$, the matrices $\boldsymbol{\Theta}_V$ and $\bar{\mathbf{I}}$ in (3.3) and (3.17), the set of weights $\{\mathbf{w}_j\}_{j=0}^{L-1}$ in (3.33), the set of vectors $\{\mathbf{r}_j\}_{j=0}^{L-1}$ representing realizations of a Bernoulli random variable, and given the set of coded apertures $\{\tilde{\mathbf{t}}_j = \mathbf{u}_{M'} \otimes (\mathbf{r}_j \circ \mathbf{w}_j)\}_{j=0}^{L-1}$, the set of selective measurements*

$\{\mathbf{g}_j\}_{j=0}^{\mathcal{U}-1}$ can be expressed as

$$\mathbf{g}_j = \sum_{k=0}^{L-1}(\boldsymbol{\Theta}_V)^k\bar{\mathbf{I}}\operatorname{diag}(\tilde{\mathbf{t}}_j^k)\mathbf{f}_k \tag{3.39}$$

where $(\tilde{\mathbf{t}}_j^k)_i = (\tilde{\mathbf{t}}_\ell)_i$ for some $\ell \in \{0, \ldots, L-1\}$.

Proof: 2 *Consider* $\mathbf{g}_0$ *first. Using* (3.21) *and observing that* $\mathbf{FP}_{L;k}\mathbf{u}_L = \mathbf{f}_k$, *and* $\mathbf{RW} = \operatorname{diag}(\tilde{\mathbf{t}}_i)$, *the measurements* $\mathbf{y}_j$ *can be written as*

$$\mathbf{y}_j = \sum_{k=0}^{L-1}(\boldsymbol{\Theta}_V)^k\bar{\mathbf{I}}\operatorname{diag}(\tilde{\mathbf{t}}_j)\mathbf{f}_k \tag{3.40}$$

for $j = 0, \ldots, L-1$. *Observe that* (3.40) *is the traditional CASSI model where each spectral band* $\mathbf{f}_k$ *is coded by the same code* $\tilde{\mathbf{t}}_j$. *Using* (3.40), *the equality* $(\mathbf{g}_0)_i = (\mathbf{y}_{\mathrm{mod}_L(i)})_i$ *in Property 2 can be written as*

$$
\begin{aligned}
(\mathbf{g}_0)_i &= \left(\sum_{k=0}^{L-1}(\boldsymbol{\Theta}_V)^k\bar{\mathbf{I}}\operatorname{diag}(\tilde{\mathbf{t}}_{\mathrm{mod}_L(i)})\mathbf{f}_k\right)_i \\
&= \sum_{k=0}^{L-1}\left((\boldsymbol{\Theta}_V)^k\bar{\mathbf{I}}\operatorname{diag}(\tilde{\mathbf{t}}_{\mathrm{mod}_L(i)})\mathbf{f}_k\right)_i \\
&= \sum_{k=0}^{L-1}\left(\operatorname{diag}(\tilde{\mathbf{t}}_{\mathrm{mod}_L(i)})\mathbf{f}_k\right)_{i-k} \\
&= \sum_{k=0}^{L-1}\left(\tilde{\mathbf{t}}_{\mathrm{mod}_L(i)}\right)_{i-k}(\mathbf{f}_k)_{i-k}.
\end{aligned}
\tag{3.41}
$$

Defining the L-long vectors $\tilde{\mathbf{t}}_0^k$ *as* $(\tilde{\mathbf{t}}_0^k)_i = (\tilde{\mathbf{t}}_{\mathrm{mod}_L(i)})_{i-k}$ *for* $k = 0, \ldots, L-1$ *and* $i = 0, \ldots, V-1$, *then* (3.41) *can be written as* $(\mathbf{g}_0)_i = \sum_{k=0}^{L-1}(\tilde{\mathbf{t}}_0^k)_i(\mathbf{f}_k)_{i-k} = \sum_{k=0}^{L-1}((\boldsymbol{\Theta}_V)^k\bar{\mathbf{I}}\mathbf{f}_k)_i(\mathbf{t}_0^k)_i$. *Hence,*

$$\mathbf{g}_0 = \sum_{k=0}^{L-1}(\boldsymbol{\Theta}_V)^k\bar{\mathbf{I}}\operatorname{diag}\left(\mathbf{t}_0^k\right)\mathbf{f}_k. \tag{3.42}$$

Note that each spectral band $\mathbf{f}_k$ *in* (3.42) *is coded by a different equivalent coded aperture* $\tilde{\mathbf{t}}_0^k$. *Similar expressions to that in* (3.42) *can be found for* $\mathbf{g}_j$ *for* $j > 0$ *such that* $\mathbf{g}_j$ *can be written in terms of* $\tilde{\mathbf{t}}_j^k$. *In these cases, the vectors* $\tilde{\mathbf{t}}_j^k$ *depend on the set of random components* $\{\mathbf{r}_j\}_{j=0}^{L-1}$ *and thus a closed expression as* (3.42) *is not available, however, they can be computed using* (3.38).

The expression in (3.39) can be further simplified observing that the vector $\mathbf{g}_j$ only contains information from the $\mathcal{L}$ desired bands defined in (3.24) and indexed by the vector ϵ_j. Thus, the vectors $\mathbf{g}_j$ can be rewritten as

$$\mathbf{g}_j = \sum_{k=0}^{\mathcal{L}-1}(\boldsymbol{\Theta}_V)^{\epsilon_k}\bar{\mathbf{I}}\operatorname{diag}(\tilde{\mathbf{t}}_j^{\epsilon_k})\mathbf{f}_{\epsilon_k} \tag{3.43}$$

for $j = 0, \ldots, K-1$. Define the vectors $\mathbf{n}_{jk} \triangleq (\boldsymbol{\Theta}_V)^{\epsilon_k}\bar{\mathbf{I}}(\tilde{\mathbf{t}}_j^{\epsilon_k})$ and $\tilde{\mathbf{f}}_k \triangleq (\boldsymbol{\Theta}_V)^{\epsilon_k}\bar{\mathbf{I}}\mathbf{f}_{\epsilon_k}$, then $\mathbf{g}_j$ in (3.43) can be succinctly represented as

$$\mathbf{g}_j = \sum_{k=0}^{\mathcal{L}-1}\operatorname{diag}(\mathbf{n}_{jk})\tilde{\mathbf{f}}_k \tag{3.44}$$

for $j = 0, \ldots, \mathcal{U}-1$. Notice that $\mathbf{n}_{jk}$ and $\tilde{\mathbf{f}}_k$ in (3.44) are circular shifted versions of the vectors $\tilde{\mathbf{t}}_j^{\epsilon_k}$ and $\mathbf{f}_{\epsilon_k}$ respectively. The sparse representation of the ensemble of vectors $\tilde{\mathbf{f}} = \left[\tilde{\mathbf{f}}_0, \ldots, \tilde{\mathbf{f}}_{\mathcal{L}-1}\right]$ is $\tilde{\mathbf{f}} = \boldsymbol{\Psi}\mathbf{b}$. Then, the vectors $\mathbf{g}_j$ can be expressed as

$$\mathbf{g}_j = \boldsymbol{\mathcal{H}}_j\mathbf{b} \tag{3.45}$$

where $\boldsymbol{\mathcal{H}}_j = \sum_{k=0}^{\mathcal{L}-1}([1,0,\ldots,0]\boldsymbol{\Theta}_L^{\epsilon_k}) \otimes \mathrm{diag}(\mathbf{n}_{jk})\boldsymbol{\Psi}$. The ensemble of the vectors $\mathbf{g}_j$ can be expressed as

$$\begin{bmatrix} \mathbf{g}_0 \\ \vdots \\ \mathbf{g}_{\mathcal{U}-1} \end{bmatrix} = \overbrace{\begin{bmatrix} \boldsymbol{\mathcal{H}}_0 \\ \vdots \\ \boldsymbol{\mathcal{H}}_{\mathcal{U}-1} \end{bmatrix}}^{\boldsymbol{\mathcal{H}}} \mathbf{b}. \tag{3.46}$$

3.3.4 Design of the Pseudo-Random Components

The minimum number of shots K given by (3.32) assumes that the pseudorandom component $\mathbf{r}_j$ of the coded aperture $\mathbf{t}^j = \mathbf{w}_j \circ \mathbf{r}_j$ remains fixed. It is shown here that the number of shots can be further reduced if the pseudorandom component is optimized. The optimization is accomplished as follows. The Hadamard multiplication of both sides of (3.29) by $\mathbf{r}_j$ produces

$$\mathbf{r}_j \circ \mathbf{w}_j = \mathbf{r}_j \circ \left((\boldsymbol{\Theta}_L)^{j+1}\mathbf{C}^{-1}\boldsymbol{\lambda}\right) \tag{3.47}$$

$$\mathbf{t}_j = \mathbf{R}_j(\boldsymbol{\Theta}_L)^{j+1}\mathbf{C}^{-1}\boldsymbol{\lambda} \tag{3.48}$$

for $j = 0,\ldots,L-1$, where $\mathbf{R}_j = \mathrm{diag}\{\mathbf{r}_j\}$. Using (3.48), the matrix $\mathbf{M}_w$ in (3.31) can be generalized to include the pseudorandom components as

$$\begin{aligned} \mathbf{M}_t &= [\mathbf{t}_0 \ \ldots \ \mathbf{t}_{L-1}] \\ &= \left[\mathbf{R}_0\boldsymbol{\Theta}_L\mathbf{C}^{-1}\boldsymbol{\lambda}, \mathbf{R}_1(\boldsymbol{\Theta}_L)^2\mathbf{C}^{-1}\boldsymbol{\lambda},\ldots,\mathbf{R}_{L-1}(\boldsymbol{\Theta}_L)^L\mathbf{C}^{-1}\boldsymbol{\lambda}\right]. \end{aligned}$$

The objective of the optimization of the set of pseudorandom vectors $\{\mathbf{r}_0,\ldots,\mathbf{r}_{L-1}\}$ is to minimize the rank of $\mathbf{M}_t$ until a predetermined number of shots $K' < K$ is obtained. Some constraints are necessary in order to limit the search of the vectors $\mathbf{r}_j$. In our approach, we seek the vectors $\mathbf{r}_j$ such that the CASSI measurements better satisfy the Restricted Isometry Property (RIP) condition. The RIP is an important condition for compressive measurements which guarantees the robust recovery of the sparse data cube via l_1 minimization [?, ?, ?].
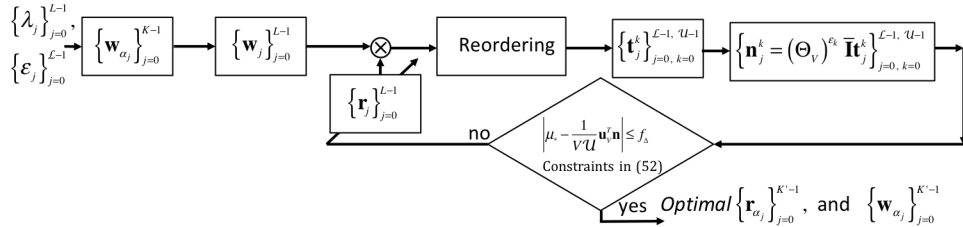
Figure 3.5: Optimization of the coded aperture process. Given the vector $\boldsymbol{\lambda}$, the optimization reduces the rank of the matrix $\mathbf{M}_t$ containing the set $\{\mathbf{w}_j \circ \mathbf{r}_j\}_{j=0}^{L-1}$ where the varying terms are the vectors $\mathbf{r}_j$. The optimization is constrained to satisfy the condition given in (3.50).

Property 4 *Given a set of spectral bands of interest* $\tilde{\mathbf{f}} = \left[\tilde{\mathbf{f}}_0,\ldots,\tilde{\mathbf{f}}_{\mathcal{L}-1}\right]$, *their sparse representation* $\tilde{\mathbf{f}} = \boldsymbol{\Psi}\mathbf{b}$, *assume that* $|\mathbf{b}| = S$, *given the matrix* $\boldsymbol{\mathcal{H}}$ *defined in (3.46), the vectors* $\mathbf{n}_{jk}$ *defined in (3.44), and the constants* $\delta_c \in (0,1)$ *and* $\epsilon \in [0.5,1]$, *then the probability*

$$\mathbb{P}\left((1-\delta_c)\parallel\mathbf{b}\parallel_2^2 \leq \parallel\boldsymbol{\mathcal{H}}\mathbf{b}\parallel_2^2 \leq (1+\delta_c)\parallel\mathbf{b}\parallel_2^2\right) = 1 - \epsilon$$

is higher when the constraints $\parallel\sum_{j=0}^{\mathcal{U}-1}\mathbf{n}_{jk}\parallel_0 \geq M$, *and* $\sum\sum_{k\neq\ell}\sum_{j=0}^{\mathcal{U}-1}\mathbf{n}_{jk}^T\mathbf{n}_{j\ell} = 0$ *for* $k,\ell = 0,\ldots,\mathcal{L}-1$ *are satisfied. Thus, if a CASSI model matrix* $\boldsymbol{\mathcal{H}}$ *satisfied the above condition with probability* $1 - \epsilon_1$ *and constant* δ_c *then that matrix can be optimized to satisfy the mentioned constraints such that the above condition is satisfied for the same constant* δ_c *with probability* $1 - \epsilon_2$ *where* $\epsilon_1 \geq \epsilon_2$.

The constraint $\| \sum_{j=0}^{\mathcal{U}} \mathbf{n}_{jk} \|_0 \geq M$ accounts for the necessary condition to reconstruct each spectral band $\tilde{\mathbf{f}}_k$. The constraint $\sum\sum_{k\neq\ell}\sum_{j=0}^{\mathcal{U}-1} \mathbf{n}_{jk}^T\mathbf{n}_{j\ell} = 0$ accounts for the joint reconstruction of the complete set of desired bands in the data cube $\tilde{\mathbf{f}}$. These two conditions are used as constraints in the optimization of the pseudorandom terms of the coded apertures.

Note that the ith element of the vector $\mathbf{n} = \sum_{j=0}^{\mathcal{U}-1} \sum_{\ell=0}^{\mathcal{L}-1} \mathbf{n}_{j\ell}$ represents the approximate number of spectral bands sensed at the ith location at the detector. This approximation comes from the correlation that exists among the vectors $\mathbf{n}_{j_1\ell}$ and $\mathbf{n}_{j_2\ell}$ for all ℓ and $j_1 \neq j_2$. Hence, the third constraint in the optimization is $n_i \neq 0$ for $i = 0, \ldots, V-1$. The fourth constraint in the optimization is the mean number μ_* of spectral components present in each pixel measurement at the detector. The parameter μ_*, referred as the optimal compressive ratio is a selectable term that indicates the average number of spectral components in each pixel measurement, and thus $\mu_* \geq 1$. The maximum mean number of spectral component by pixel detector can be estimated as

$$\mu_m = \frac{M\mathcal{L}}{V}. \tag{3.49}$$

where $M\mathcal{L}$ is the number of total variables and V is the number of effective pixel sensors in a line of the FPA. The optimal compressive ratio parameter μ_* range is thus $[1, \mu_m]$. In general, the mean number of spectral components by pixel can be estimated as: $\frac{1}{V\mathcal{U}}\mathbf{u}_V^T\mathbf{n}$, where $\mathbf{u}_V$ is a one-valued V long vector.

Table 3.3: Iterative Stochastic Algorithm to solve (3.50)**.**

Inputs	$\boldsymbol{\lambda}$, K', $\mathcal{U}$, $\Pr(.)$ is a random permutation, $rk(.) = rank(.)$.
Initialize	$\mathbf{w}_i = (\boldsymbol{\Theta}_L)^{i+1}\mathbf{C}^{-1}\boldsymbol{\lambda}$, $\mathbf{M} = [\mathbf{w}_0, \ldots, \mathbf{w}_{L-1}]$, $\boldsymbol{\mathcal{M}} = \mathbf{M}$,
	$\mathbf{B} = \{B_{kj} = \text{Bernoulli}(0.5) : \sum_{k=0}^{L-1} B_{kj} = 1 \; \forall j$,
	$\sum_{j=0}^{L-1} \| \sum_{j=0}^{L-1} B_{kj} \|_0 = K'\}$.
Loop-1	While, $\text{rk}(\boldsymbol{\mathcal{M}}) \neq K'$, $\quad \boldsymbol{\mathcal{M}} = \mathbf{M} \circ \mathbf{B}$. $\quad$ return to **Main**.
Loop-2A	$\mathbf{s} = \{s_j \in \{0, \ldots, L-1\} \; : \; \sum_{i=0}^{L-1} \mathcal{M}_{s_j i} = 0\}$, $\mathbf{z} = \Pr(\mathbf{s})$.
	For $j = 1, \ldots, |\mathbf{z}|$; for $(r, m) = 1, \ldots, L; \; r \neq m$
	$\quad \mathcal{M}'_{z_j r} = 1, \; \mathcal{M}'_{z_j m} = 1$,
	$\quad$ If $\text{rk}(\boldsymbol{\mathcal{M}}') = K'$, $\boldsymbol{\mathcal{M}} = \boldsymbol{\mathcal{M}}'$, $\xi_0 = 0$ break;
	$\quad$ Else $\boldsymbol{\mathcal{M}}' = \boldsymbol{\mathcal{M}}$.
	return to **Main**.
Loop-2B	$\mathbf{s} = \{s_j \in \{0, \ldots, L-1\} \; : \; \sum_{i=0}^{L-1} \mathcal{M}_{is_j} = 0\}$, $\mathbf{z} = \Pr(\mathbf{s})$.
	For $j = 0, \ldots, |\mathbf{z} - 1|$; for $(r, m) = 0, \ldots, L-1; \; r \neq m$
	$\quad \mathcal{M}'_{rz_j} = 1, \; \mathcal{M}'_{mz_j} = 1$,
	$\quad$ If $\text{rk}(\boldsymbol{\mathcal{M}}') = K'$, $\boldsymbol{\mathcal{M}} = \boldsymbol{\mathcal{M}}'$, $\xi_1 = 0$ break;
	$\quad$ Else $\boldsymbol{\mathcal{M}}' = \boldsymbol{\mathcal{M}}$.
	return to **Main**.
Loop-2C	For $0, \ldots, L-1$; $x, y = \text{UniformDiscrete}(0, L-1)$
	$\quad \mathcal{M}'_{xy} = 1$,
	$\quad$ If $\text{rk}(\boldsymbol{\mathcal{M}}') = K'$, $\boldsymbol{\mathcal{M}} = \boldsymbol{\mathcal{M}}'$, $\xi_2 = 0$, break;
	$\quad$ Else $\boldsymbol{\mathcal{M}}' = \boldsymbol{\mathcal{M}}$.
	return to **Main**.
Main	While, $\mathcal{S}_1 < M \vee \mathcal{S}_2 > 0 \vee \|\mathbf{n}\|_0 < V \vee f > f_\Delta \vee \text{rk}(\boldsymbol{\mathcal{W}}^T\boldsymbol{\mathcal{W}}) \neq K'$
	$\quad \boldsymbol{\xi} = \mathbf{u}_3$, **Loop-2A**, **Loop-2B**, **Loop-2C**;
	$\quad$ Update $\mathbf{n}_{ik}, \mathbf{n}$, $f = |\mu_* - \frac{1}{V\mathcal{U}}\mathbf{u}_V^T\mathbf{n}|$,
	$\quad \mathcal{W}_{km} = \mathcal{M}_{k\alpha_m} \; k = 0, \ldots, L-1, \; m = 0, \ldots, K'-1$.
	$\quad$ If $\| \boldsymbol{\xi} \|_0 = 3$ then **Loop-1**.
Output	Optimal $\boldsymbol{\mathcal{M}}^* = \left[\mathbf{t}_0^* \ldots, \mathbf{t}_{L-1}^*\right]$, $\boldsymbol{\mathcal{W}}^* = \left[\mathbf{t}_{\alpha_0}^*, \ldots, \mathbf{t}_{\alpha_{K'-1}}^*\right]$.
	$\boldsymbol{\mathcal{C}} = (\boldsymbol{\mathcal{W}}^{*T}\boldsymbol{\mathcal{W}}^*)^{-1}\boldsymbol{\mathcal{W}}^*\boldsymbol{\mathcal{M}}^*$.

Given the vector $\boldsymbol{\lambda}$, the respective set of weights $\{\mathbf{w}_j\}_{j=0}^{L-1}$, the desired number of shots K', the desired number of optimal measurements $\mathcal{U}$, the optimal compressive ratio μ_*, the optimization of the

pseudorandom component of the coded apertures $\mathbf{r}_0, \ldots, \mathbf{r}_{L-1}$ can be written as

$$\min_{\{\mathbf{r}_0,\ldots,\mathbf{r}_{L-1}\}} |\mu_* - \frac{1}{V\mathcal{U}}\mathbf{u}_V^T\mathbf{n}| \tag{3.50}$$

Subject to

$$\operatorname{rank}([\mathbf{w}_0 \circ \mathbf{r}_0 \ \ldots \ \mathbf{w}_{L-1} \circ \mathbf{r}_{L-1}]) = K',$$

$$\|\sum_{j=0}^{\mathcal{U}-1} \mathbf{n}_{jk}\|_0 \geq M, \ \|\mathbf{n}\|_0 = V$$

$$\sum_{k \neq \ell}\sum\sum_{j} \mathbf{n}_{jk}^T\mathbf{n}_{j\ell} = 0 \ \ k,\ell = 0,\ldots,\mathcal{L}-1$$

where the vectors $\mathbf{n}_{jk}$ representing shifted versions of the coded apertures are given in (3.44), and $\mathbf{n} = \sum_{j=0}^{\mathcal{U}-1}\sum_{\ell=0}^{\mathcal{L}-1}\mathbf{n}_{j\ell}$ represents the mean number of spectral bands sensed at the jth location at the detector. A good range of μ_* has been empirically obtained as $[1.4, 2.0]$. In addition to the constraints in (3.50), the vectors $\mathbf{r}_0, \ldots, \mathbf{r}_{L-1}$ are realizations of a random variable perturbed such that they satisfy the constraints in (3.50). Figure 3.5 shows a flowchart of the optimization of the coded apertures. Solving equation (3.50) is an NP hard optimization problem. A stochastic based algorithm is proposed to solve (3.50) [?].

The objective of the algorithm in Table 3.3 is to find the matrix $\boldsymbol{\mathcal{M}}^* = [\mathbf{t}_0^* \ldots, \mathbf{t}_{K'-1}^*]$ which satisfies $\operatorname{rank}(\boldsymbol{\mathcal{M}}^*) = K'$, and the constraints given in (3.50). Further, the optimal matrix $\boldsymbol{\mathcal{M}}^*$ can be factorized as a function of its K' linear independent columns $\boldsymbol{\mathcal{W}}^* = [\mathbf{t}_{\alpha_0}^*, \ldots, \mathbf{t}_{\alpha_{K'-1}}^*]$ as $\boldsymbol{\mathcal{M}}^* = \boldsymbol{\mathcal{W}}^*\boldsymbol{\mathcal{C}}$ where $\boldsymbol{\mathcal{C}} = (\boldsymbol{\mathcal{W}}^{*T}\boldsymbol{\mathcal{W}}^*)^{-1}\boldsymbol{\mathcal{W}}^{*T}\boldsymbol{\mathcal{M}}^*$. The matrix $\boldsymbol{\mathcal{W}}^*$ contains an optimal row of coded apertures for spectral selectivity.

The algorithm uses the $L \times L$ matrix $\mathbf{B}$ whose elements are random realizations of a Bernoulli variable, further, K' rows of $\mathbf{B}$ have at least a nonzero element or the same $\operatorname{rank}(\mathbf{B}) \leq K'$. The **Loop-1** uses several realizations of the matrix $\mathbf{B}$ to initialize the matrix $\boldsymbol{\mathcal{M}}$. The initial matrix $\boldsymbol{\mathcal{M}}$ has both $\operatorname{rank}(\boldsymbol{\mathcal{M}}) = K'$ and a very low Frobenius norm. In each iteration, the **Main** loop verifies that the constraints given in (3.50) are satisfied. Then, the **Main** loop applies the loops **Loop-2A**, **Loop-2B**, and **Loop-2C** to increase the Frobenius norm of the initial matrix $\boldsymbol{\mathcal{M}}$. The loop **Loop-2A** increases the Frobenius norm of $\boldsymbol{\mathcal{M}}$ by making two randomly chosen elements in a column of $\boldsymbol{\mathcal{M}}$ equal to one. The loop **Loop-2B** increases the Frobenius norm of $\boldsymbol{\mathcal{M}}$ by making two randomly chosen elements in a row of $\boldsymbol{\mathcal{M}}$ equal to one. The loop **Loop-2C** increases the Frobenius norm by placing a one element in an arbitrary coordinate of $\boldsymbol{\mathcal{M}}$. The loops **Loop-2A**, **Loop-2B**, and **Loop-2C** do not change the rank of $\boldsymbol{\mathcal{M}}$. Further, the **Main** loop verifies that $\operatorname{rank}(\boldsymbol{\mathcal{W}}^T\boldsymbol{\mathcal{W}}) = K'$. The Frobenius norm of $\boldsymbol{\mathcal{M}}$ is increased until that f is less than some user defined constant f_Δ. If the loops **Loop-2A**, **Loop-2B**, and **Loop-2C** fail simultaneously to increase the Frobenius norm of $\boldsymbol{\mathcal{M}}$, then the algorithm restarts at **Loop-1**. Notice that the algorithm in Table 3.3 needs to be run N times to construct the complete 2-dimensional (2D) coded apertures. A flowchart of the procedure to reconstruct the desired set of bands is shown in Fig. 3.6. The details of the construction of the 2D coded apertures are explained in the next section.
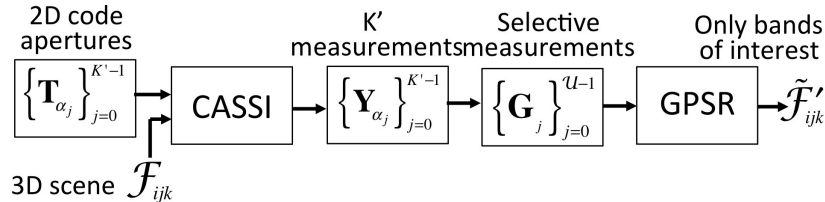
Figure 3.6: Given K' 2D optimized coded apertures, K' CASSI measurements $\mathbf{Y}_{\alpha_j}$ are made. These measurements are reordering to construct the spectrally selective measurements $\mathbf{G}_j$. The GPSR algorithm reconstructs only the desired bands. N unidimensional optimal codes $\{\mathbf{r}_{\alpha_j}\mathbf{w}_{\alpha_j}\}_{j=0}^{K'-1}$ are used to construct the 2D codes $\{\mathbf{T}_{\alpha_j}\}_{j=0}^{K'-1}$.

Table 3.4: Comparison Between CASSI and Optimized CASSI

	CASSI	Optimized CASSI
Number of Shots	K	$K' \leq K$
Data Cube Size	$N \times M \times L$	$N \times M \times \mathcal{L}$
Coded Aperture for each mth shot	Constant, T^m	Variable in each ith band T^{mi}
Output, $G_{nk} =$	$\displaystyle\sum_{i=0}^{L-1} \mathcal{F}_{i,n,k+i} T_{n,k+i}$	$\displaystyle\sum_{i=0}^{\mathcal{L}-1} \mathcal{F}'_{i,n,k+i} T^i_{n,k+i}$
Measurements Size	$N \times (M+L-1) \times K$	$N \times (M+\mathcal{L}-1)\mathcal{U}$

3.4 Optimal 2-Dimensional Coded Apertures

Section III provided the coded aperture design for a single slice at the detector. Here, we extend these concepts to the design of 2D coded apertures which are built by an ensemble of 1D coded apertures. The nth execution of the algorithm in Table 3.3 provides the optimal vectors $\mathbf{t}_{\alpha_1}^{(n)}, \mathbf{t}_{\alpha_2}^{(n)}, \ldots, \mathbf{t}_{\alpha_{K'}}^{(n)}$. The $N \times K'$ set of vectors $\{\mathbf{t}_{\alpha_k}^{(n)}\}$ are used to create the K' set of 2D coded apertures $\mathbf{T}_{\alpha_k}$ which can be calculated by

$$(\mathbf{T}_{\alpha_k})_{nj} = \left(\mathbf{t}_{\alpha_k}^{(n)}\right)_{\text{mod}_L(j)} \tag{3.51}$$

for $n = 0, \ldots, N-1$, $j = 0, \ldots, V-1$, and $k = 0, \ldots, K'-1$. Let $\mathbf{G}_{\alpha_k}$ be the 2D CASSI output when the respective coded aperture $\mathbf{T}_{\alpha_k}$ in (3.51) is used. Then, $\mathbf{Y}_{\alpha_k}$ is the 2D version of $\mathbf{y}_{\alpha_k}$ in (3.34). Similarly, the matrices $\mathbf{Y}_k$ representing the 2D version of $\mathbf{y}_k$ in (3.34) can be estimated as

$$\mathbf{Y}_k = \sum_{m=0}^{K'-1} \mathbf{B}_{mk} \mathbf{Y}_{\alpha_m} \qquad k = 0, \ldots, K-1 \tag{3.52}$$

where $\mathbf{B}_{mk} = \text{diag}\left(\mathcal{C}_{mk}^{(0)}, \ldots, \mathcal{C}_{mk}^{(N-1)}\right)$, and the matrices $\mathcal{C}^{(n)}$ are provided by the optimization algorithm.

Let the matrices $\mathbf{Y}_k$ in (3.52) be expressed in terms of their columns as $\mathbf{Y}_k = \left[\mathbf{y}_0^k \ldots \mathbf{y}_{V-1}^k\right]$, then the 2D version $\mathbf{G}_0$ of the desired compressive measurement $\mathbf{g}_0$ in (3.36) containing only the bands of interest is given by

$$\mathbf{G}_0 = \left[\mathbf{y}_0^0, \ldots, \mathbf{y}_{L-1}^{L-1}, \mathbf{y}_L^0, \ldots, \mathbf{y}_{V-1}^{\text{mod}_L(V-1)}\right]. \tag{3.53}$$

The remaining optimized matrices $\mathbf{G}_1, \ldots, \mathbf{G}_{\mathcal{U}-1}$ are estimated using (3.38) and selecting the elements of the matrices $\mathbf{Y}_k$ in (3.52) containing exclusively the desired bands. Observe that the spectrally selective measurement matrices $\mathbf{G}_m$ in (3.53) can be seen as the output of a multi-frame CASSI system sensing an $N \times M \times \mathcal{L}$ spectral data cube given by

$$\mathcal{F}'_{ijk} = \mathcal{F}_{\epsilon_i jk} \qquad i = 0, \ldots, \mathcal{L} \tag{3.54}$$

where ϵ_i indexes the desired bands. Further, the matrices $\mathbf{G}_m$ can be seen as the output of the system whose input-output relation is given by

$$(\mathbf{G}_m)_{jk} = \sum_{i=0}^{\mathcal{L}-1} \mathcal{F}'_{i,j,k+i} T^{mi}_{j,k+i} + \omega_{j,k} \tag{3.55}$$

where $\mathbf{T}^{mi} = \left[\tilde{\mathbf{t}}_m^{\epsilon_i}(0) \ \tilde{\mathbf{t}}_m^{\epsilon_i}(1) \ \ldots \ \tilde{\mathbf{t}}_m^{\epsilon_i}(N-1)\right]^T$ and $\tilde{\mathbf{t}}_m^{\epsilon_i}(n)$ is the nth realization of the vector $\tilde{\mathbf{t}}_m^{\epsilon_i}$ defined in (3.43). Table (3.4) summarizes the principal differences between a CASSI system using multiple shots and the CASSI system with optimized coded apertures defined in (3.55).

3.5 Simulations

To test the methodology developed in Sections 3.3, and 3.4, a set of optimal aperture codes for two different desired spectral band sets $\boldsymbol{\lambda}$ are derived, for an increasing number of measurement shots. The
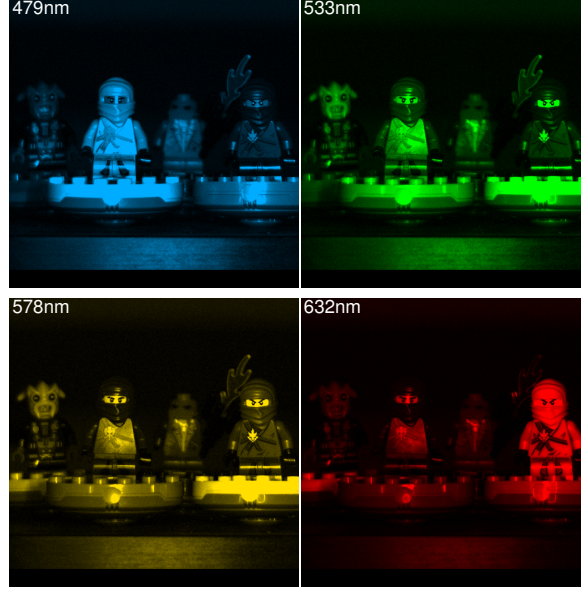
Figure 3.7: 4 spectral channels of 24 channels in the data cube used in the simulations are presented. The complete data cube extends from 460nm to 680nm, and it has 24 spectral channels and 512×512 pixels of spatial resolution.

experiments use a test data cube $\mathcal{F}$ with 512×512 pixels of spatial resolution and $L = 24$ spectral bands ranging from 460nm to 668nm.[2] Figure 3.7 shows a portion of the data cube used in the simulations. The compressive sensing reconstruction is realized using the GPSR algorithm [?]. Sparsity basis selection for hyperspectral signals has been widely studied in [?]. It is shown there that the Kronecker product of 1D sparsity basis provides the highest compression ratio for hypersectral images. Here, the base representation Ψ_{3D} is the Kronecker product of three basis $\Psi = \Psi_1 \otimes \Psi_2 \otimes \Psi_3$, where the combination $\Psi_1 \otimes \Psi_2$ is the 2D-Wavelet Symmlet 8 basis and Ψ_3 is the Cosine basis. Other Kronecker products such as tridimensional wavelets can also be used, however, they requires that the underlying signal has dyadic dimensions. The basis based on the Cosine Transform has the advantage of its low computational cost compared with the tridimensional wavelet. Using the Kronecker representation the data cube in Fig. 3.7 can be represented with only 4% of the coefficients and preserving the 99.67% of the energy of the signal. The maximum number of iterations in the GPSR algorithm is 50 and the stopping criterion as recommended in [?] is the objective function.

3.5.1   Rank Minimization Algorithm

In the first experiment, the rank minimization algorithm is run for $L = 24$, $\boldsymbol{\lambda} = [461\text{nm} - 471\text{nm}, 641\text{nm} - 668\text{nm}]$, $\mathcal{U} = 3$, $K' = 12$, $\mu_* = 1.6$. The minimization algorithm aims at reducing the rank of the matrix $\mathbf{M}_t$ from 24 to 12. Figure 3.8(b) shows the error $f = |\mu_* - \frac{1}{V\mathcal{U}}\mathbf{u}_V^T\mathbf{n}|$ of the minimization algorithm through the iterations. There, it can be observed that the algorithm periodically aims at minimizing the cost function, however, the algorithm restarts when the constraints in (3.50) are not satisfied. This behavior of the algorithm is originated in the pseudorandom searching strategy.

In the second experiment, the optimization algorithm is run for several values of the parameter μ_*, the other parameters are kept equal to the first experiment. For each μ_* value the optimization algorithm is run 512 times. Using the spectral data cube in Fig. 3.7 and the 512 realizations of the optimization algorithm, the 2D spectrally selective measurements $\{\mathbf{G}_0, \mathbf{G}_1, \mathbf{G}_2\}$ are constructed using the procedure in Section 3.4. Using the spectrally selective measurements and the GPSR algorithm, the desired bands are reconstructed and their mean PSNR is calculated. This experiment is repeated 50 times and the PSNR is averaged. Figure 3.8(a) shows the averaged PSNR as a function of the parameter μ_*. From

---

[2]Data provided by Yuehao Wu and Iftekhar O. Mirza. Test objects provided by Andrew Arce.
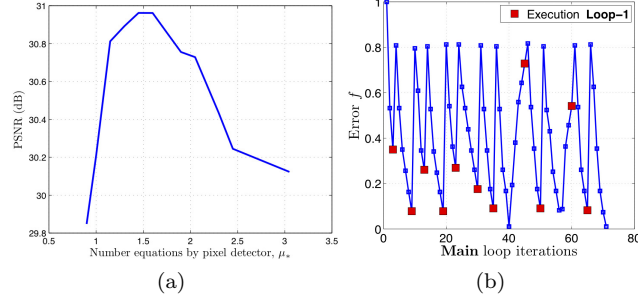
Figure 3.8: (a) Performance of the rank minimization algorithm versus the μ_* parameter, (b) a typical performance profile through iterations of the rank minimization algorithm. The iterations where the algorithm restarting are indicated with squares.

several simulations, it was found that regardless the value of L or $\mathcal{L}$ the optimal value of the parameter μ_* can be chosen as rule of thumb between 1.4 to 2.0. In practice, the lower the value of μ_*, the more difficult it will be to achieve convergence of the optimization algorithm.

3.5.2 Spectral Selectivity

In the first experiment of spectral selectivity, the set of desired bands are set to $\boldsymbol{\lambda}_1 = [461\text{nm} - 479\text{nm},$ $641\text{nm} - 668\text{nm}]$ as it is depicted in Fig. 3.9(g). Figure 3.7 depicts a portion of the $24 \times 512 \times 512$ data cube used in the simulations. In this experiment, the initial rank of the matrix $\mathbf{M}_t$ is 24. Using the optimization algorithm, the rank of the matrix $\mathbf{M}_t$ is minimized to 9, 12, and 18. The optimization uses $\mathcal{U} = 3$ and $\mu_* = 1.6$. The experiment is repeated 45 times and the mean PSNR is estimated. The resulting spectral data cubes are shown as they would be viewed by a Stingray F-033C CCD Color Camera. Figure 3.9(a) shows the desired original bands. Figure 3.9(b) illustrates the results when the desired spectral bands are reconstructed using 12 Bernoulli non-optimized random coded apertures measurements. In this case, the 24 bands are reconstructed and the desired bands are manually selected. Figures 3.9(c)-(e) show the results when 9, 12 and 18 optimized coded apertures are respectively used in the sensing and reconstruction process. Notice that in this case only the desired bands are reconstructed. Figure 3.9(f) shows a typical realization of the optimal coded aperture mentioned in (3.55). Figures 3.9(g), 3.9(h), and 3.9(i) show a zooming of the Figs. 3.9(a), 3.9(b), and 3.9(d) respectively. Clearly Fig. 3.9 depicts that the optimal coded apertures conduce to a higher quality reconstruction. Additionally, Figure 3.10 depicts the differences between the original and the reconstructed 3rd spectra channel ($479nm$). Reconstructions artifacts in Figure 3.10 emerge in part from the cosine sparsifier in the spectral axis and in part from the 2D wavelet spatial sparcifier.

Table 3.5: **Mean reconstruction PSNR in dB.**

Number of shots	9		12		18	
	λ_1	λ_2	λ_1	λ_2	λ_1	λ_2
Bernoulli, min	25.02	26.25	26.08	27.13	27.32	28.12
mean	26.68	27.47	26.92	27.77	27.51	28.30
max	27.19	27.89	27.38	28.14	27.58	28.38
Hadamard, min	23.51	25.09	24.66	26.03	25.71	26.98
mean	25.50	26.53	26.15	27.13	26.99	27.85
max	26.68	27.37	27.04	27.83	27.38	28.19
Optimized, min	30.79	29.85	29.44	30.34	31.75	30.92
mean	**30.91**	**30.09**	**31.02**	**30.81**	**31.79**	**31.21**
max	31.01	30.27	31.13	30.96	31.84	31.32

In the second experiment, 9 desired bands are selected in the range given by $\boldsymbol{\lambda}_2 = [488\text{nm} - 515\text{nm},$ $560\text{nm} - 596\text{nm}]$. In this case, the initial rank of the matrix $\mathbf{M}_t$ is 21. The optimization uses the same values of $\mathcal{U}$ and μ_* used in the first experiment. Again, the experiment is repeated 45 times and the PSNR are averaged. Figure 3.11(a) shows the desired original bands. Figure 3.11(b) illustrates the results for 12 Bernoulli non-optimized random coded apertures. Figure 3.11(c) shows the results when 12 optimized
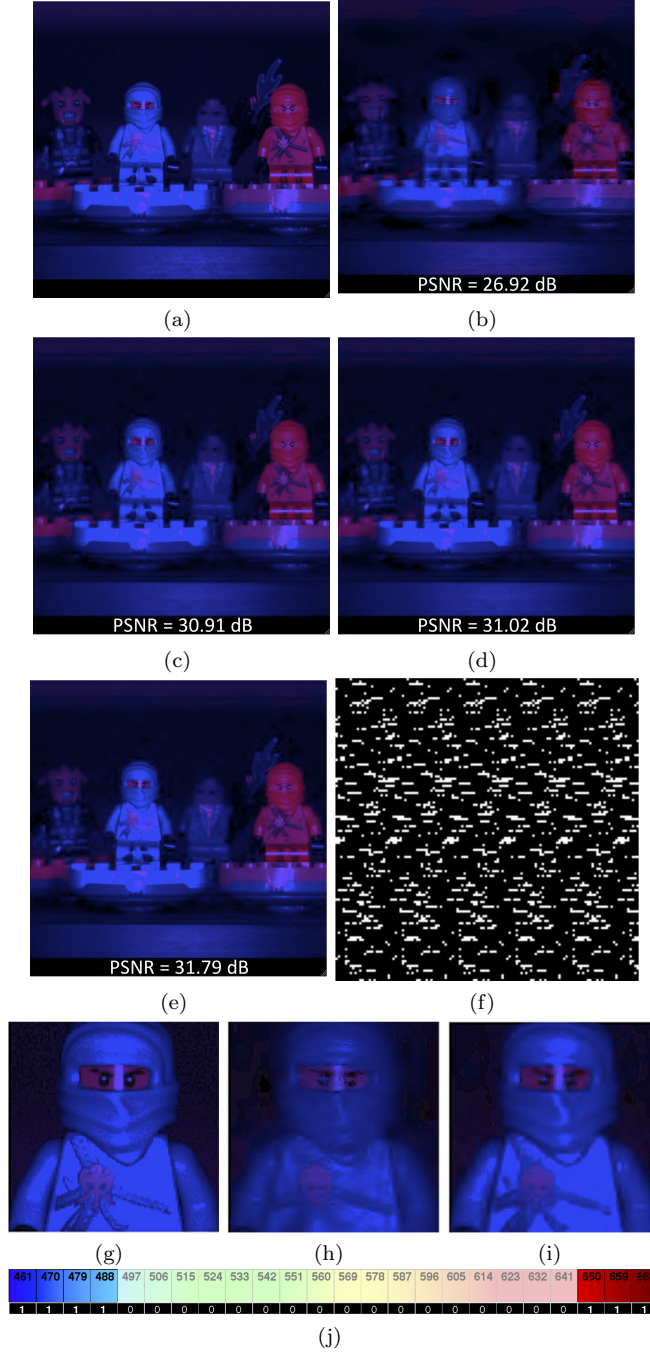
Figure 3.9: The resulting spectral data cubes are shown as they would be viewed by a Stingray F-033C CCD Color Camera. The desired bands are depicted in (g). The original desired bands are shown in (a). Reconstructed images by using : (b) 12 shots with random codes, (c) 9, (d) 12, and (e) 18 shots with optimized codes. An optimized coded aperture used to reconstruct (c) is shown in (f). Zooming of (a) (original), (b) (random codes), and (d) (optimal codes) are shown in (g), (h), and (i) respectively.

coded apertures are used in the sensing and reconstruction process. Figure 3.11(d) illustrates a typical realization of the optimal codes. The simulations using random coded apertures were repeated using Hadamard matrices, however the PSNR was similar to that of the Bernoulli case. Table 3.5 summarizes the numerical results shown in Figs. 3.9 and 3.11. To indicate the consistency of the algorithm Table 3.5 shows the minimum, mean and maximum averaged PSNR of the 45 repetitions of the experiment. The optimized results indicate improvements up to 4dB in the PSNR of the reconstructed data cubes
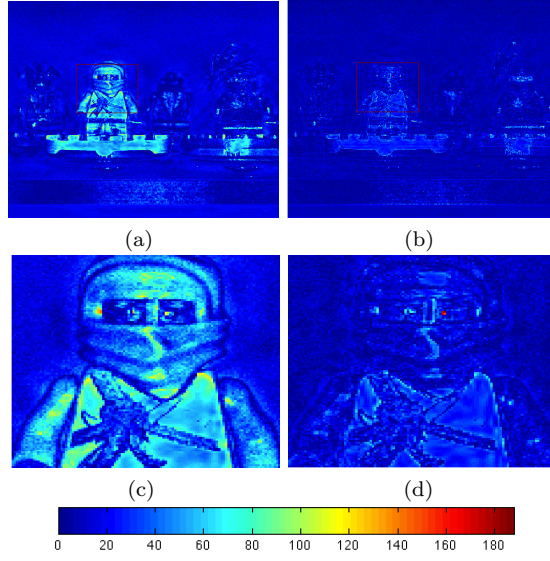
Figure 3.10: Differences between the original and the reconstructed 3rd spectra channel ($479nm$) are presented for (a) the reconstructed data cube in Fig. 3.9(b) (random codes) and (b) the reconstructed data cube in Fig. 3.9(d) (optimized codes). A zoomed region of (a) and (b) are presented in (c) and (d) respectively.

compared with the results of using random coded apertures.
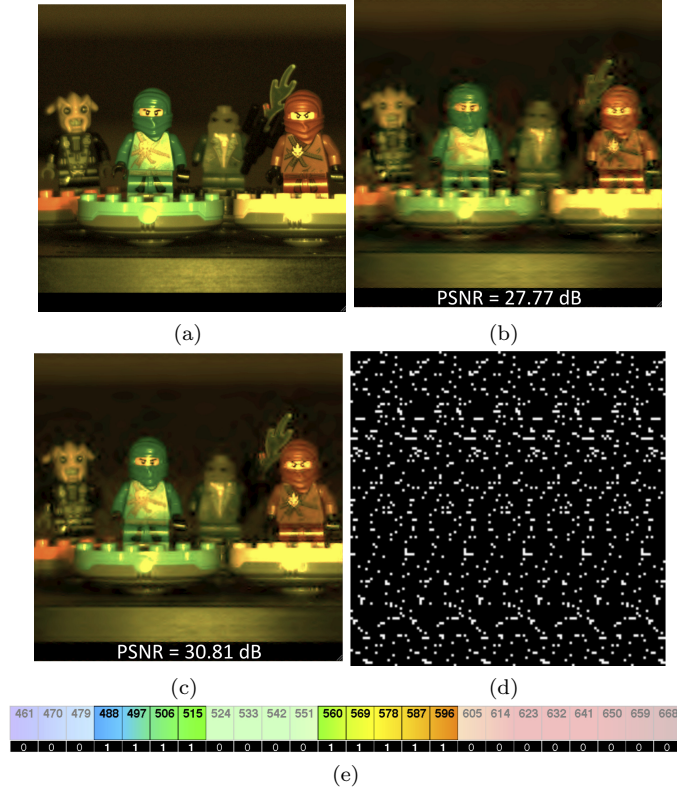
Figure 3.11: The resulting spectral data cubes are shown as they would be viewed by a Stingray F-033C CCD Color Camera. The desired bands are indicated in (e). The original desired bands are shown in (a). Reconstructed images by using : (b) 12 shots with random codes, and (c) 12 shots with optimized codes. An optimal coded aperture is illustrated in (d).

3.6   Conclusion

A matrix representation of CASSI has been developed. The matrix model permits the optimal design of weight coded apertures that can be used to build a set the spectrally selective compressive CASSI measurements. A rank minimization algorithm was designed to estimate the pseudorandom component of the coded apertures. The optimization of the coded apertures is subject to a specified number of shots and the optimal coded apertures are designed to satisfy the RIP condition with high probability. Given a set the desired bands, the PSNR achieved by the optimized codes is up to 4dB higher than the systems using random codes.

Chapter 4

Higher-Order Computational Model for Coded Aperture Spectral Imaging

4.1   Introduction

Typically, the discretized output at the CASSI detector g_{mn} is modeled as the sum of the underlying spectral voxel slices which have been previously modulated by a coded aperture and subsequently spatially dispersed by a prism. More specifically, the two dimensional CASSI output has been traditionally modeled as

$$g_{mn} = \sum_{k=0}^{L-1} f_{(m-k)jk} T_{(m-k)j},\qquad(4.1)$$

where f_{ijk} is the discretization of the underlying spatio-spectral power source density and T_{ij} is the discretized coded aperture. Notice that f_{ijk} in (4.1) is assumed to be a cubic voxel which impinges on a single pixel detector element g_{mn}. The analog sensing phenomena, however, is such that when a single voxel of a scene is dispersed by the prism, it impinges on several detector elements at a time. This, in turn, causes blurring which deteriorates the quality of image reconstruction. To ameliorate this problem, instead of using the coded aperture T_{ij}, a set of calibrated coded apertures $\{T_{ij}^k\}_{k=0}^{L-1}$ are experimentally measured and used in the reconstruction process to take into account the non-ideal optical blur and non-linear dispersion [**?**]. Thus, the model in (4.1) suffers of a coarse approximation which is then partially rectified by the coded aperture calibration process.

There are two drawbacks in this approach. First the calibration process is often inadequate such that the discretized voxels f_{ijk} are incorrectly weighted by the calibrated codes T_{ij}^k. The calibration errors originate principally from the assumption that a coded cubic voxel impinges on the detector when actually it is a coded oblique voxel which impinges on it. Secondly, calibration of the coded apertures is difficult for multiframe CASSI systems where a sequence of coded apertures are used sequentially. This Chapter examines the sensing phenomena and determines a more precise computational model than that in (4.1). The gains include less reliance of calibration procedures in the reconstruction, as well as higher quality of image reconstruction. The higher-order model is tested through extensive simulations and experimentally in a CASSI multi-frame testbed.

4.2   System Model

The CASSI optical architecture proposed in [**?**] is depicted in Fig. 4.1. Denote the spatio-spectral power source density as $f_0(x, y, \lambda)$ where x and y index the spatial coordinates and λ indexes the wavelength. The spatio-spectral image source density $f_0(x, y, \lambda)$ is firstly coded by a coded aperture $T(x, y)$. The resulting coded field $f_1(x, y, \lambda)$ is subsequently dispersed by a dispersive element before it impinges onto

the FPA detector. The compressive measurements across the FPA are realized by the integration of the field $f_2(x,y,\lambda)$ over the detector's spectral range sensitivity. The spectral density at the output of the dispersive element, can be expressed as,

$$f_2(x,y,\lambda) = \int\int T(x',y')f_0(x',y',\lambda)\delta(x' - (x - S(\lambda)))\delta(y' - y)dx'dy', \tag{4.2}$$

where $\delta(x' - (x - S(\lambda)))\delta(y' - y)$ represents the optical impulse response of the system, such that $S(\lambda) = \alpha(\lambda)(\lambda - \lambda_c)$ is the dispersion induced by the prism along the x-axis, which is centered at the wavelength λ_c and has a dispersion coefficient $\alpha(\lambda)$. The resulting intensity image at the FPA is the integration of the field $f_2(x,y,\lambda)$ over the detector's spectral range sensitivity (Λ) that can be represented as $g(x,y) = \int_\Lambda f_2(x,y,\lambda)d\lambda$. Assuming ideal optical elements, the energy in front of the 2D FPA can be expressed as,

$$g(x,y) = \int_\Lambda T(x - S(\lambda),y)f_0(x - S(\lambda),y,\lambda)d\lambda. \tag{4.3}$$

Using a first order discretization model [?, ?, ?], a CASSI measurement at the $(m,n)^{th}$ pixel is given by, $g_{mn} = \int\int p(m,n;x,y)g(x,y)dxdy + w_{mn}$, where w_{mn} represents additive noise and $p(m,n;x,y) = \text{rect}\left(\frac{x}{\Delta} - m, \frac{y}{\Delta} - n\right)$ accounts for the detector pixelation, with Δ being the detector pixel pitch. This approximation however is coarse leading to inter-pixel blurring in the detection. The goal of this Chapter is thus to develop a more precise, higher order computational model that mitigates the inter-voxel interference, which in turn leads to higher quality spectral imaging. At the same time, the higher-order precision model allows less reliance on calibration corrections. To this end, the pixelation function $p(m,n;x,y)$ is replaced by defining the integration limits at the detector as,

$$g_{mn} = \int_{n\Delta}^{(n+1)\Delta}\int_{m\Delta}^{(m+1)\Delta}\int_\Lambda T(x - S(\lambda),y)f_0(x - S(\lambda),y,\lambda)d\lambda dxdy, \tag{4.4}$$

and the new discretization model is then derived as follows. The source $f_0(x,y,\lambda)$ is discretized as the signal f_{ijk} where i, j, and k are the discrete indices accounting for x, y, and λ respectively. A voxel f_{ijk} represents the intensity concentrated in a specific spatio-spectral region Ω_{ijk} where $x \in [i\Delta, (i+1)\Delta]$, $y \in [j\Delta, (j+1)\Delta]$, and $\lambda \in [\lambda_k, \lambda_{k+1}]$. Specifically, the $(ijk)^{th}$ voxel is given by

$$f_{ijk} = \int_{\lambda_k}^{\lambda_{k+1}}\int_{j\Delta}^{(j+1)\Delta}\int_{i\Delta}^{(i+1)\Delta} f_0(x,y,\lambda)dxdyd\lambda \tag{4.5}$$

$$= \iiint_{\Omega_{ijk}} f_0(x,y,\lambda)dxdyd\lambda = c_{ijk}\cdot f_0(x_i,y_j,\lambda_k),$$

where c_{ijk} represents the quadrature weight, and x_i, y_j, and λ_k are average values in Ω_{ijk}. Notice in (4.5) that the spectral axis λ has been discretized in L spectral bands. The range of the kth spectral band is $[\lambda_k \ \lambda_{k+1}]$ where λ_k is the solution to the equation given by

$$S(\lambda_k) - S(\lambda_0) = k\Delta, \quad k = 0,\ldots,L-1, \tag{4.6}$$

where again $S(\lambda) = \alpha(\lambda)(\lambda - \lambda_c)$ is the dispersion of the prism. Equation (4.6) establishes that the spectral axis resolution is determined by the prism response $S(\lambda)$ and by the pitch of the detector Δ.
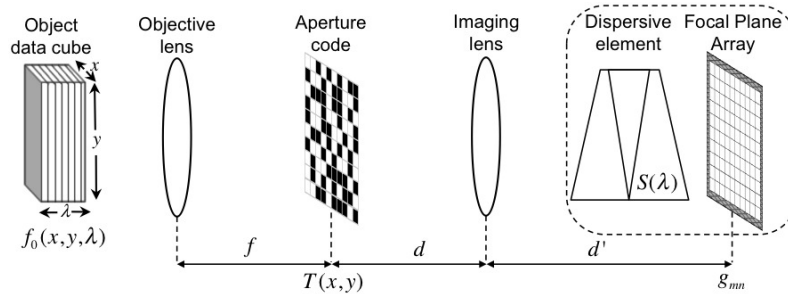
Figure 4.1: Optical elements present in CASSI.

Equation (4.5) also establishes the spatial resolution which is determined by the pitch of the detector Δ that is assumed to be equal to the coded aperture pitch. Using the ranges of the L spectral bands defined in (4.6), Eq. (4.4) can be expressed as

$$g_{mn} = \int\limits_{n\Delta}^{(n+1)\Delta} \int\limits_{m\Delta}^{(m+1)\Delta} \left[\sum_{k=0}^{L-1} \int\limits_{\lambda_k}^{\lambda_{k+1}} T(x - S(\lambda), y) f_0(x - S(\lambda), y, \lambda) d\lambda \right] dx dy.$$ (4.7)

To better illustrate the discretization of the source, Fig. 4.2 depicts the physical phenomena described in Eq. (4.7). Notice that each cubic voxel when sheared by the prism effects, turns into an oblique voxel. The oblique voxel is stretched along the x axis, such that when it is projected onto the detector grid, it impinges onto several detector pixel elements at once. Hence, several voxels at the source will impact each of the FPA pixels.
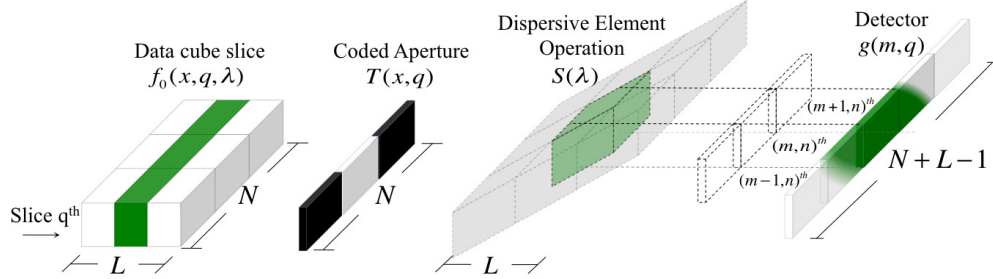
Figure 4.2: CASSI integration model. A voxel of the data cube is coded by the aperture code, sheared by the dispersive element with dispersion $S(\lambda_k)$ and projected onto several pixels of the detector.

The inter-voxel interference is next examined by two discretization models as illustrated in Fig. 4.3, when viewed from the top of the datacube. A linear dispersive function with slope equal to one ($d_S = 1$) is assumed in the figure. Figure 4.3(a) depicts the traditional discretization approach proposed in [?]. Figure 4.3(b) shows the higher precision discretization model where the FPA pixel detector captures energy from several voxels simultaneously. The dotted lines indicate the spatio-spectral region of the data cube integrated in the $(m, n)^{th}$ detector pixel. It can be observed that the higher precision discretization

(a) First order precision model (b) Higher order precision model
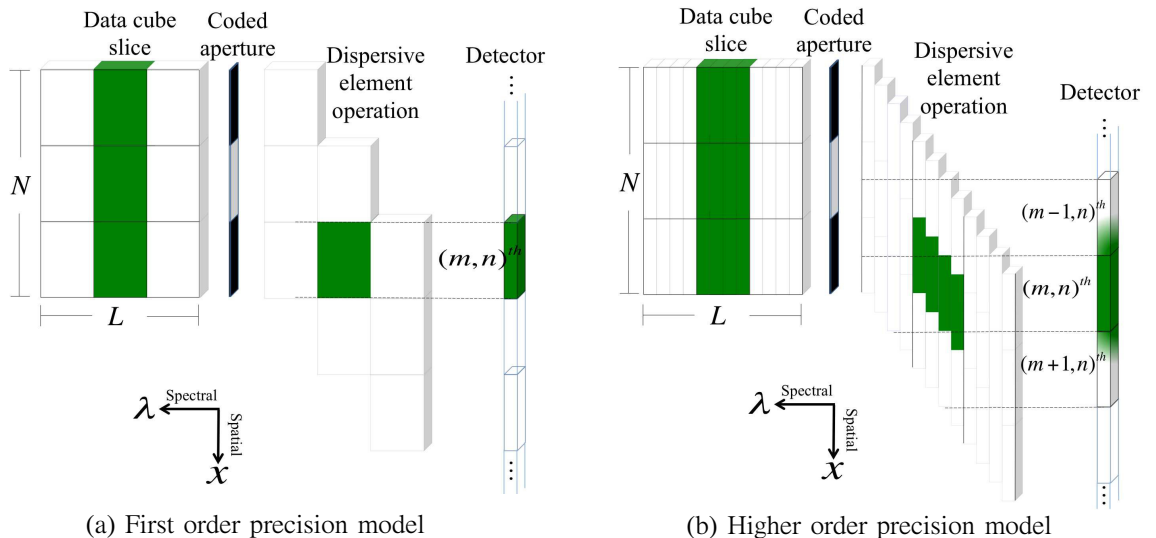
Figure 4.3: (Color online) (a) First order discretization model. A voxel impinges onto a single FPA pixel detector; (b) higher order discretization model. A voxel impinges onto three FPA pixels. Notice that the light dispersion path is on the (λ, x) axis (top view).

of the dispersive curve leads to more voxels superimposing in the formation of g_{mn}.

Figure 4.4 shows a zoomed version of one voxel of the source after it is sheared by the prism. Notice that its energy will impinge on up to three different FPA pixels when $d_S = 1$. Each voxel at the source can then be partitioned into three different regions denoted as R_0, R_1, and R_2. Depending on the nature of $S(\lambda)$, a voxel may affect more than 3 detector elements. Therefore, for a general dispersion curve, each of the integrals in (4.7) can be rewritten as

$$\iiint\limits_{n\Delta,m\Delta,\lambda_k}^{(n+1)\Delta,(m+1)\Delta,\lambda_{k+1}} T(x-S(\lambda),y)f_0(x-S(\lambda),y,\lambda)d\lambda dxdy = \sum_{u=0}^{d} \iiint\limits_{\lambda_k\,\{x-S(\lambda),y\}\in R_u}^{\lambda_{k+1}} T(x-S(\lambda),y)f_0(x-S(\lambda),y,\lambda)dxdyd\lambda, \qquad (4.8)$$

where $d = d_S + 1$ for linear dispersion, and $d = \max\lceil (m+1)\Delta - S(\lambda_k)\rceil$ when a prism exhibits a non-linear response. Further, let the discrete version of the aperture code $T(x,y)$ be $t_{i,j}$ and using the representation in Eq. (4.5) for $f_0(x,y,\lambda)$, then

$$\int\limits_{\lambda_k}^{\lambda_{k+1}} \iint\limits_{\{x-S(\lambda),y\}\in R_u} T(x-S(\lambda),y)f_0(x-S(\lambda),y,\lambda)dxdyd\lambda = w_{mnku}t_{(m-k-u)n}f_{(m-k-u)nk} \qquad (4.9)$$

where the proportion of the voxel $f_{(m-k-u)nk}$ contained in R_u is taken into account by the constant w_{mnku}. Notice that the subindex k in w_{mnku} refers to the spectral interval $[\lambda_k\ \lambda_{k+1}]$. While the weights w_{mnku} can be estimated using a calibration process, they can also be numerically approximated assuming that the the spectral information is uniformly distributed in the region delimited by Ω_{ijk}. More specifically, they are calculated as

$$w_{mnku} = \left(\iiint\limits_{R_u} dxdyd\lambda\right)\left(\iiint\limits_{\Omega_{(m-k-u)nk}} dxdyd\lambda\right)^{-1} \qquad (4.10)$$

where R_u is taken in the respective interval $[\lambda_k\ \lambda_{k+1}]$. In practice, the sections R_u can be calculated by estimating the prism response $S(\lambda)$ and the misalignment between the coded aperture and the FPA detector. Using Eq. (4.8) and (4.9), Eq. (4.7) can be expressed as

$$g_{mn} = \sum_{k=0}^{L-1}\sum_{u=0}^{d} w_{mnku}t_{(m-k-u)n}f_{(m-k-u)nk}. \qquad (4.11)$$

Equation (4.11) can be written in matrix form as $\mathbf{g} = \mathbf{Hf}$, where the $N(N+L+d-1)$ long vector $\mathbf{g}$ and the N^2L long vector $\mathbf{f}$ represent the compressive measurements and the spectral data cube respectively,
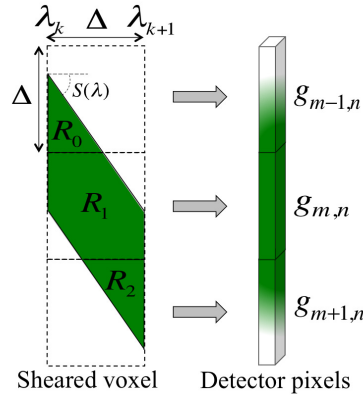
Figure 4.4: A voxel dispersed into the regions R_0, R_1, and R_2 in each interval $[\lambda_k\ \lambda_{k+1}]$. These regions determine the voxel fractions involved in the formation of the $g_{m-1,n}$, $g_{m,n}$ and $g_{m+1,n}$ detector pixels.

ordered lexicographically. When several FPA measurements are captured each one using a different aperture code, the ith FPA measurement can be written as

$$\mathbf{g}_i = \mathbf{H}_i \mathbf{f}. \tag{4.12}$$

In Eq. (4.12) each $N(N + L + d - 1) \times N^2 L$ matrix $\mathbf{H}_i$ is composed by,

$$\mathbf{H}_i = \mathbf{PT}_i, \tag{4.13}$$

where $\mathbf{P}$ accounts for the weights w_{mnku} and the dispersion of the prism, and $\mathbf{T}_i$ represents the ith coded aperture. Here $\mathbf{T}_i$ is a block-diagonal matrix of the form,

$$\mathbf{T}_i = \begin{bmatrix} \text{diag}(\mathbf{t}_i) & \mathbf{0}_{N^2} & \cdots & \mathbf{0}_{N^2} \\ \mathbf{0}_{N^2} & \text{diag}(\mathbf{t}_i) & \cdots & \mathbf{0}_{N^2} \\ \vdots & \vdots & \ddots & \vdots \\ \mathbf{0}_{N^2} & \mathbf{0}_{N^2} & \cdots & \text{diag}(\mathbf{t}_i) \end{bmatrix}, \tag{4.14}$$

where $\mathbf{t}_i$ is the ith aperture code in lexicographical notation and $\mathbf{0}_{N^2}$ is a $N^2 \times N^2$ zero-matrix. Notice that Eq. (4.10) can be written in matrix form as, $(\mathbf{W}_k^u)_{mn} = \omega_{mnku}$, for $m, n = 0, 1, \ldots, N - 1$, and k, u as in Eq. (4.11). Then, the matrix $\mathbf{P}$ is given by $\mathbf{P} = \sum_{u=0}^{d} \mathbf{P}_u$, such that

$$\mathbf{P}_u = \begin{bmatrix} & & \mathbf{0}_{Nu \times N^2 L} & \\ \text{diag}(\mathbf{W}_0^u) & \mathbf{0}_{N \times N^2} & \cdots & \mathbf{0}_{N \times N^2} \\ \mathbf{0}_{N \times N^2} & \text{diag}(\mathbf{W}_1^u) & \cdots & \mathbf{0}_{N \times N^2} \\ \vdots & \vdots & \ddots & \vdots \\ \mathbf{0}_{N \times N^2} & \mathbf{0}_{N \times N^2} & \cdots & \text{diag}(\mathbf{W}_{L-1}^u) \\ & & \mathbf{0}_{N(d-u) \times N^2 L} & \end{bmatrix}. \tag{4.15}$$

The ensemble of measurements $\{\mathbf{g}_i\}_{i=1}^{K}$, can be succinctly written as $\boldsymbol{g} = \tilde{\mathbf{H}} \mathbf{f} = \boldsymbol{\mathcal{P}} \boldsymbol{\mathcal{T}} \mathbf{f}$, where $\boldsymbol{g} = \left[\mathbf{g}_1^T, \ldots, \mathbf{g}_K^T \right]^T$, $\boldsymbol{\mathcal{P}}$ is a K-times block-diagonal matrix of $\mathbf{P}$, and $\boldsymbol{\mathcal{T}} = \left[\mathbf{T}_1^T, \ldots, \mathbf{T}_K^T \right]^T$, with K representing the number of FPA shots. Figure 4.5 depicts the structure of the matrix $\tilde{\mathbf{H}}$ for the first order and the higher order discretization models, when three FPA shots are used to capture a $6 \times 6 \times 5$ datacube.

4.3 Simulations

In order to compare the higher-order precision model with the traditionally used model, a hyper-spectral data cube was experimentally acquired using a wide-band Xenon lamp as the light source, and a visible monochromator. Monochromatic images were captured every 1nm in the spectral range $\{450 - 620\}$; thus 170 spectral planes were acquired. The image intensity was captured by a CCD camera AVT Marlin F033B, with 656×492 pixels, exhibiting a pixel pitch of $9.9\mu m$ and using 8 bits for pixel depth. In addition, a double Amici prism was used as the dispersive element. Its non-linear dispersion curve shown in Fig. 4.10(b) was determined experimentally by using the monochromator as the input of the setup. Other elements such as the lens, the spectral response of the camera, and the coded apertures are considered ideal. Deviations from the ideal characteristics of these elements are mitigated partially by a calibration step. In this architecture, a voxel spanning any of the following wavelength intervals will create a displacement of a pixel on the detector: $\{450 - 463\}$, $\{464 - 477\}$, $\{478 - 493\}$, $\{494 - 510\}$, $\{511 - 530\}$, $\{531 - 556\}$, $\{557 - 586\}$ and $\{587 - 620\}$ where all the intervals are given in nanometres. Thus, the 170 spectral planes of the datacube will be clustered into 8 bands. Notice that the intervals width are not constant, as a non-linear dispersive element was used. Figure 4.6 shows the eight spectral bands of the datacube, which the CASSI system aims at recovering.

Experiments use the multi frame CASSI setup described in [?], and simulation algorithms utilizes 64 bits as arithmetic precision. Aperture codes entries are random realizations of a Bernoulli random

(a) First order discretization model · (b) Higher order discretization model
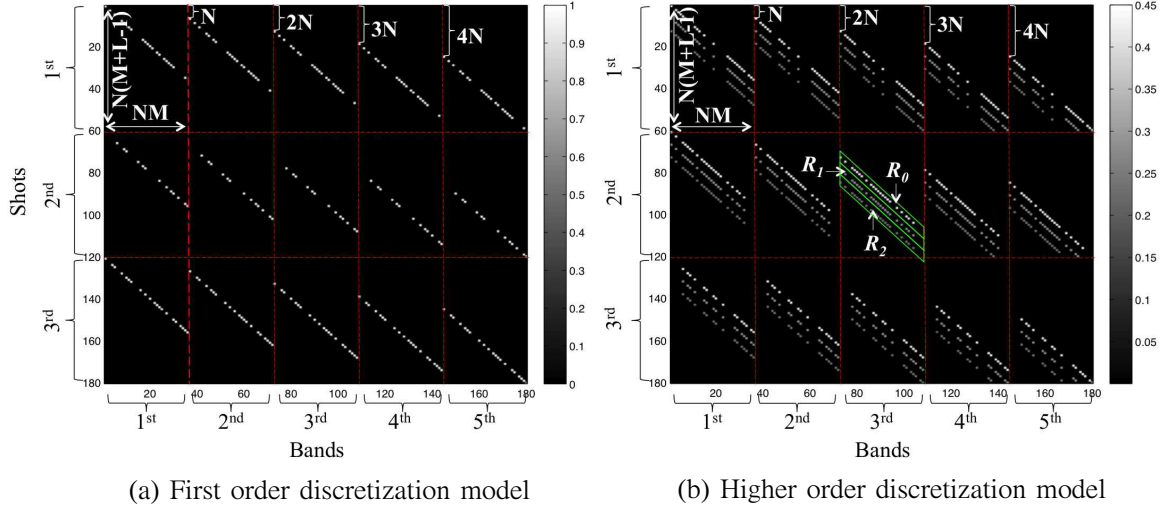
Figure 4.5: Structure of the matrix $\tilde{\mathbf{H}}$ for a $N = M = 6$, $L = 5$ datacube, when $K = 3$ for (a) CASSI traditional model ($\tilde{\mathbf{H}} \in \mathbb{R}^{180 \times 180}$); (b) Higher order CASSI model ($\tilde{\mathbf{H}} \in \mathbb{R}^{180 \times 180}$). Extra diagonal terms account for the inter-voxel interference. Notice that entries in (a) are either 0 or 1, while in (b) they vary in the interval $[0, 1]$.
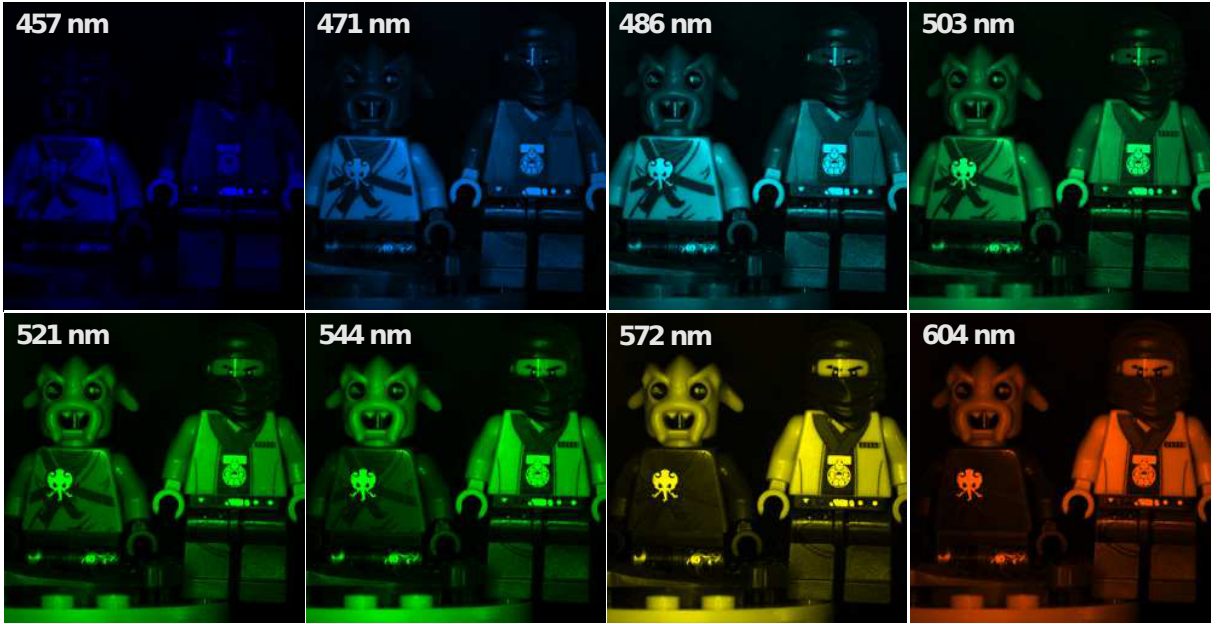
Figure 4.6: Spectral bands used in the simulations and their central wavelength.

variable with parameter $p = 0.5$. Note that the proposed model uses the same pitch for coded aperture features and FPA pixels. In summary, the hyper-spectral test data cube $\mathbf{F}$ has 256×256 pixels of spatial resolution and $L = 8$ spectral bands in the range 450 nm to 620 nm. In order to simulate the analogous sensing process, the compressive measurements are obtained using the 170 spectral planes of the datacube, as shown in Fig. 4.3(b). Notice also that the reconstruction process aims to recover the average of the spectral information in the 8 mentioned spectral intervals. The calibration weights for the proposed model are approximated using Eq. 4.10 and the prism's response curve. Given the set of compressive measurements, the voxels' weight distribution and the set of coded apertures, the hyper-spectral datacube is recovered using the GPSR algorithm [?]. GPSR exploits the sparse nature of the hyperspectral

datacube. In particular, the hyperspectral signal $\mathbf{F} \in \mathbb{R}^{N \times M \times L}$, or its vector representation $\mathbf{f} \in \mathbb{R}^{N.M.L}$, are assumed to be $K-$sparse on some basis $\boldsymbol{\Psi}_{3D}$, such that $\mathbf{f} = \boldsymbol{\Psi}_{3D}\theta$, where θ are the coefficients of the sparse representation. Hence, $\mathbf{f}$ can be approximated by a linear combination of K vectors from $\boldsymbol{\Psi}_{3D}$ with $K \ll (N.M.L)$. Specifically, this algorithm estimates a hyperspectral datacube $\hat{\mathbf{f}}$ by solving the optimization problem, $\hat{\mathbf{f}} = \boldsymbol{\Psi}_{3D}\{\mathrm{argmin}_{\theta'}\|\boldsymbol{g} - \boldsymbol{\mathcal{P}}\boldsymbol{\mathcal{T}}\boldsymbol{\Psi}_{3D}\theta'\|_2^2 + \tau\|\theta'\|_1\}$, where $\tau > 0$ is a regularization parameter that balances the conflicting tasks of minimizing the least square of the residuals, while at the same time, it seeks for a sparse solution The basis representation $\boldsymbol{\Psi}_{3D}$ is set as the Kronecker product of three basis $\boldsymbol{\Psi}_{3D} = \boldsymbol{\Psi}_1 \otimes \boldsymbol{\Psi}_2 \otimes \boldsymbol{\Psi}_3$, where the combination $\boldsymbol{\Psi}_1 \otimes \boldsymbol{\Psi}_2$ is the 2D-Wavelet Symmlet 8 basis and $\boldsymbol{\Psi}_3$ is the Discrete Cosine basis. The reconstructions are performed using the new model in Eq. (4.11), and the traditional model in Eq. (4.1) with its respective calibration process described in [**?**]. The regularization parameters needed in the compressive sensing reconstruction algorithm are carefully selected such that each simulation uses the best selectable parameter. Figure 4.7 depicts the reconstructed spectral bands (zoomed area) when 6 shots are captured for the model in (4.1). Figure 4.8 illustrates the reconstruction of the same spectral bands (zoomed area) when the same number of shots are used in the new model. It can be observed that the new model recovers the spectral information with higher accuracy.

| (a) 18.6 dB | (b) 23.2 dB | (c) 23.7 dB | (d) 23.7 dB |
| (e) 17.2 dB | (f) 23.0 dB | (g) 26.4 dB | (h) 22.6 dB |
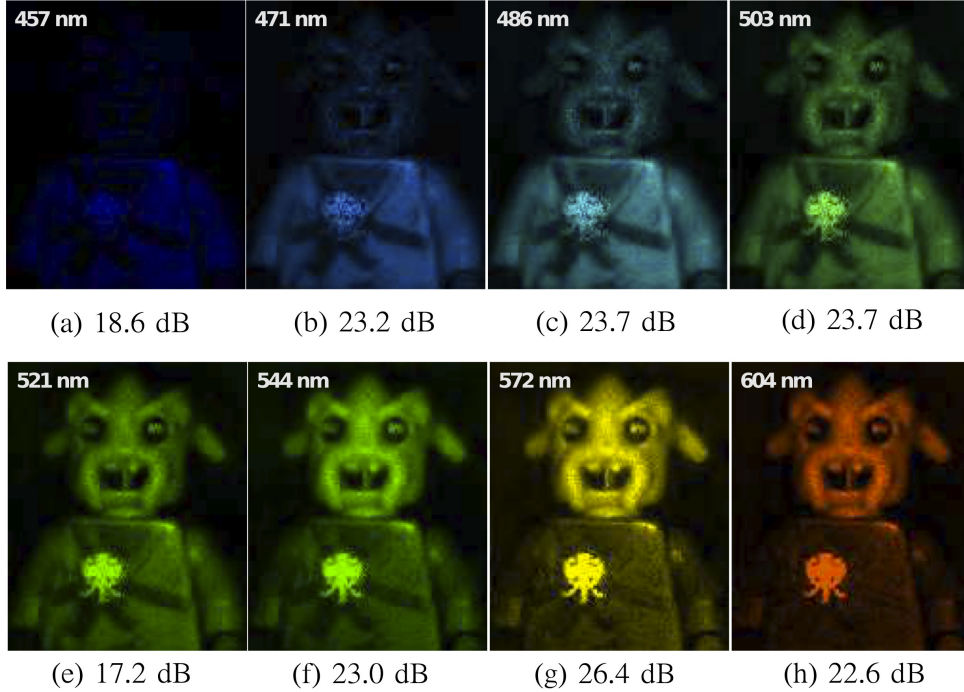
Figure 4.7: Reconstruction using the traditional CASSI model and the corresponding attained PSNR. The average PSNR across the 8 bands is 22.3 dB.

Figure 4.9 shows the PSNR of the reconstructions for the two models as function of the measurement shots. The gain achieved by the new model is quantitatively noticeable by averaging the PSNR of the recovered datacubes. This improvement approaches to 4 dB when more than two FPA shots are used.

4.4 Experimental results

The testbed shown in Fig. 4.10(a) is used to implement the CASSI system and to verify the simulation results [**?**]. It is formed by two subsystems: the first composed by the illuminated target, the objective lens and the DMD; the second by the imaging lenses, the band pass filter, the dispersive element, and the CCD camera. The target is illuminated by a white light source and its reflected light is captured by the objective lens which focuses the light onto the DMD plane, which plays the role of the coded aperture. Afterwards, the reflected light from the DMD is focused by the imaging lenses into the prism

| (a) 23.5 dB | (b) 25.9 dB | (c) 25.9 dB | (d) 26.4 dB |
| (e) 27.9 dB | (f) 28.8 dB | (g) 28.5 dB | (h) 25.7 dB |
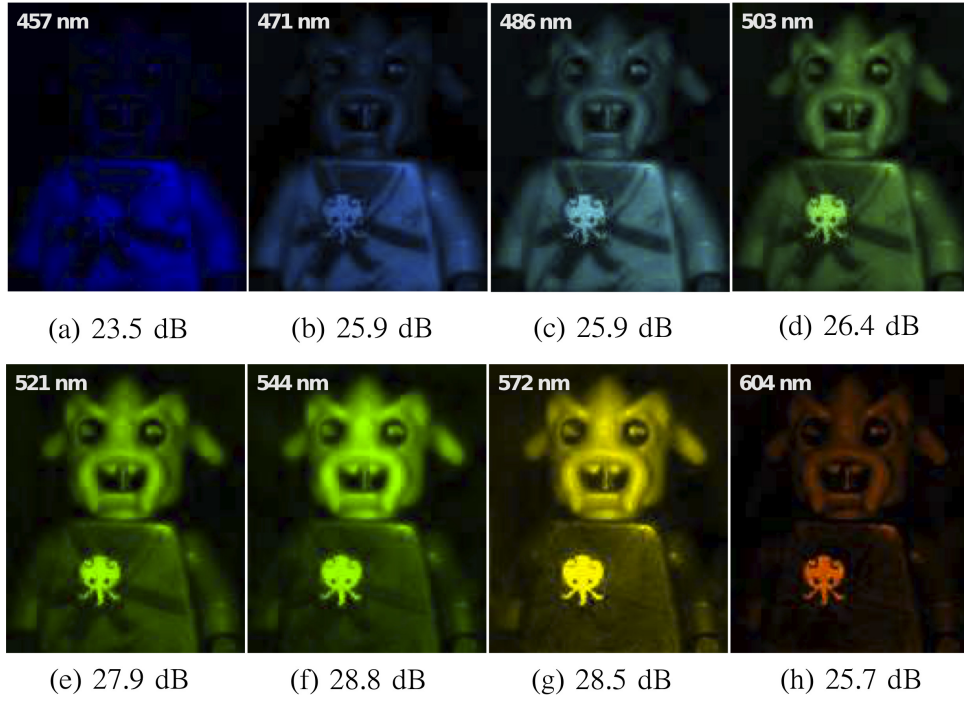
Figure 4.8: Reconstruction using the higher order CASSI model and the corresponding attained PSNR. The average PSNR across the 8 bands is 26.85 dB
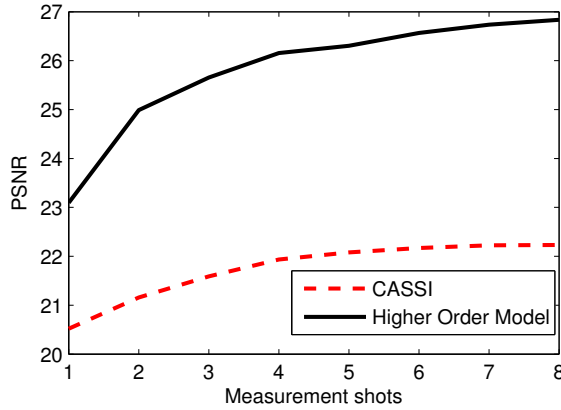
Figure 4.9: Averaged PSNR of the reconstructed datacubes as function of the number of FPA shots. The traditional and the higher order precision models are compared.

imaging plane that disperses the filtered light onto the CCD camera which integrates the underlying 3D hyperspectral image in the 2D FPA.

The testbed setup is characterized in order to reduce the impact of non-linearities, non-uniformities, and external noise artifacts. This process is realized as follows: (a) The light source intensity distribution and the FPA spectral sensitivity are characterized by experimentally analyzing their spectral responses using a USB2000+VIS-NIR Ocean Optics spectrometer with a known spectral response. These non-uniform spectral response curves are taken into account to reduce their impact in the measurement shots; (b) for each one of the 170 captured spectral planes, 10 FPA measurements are captured and averaged to reduce the impact of shot and readout noise; (c) the CCD exposure time is setted to 100 microseconds, in order to improve the signal-to-noise-ratio of the aperture code at each wavelength; (d) the dispersive element is characterized in order to take into account its non-linear response curve and the resultant bandwidth of
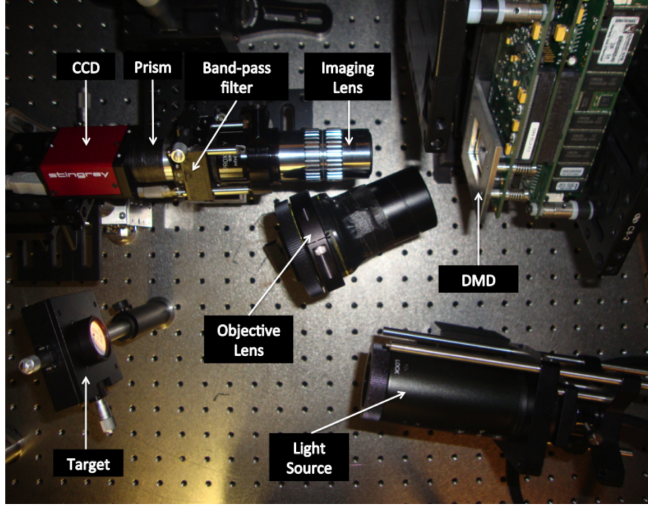
(a) CASSI testbed setup
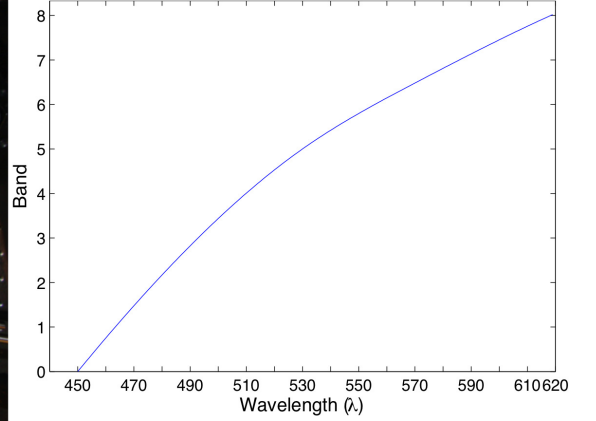
(b) Non-linear response of the Amici prism

Figure 4.10: (a) The CASSI testbed setup and its six optical elements: objective lens, DMD, imaging lenses, band-pass filter, prism and CCD; (b) non-linear dispersion response of the Amici prism between $\{450 - 620\}$nm.

each spectral band. After characterization of the testbed and in order to observe the oblique voxel effect impinging into the FPA as explained in Fig. 4.3, a measurement shot is captured using monochromatic light at 502 nm as the input of the system. The resultant measurement is depicted in Fig. 4.11.
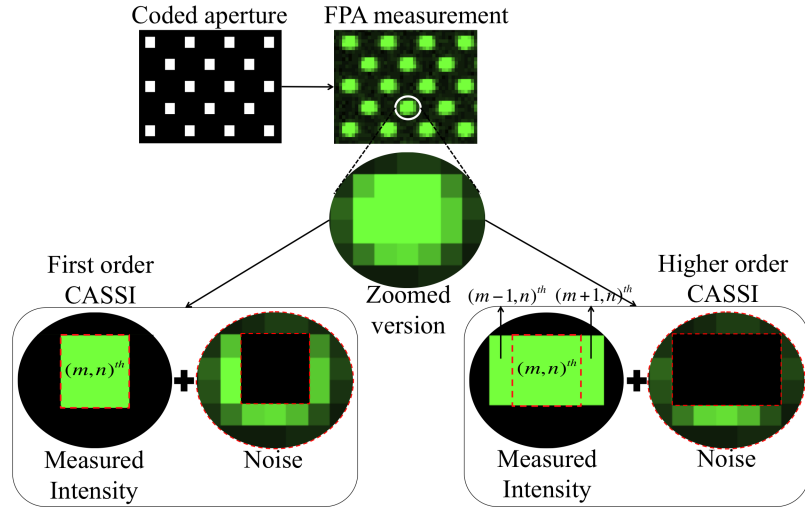
Figure 4.11: FPA measurement at 502 nm. The coded aperture (upper-left) is used in order to isolate the effect of a single voxel impinging onto the FPA (upper right). A zoomed version of a single FPA pixel shows the measured intensity taken into account for each of the discretization models. The energy classified as noise and blur by the first order and the higher order models, is shown.

This measurement is taken using a test coded aperture with enough space (3 'off' features) between each 'on' feature, thus, allowing the isolation of the effect of a single voxel impinging onto the FPA. Then, a zoomed version of a single FPA pixel is analyzed. Firstly, it can be confirmed that energy belonging to a single datacube voxel impinges principally in a single FPA pixel $(m, n)^{th}$, and a smaller portion is projected into its neighbors $(m - 1, n)^{th}$ and $(m + 1, n)^{th}$. Second, the first order model accounts only for the energy impinging on the principal pixel, discarding the energy around it, or classifying it as noise
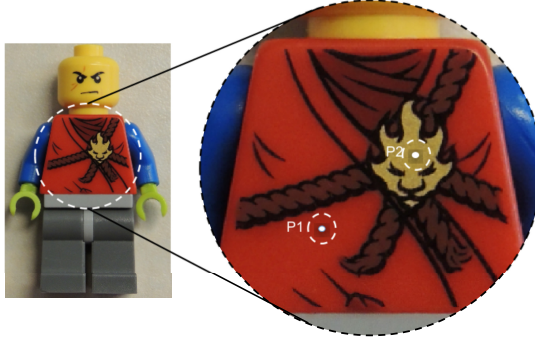
Figure 4.12: Objects in scene used in the experimental comparison

Region	Band							
	1	2	3	4	5	6	7	8
R_0	0.30	0.27	0.27	0.26	0.26	0.25	0.24	0.24
R_1	0.42	0.46	0.46	0.49	0.52	0.55	0.56	0.56
R_2	0.28	0.27	0.27	0.25	0.22	0.20	0.20	0.20

Table 4.1: Weights R_i and their distribution across spectral bands

or blur. The energy discarded by the first order model, is taken into account in the higher order model by the weights w_{mnku}. Notice that the energy considered as noise and blur by the traditional CASSI is leveraged by the use of a calibration cube at the reconstruction stage, while the proposed model finds the weights distribution in an off-line process. Then, the proposed higher-precision computational model becomes more suitable for reconfigurable multi-shot CASSI where multiple coded apertures are used sequentially.

For experimental purposes, the objective scene used is depicted in Fig. 4.12. The coded apertures are realizations of a Bernoulli random variable with $p = 0.5$, realized by a DMD as explained in [?] exhibiting 128×128 pixels. The dispersive element is an Amici prism exhibiting the non-linear response shown in Fig. 4.10(b). To match with the pitch of the coded aperture features and accounting for the dispersion process, 128×136 pixels of the CCD are required. The weight distribution extraction is performed using Eq. (4.10). As a result, three $128 \times 128 \times 8$ weight datacubes were obtained, each one accounting for the regions R_0, R_1 and R_2 as described in Fig. 4.4. By averaging each weight datacube per band, a succinctly version can be shown in Table 4.1. Notice that when misalignments between the coded aperture and the FPA occur, the weights distributions may vary along the regions.
The GPSR algorithm is employed in the reconstruction of the underlying hyperspectral scene, with parameters as described in the simulations section [?]. Figure 4.13 depicts the 8 reconstructed spectral bands for 6 shots when the models in Eq. (4.1) and Eq. (4.11) are used. Here, the higher quality reconstruction obtained when the proposed model is used in the simulations section is confirmed. Notice that the test object intensity spans principally along the last four bands, and the reconstruction quality of the proposed model overcomes the one from the traditional CASSI model. In particular, the improvement can be clearly noticed in the fifth band (524 nm), where the higher-order CASSI estimates a better shape of the face, compared with the same band from the traditional CASSI. Furthermore, the improved results can also be noticed in the spectral signatures of two particular points (P1 and P2 in Fig. 4.12) depicted in Fig. 4.14. The resulting reconstructed datacubes curves are compared against their respective ground truth curves measured by the use of the commercial spectrometer.

It is important to point out here, that the simulations setup differs from the experimental setup in the following aspects: The former performs the CASSI and higher-order CASSI FPA measurements starting with a hyperspectral datacube captured off-line and taken as the ground truth. The coded apertures as well as the non-linear prism dispersion curve are simulated, and the weights distribution (w_{mnku}) given by Eq. (4.10) are then synthetically obtained. Noise, as well as blur and misalignment between the

coded aperture and the CCD were not added to the model. It can be assumed that this is the ideal case scenario. The latter uses the experimental testbed depicted in Fig. 4.10(a) to capture the FPA measurement shots. The same fluorescent white illumination source was employed for both cases. However, in the experimental results, the FPA measurements are contaminated by optical aberrations, as well as noise and misalignment between the CCD and the coded aperture. Consequently, the weights distribution (w_{mnku}) presented in Table. 4.1, is experimentally obtained from the non-linear prism dispersion curve depicted in Fig. 4.10(b), which is characterized by the use of a monochromatic light source as the input of the testbed ranging between $450nm$ and $650nm$. The reconstruction algorithm utilized (GPSR) is equal for both simulations and experimental results, but differs for each compared model (CASSI vs Higher-Order CASSI). The objects used as targets in the simulation section differs from the one used in the experimental setup. Due to field of view restrictions in the optical instruments, a smaller but spatially richer scene was selected for the latter.

4.5   Conclusions

A higher order precision discretization model for coded aperture-based spectral imaging systems has been developed. This model accounts for the inter-voxel projections onto each pixel detector which is disregarded by the first order discretization model. This, in turn, allows for the reconstruction of hyperspectral signals with higher PSNR. Simulations achieve a 4 dB improvement, while testbed experiments visually confirm the simulations results. The proposed model is less-dependent on time-demanding calibration processes, thus leading to multiple-frame CASSI systems to be more suitable for real applications.
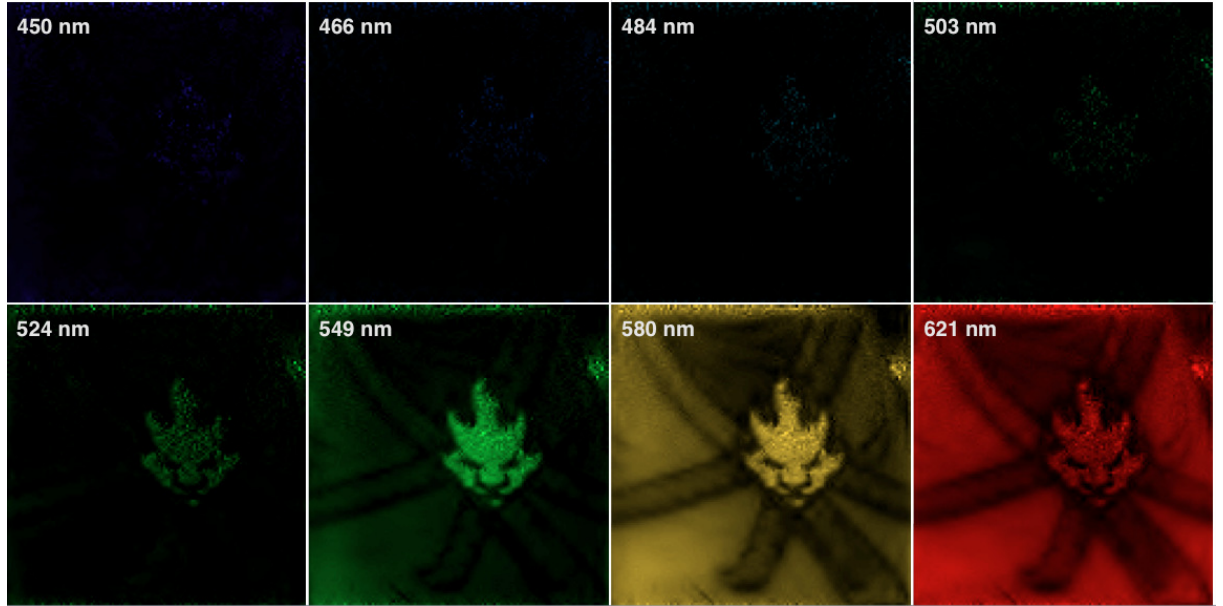
(a) CASSI
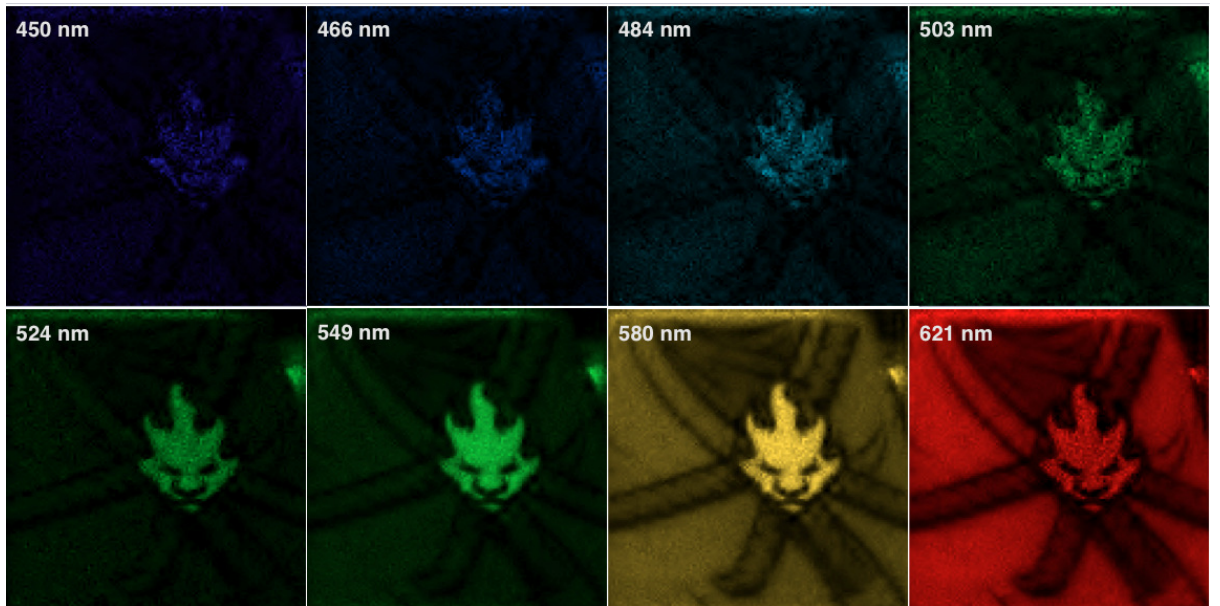
(b) Higher-order CASSI

Figure 4.13: Reconstruction of the 8 spectral bands using (a) the traditional CASSI model, and (b) the proposed higher-order CASSI model.
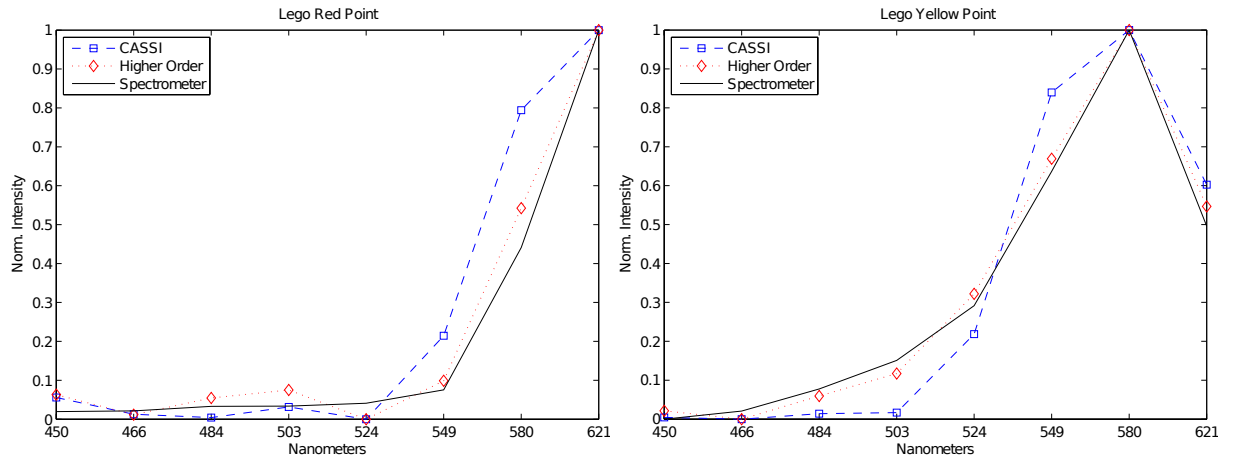
(a) Red point (P1 in Fig. 12)   (b) Yellow point (P2 in Fig. 12)

Figure 4.14: Spectral signatures comparison from given points in Fig. 12.

Chapter 5

Compressive Hyperspectral Imaging Testbed

In this chapter, we present a dispersive optical element-based approach for building a CS-HSI system. This system has a compact optical/mechanical architecture, along with a higher efficiency in utilizing the DMD reflected imaging irradiance and therefore, spectral images can be concurrently reconstructed from this system. Additionally, the acquisition of spatial/spectral image cubes using the CS-HSI system is free from mechanical or temporal scanning processes and thus this acquisition process virtually does not cause any time penalty.

5.1 Coded Aperture Snapshot Spectral Imaging System

Conventional spectral imaging systems usually rely on some mechanical or temporal scanning processes to acquire the complete spatial/spectral information of an imaging scene [49]. The time penalty caused by the scanning process unavoidably undermines the performance of spectral imaging systems in low light or high speed imaging applications. To circumvent the scanning process, the so-called Coded Aperture Snapshot Spectral Imaging (CASSI) system was developed [50-53]. Figure 5.1 shows the schematic drawing of the CASSI system. CASSI systems usually use photomasks to implement CS measurement patterns.
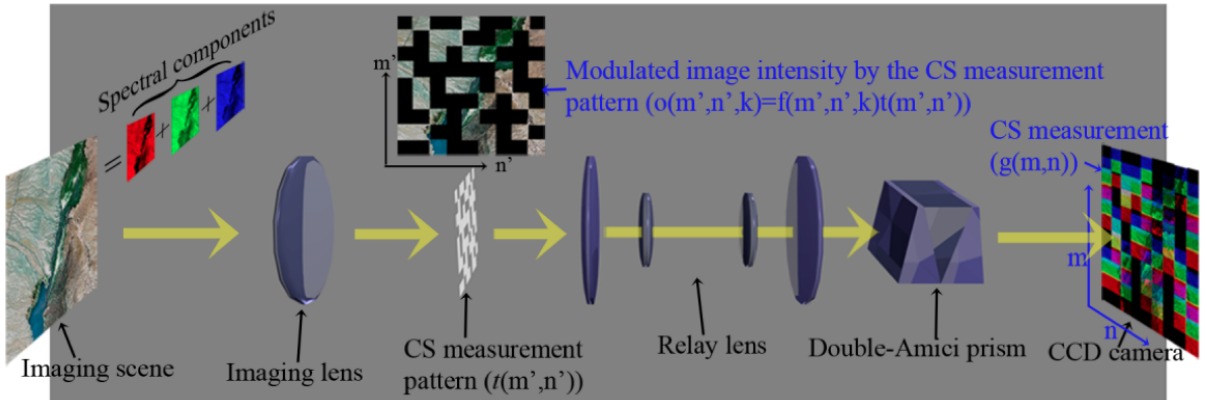
Figure 5.1: Schematic drawing of the CASSI system.

Binary random patterns are widely used as CS measurement patterns in such systems. The photomask is installed on the image plane of an imaging lens such that intensities of optical images formed on the photomask can be modulated by the CS measurement pattern coated on it. In this process, the continuous spatial information of the optical image is pixelated into an array of square pixels by the photomask. In the following discussion, we use $f(m', n', k)$ to represent the spatial/spectral information of the optical

image formed on the photomask, and use $t(m', n')$ to represent the CS measurement pattern. The coordinates m' and n' are used to locate a pixel on the photomask ($m' = 1, 2, \ldots, M'$ and $n' = 1, 2, \ldots, N'$). The coordinate k is used to describe the location of a spectral image in the wavelength (λ) direction of the image cube ($k = 1, 2, \ldots, K$). The spatial/spectral information of the original optical image after being modulated by the CS measurement pattern can be represented as: $o(m', n', k) = f(m', n', k)t(m', n')$. A relay lens is used to transfer the modulated image intensity from the photomask onto a CCD camera. In between the exit aperture of the relay lens and the CCD camera, an optical dispersive element (such as a prism) is used to spatially separate the spectral components of the modulated image intensity. In other words, a spectrally dispersed image of the modulated image intensity is formed on the CCD camera, which represents a set of CS measurement results for the original image cube. We use $g(m, n)$ to represent that spectrally dispersed image, where (m, n) is the coordinate system used to locate a pixel on the optical plane where the CCD camera is installed. If the magnification of the relay lens/double-Amici prism structure is A, we have $m = Am'$ and $n = An'$. In following discussions, we assume $A = 1$.

In [53], optical operations realized by the CASSI system were described as punch, shear, and smash. Figure 5.2 provides an illustrative explanation for those optical operations. In Fig. 5.2, we only show three spectral channels in the original image cube, including a red channel, a green channel, and a blue channel. The spatial shift of different spectral channels caused by the prism happens only in the x direction on the CCD camera plane and we call that direction the dispersion direction of the CASSI system. Also in Fig. 5.2, the green spectral channel is spatially shifted from the red channel by 1 CCD pixel to the right in the dispersion direction, and the blue channel is shifted from the red channel by 2 CCD pixels to the right.
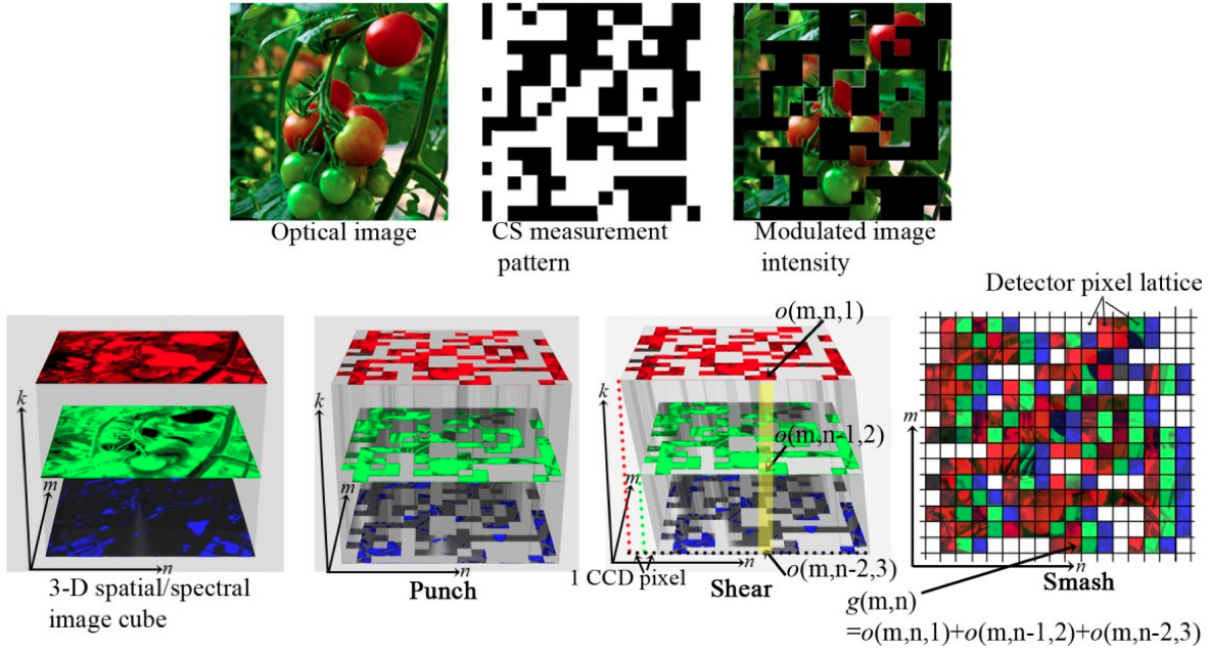
Figure 5.2: Optical operations realized by the CASSI system.

The first optical operation realized by the CASSI system is called punch, wherein closed apertures in the photomask punch the spatial/spectral information away from the original image cube in corresponding pixel locations. The second operation is called shear, wherein different spectral components of the punched image cube are spatially separated from each other along the dispersion direction, due to the dispersion performance of the prism. The last optical operation is called smash, wherein the continuous information of the sheared image cube is digitally sampled and collected by a CCD camera. Those optical operations were modeled as a system transfer function H in [51-53]. If we use g to represent the spectrally dispersed

image captured by the camera, the image formation process of the CASSI system can be modeled as:

$$g = Hf. \tag{5.1}$$

5.2 Transfer Matrix of the CASSI System

In Fig. 5.2, we note that the intensity of the CS measurement result g at the pixel location (m, n) equals to the intensity of the first spectral channel ($k = 1$) of the modulated image intensity at the pixel location (m, n) plus the intensity of the second spectral channel ($k = 2$) at the pixel location $(m, n-1)$, plus the intensity of the third spectral channel ($k = 3$) at the pixel location $(m, n-2)$, and so on. Following this logic, for an $M \times N \times K$ image cube, the CS measurement result generated from the CASSI system can be represented as:

$$g(m, n) = \begin{cases} \sum_{k=1}^{n} o(m, n-k+1, k), & \text{if } 1 \leq n \leq K-1 \\ \sum_{k=1}^{K} o(m, n-k+1, k), & \text{if } K \leq n \leq N \\ \sum_{k=n}^{K} o(m, n-k+1, k), & \text{if } N+1 \leq n \leq N+K-1 \end{cases} \tag{5.2}$$

where $o(m, n-k+1, k) = f(m, n-k+1)t(m, n-k+1)$. To determine the system transfer matrix H, we transform the 2D and 3D data arrays in Eq. 5.2, which are g and o, respectively, into 1D vector forms by concatenating their column vectors. In their 1D vector forms, g has $M \times (N+K-1)$ data entries and f has $M \times N \times K$ data entries. Thus, the transfer matrix H has a pixel dimension of $M \times (N+K-1)$ by $M \times N \times K$, which is a rectangle with an aspect ratio smaller than 1. We define the aspect ratio of the transfer matrix to be the down-sampling ratio of the CASSI system, which is denoted as R_{CASSI} in this work, and we have:

$$R_{CASSI} = \frac{M \times (N+K-1)}{M \times N \times K} = \frac{N+K-1}{N \times K}. \tag{5.3}$$

Apparently, the down-sampling ratio decreases with the increment of the number of spectral channels in the image cube. In their 1D vector representations, the pixel location (m, n) in g becomes the $((n-1)M+m)^{th}$ data entry and the pixel location (m, n, k) in f becomes the $((k-1)MN+(n-1)M+m)^{th}$ data entry. The pixel location $(m, n-k+1, k)$ in f becomes the $((k-1)MN+(n-k)M+m)^{th}$ data entry. If we use the 1D coordinate $((n-1)M+m)$ to replace the 2D coordinate (m, n) in Eq. 5.2, use $((k-1)MN+(n-1)M+m)$ to replace (m, n, k) and let $z = (n-1)M+m$, which represents the pixel index in the 1D form of the CS measurement result g, the center term of Eq. 5.2 can be modified as:

$$\begin{aligned} g(z) &= \sum_{k=1}^{K} o((k-1)MN+(n-k)M+m) \\ &= \sum_{k=1}^{K} o((k-1)MN+nM-kM+m) \\ &= \sum_{k=1}^{K} o((k-1)MN+nM-M+M-kM+m) \\ &= \sum_{k=1}^{K} o((k-1)MN+z-(k-1)M), \end{aligned} \tag{5.4}$$

which is valid when $(K-1)M+1 \leq z \leq NM$. Similarly, the top term in Eq. 5.2 can be modified as:

$$g(z) = \sum_{k=1}^{\lceil \frac{z}{M} \rceil} o((k-1)NM+z-(k-1)M), \tag{5.5}$$

which is valid when $1 \leq z \leq (K-1)M$. $\lceil \frac{z}{M} \rceil$ represents the ceiling function of $\frac{z}{M}$. The bottom term in Eq. 5.2 can be modified as:

$$g(z) = \sum_{\lceil \frac{z}{M} \rceil}^{K} o((k-1)NM+z-(k-1)M), \tag{5.6}$$

which is valid when $MN + 1 \leq z \leq M(N + K - 1)$.

The explicit expression of the transfer matrix H can be derived from Eq. 5.4 through Eq. 5.6. Here we use a simple example to demonstrate the derivation process, where we consider a small image cube which has $M = N = 3$ and $K = 3$. The CS measurement pattern t has a pixel dimension of 3×3, and the CS measurement result g has a pixel dimension of 3×5. In their 1D vector forms, t and g have 9 and 15 data elements, respectively. When, $1 \leq z \leq 6$, Eq. 5.5 should be used. When $z = 1$, $\lceil \frac{z}{M} \rceil = 1$ and we have $g(1) = \sum_{k=1}^{1} = o((k-1)NM + 1 - (k-1)M) = o(1) = t(1)f(1)$. Similarly, we have $g(2) = t(2)f(2)$ and $g(3) = t(3)f(3)$. In other words, data entries in pixel locations of (1,1), (2,2), and (3,3) in the transfer matrix H are $t(1)$, $t(2)$, and $t(3)$, respectively. The last are the first three data entries in the 1D vector form of the CS measurement pattern. When $z = 4$, also from Eq. 5.5, $\lceil \frac{z}{M} \rceil = 2$ and we have $g(4) = \sum_{k=1}^{2} o((k-1)NM + 4 - (k-1)M) = o(4) + o(10) = t(4)f(4) + t(10)f(10)$. $t(10)$ represents the intensity modulation implemented on the first pixel location of the second spectral channel in the original image cube. Since in the punch process, the same CS measurement pattern was used to implement the intensity modulation on all the spectral channels of the original image cube, the intensity modulation implemented on the first pixel location in the second spectral channel equals to the intensity modulation implemented on the first pixel location in the first spectral channel and thus $t(10) = t(1)$. Similarly, we have $g(5) = t(5)f(5) + t(2)f(11)$, and $g(6) = t(6)f(6) + t(3)f(12)$. In other words, data entries in pixel locations of (4,4), (4,10), (5,5), (5,11), (6,6), (6,12) in the transfer matrix are $t(4), t(1), t(5), t(2), t(6)$, and $t(3)$ respectively. Other data entries in the transfer matrix can be derived in a similar manner and the resulted transfer matrix H is shown in Fig. 5.3. The values of those empty entries in this transfer matrix are all 0.

t(1)																										
	t(2)																									
		t(3)																								
			t(4)						t(1)																	
				t(5)						t(2)																
					t(6)						t(3)															
						t(7)						t(4)						t(1)							
							t(8)						t(5)						t(2)						
								t(9)						t(6)						t(3)					
															t(7)						t(4)					
																t(8)						t(5)				
																	t(9)						t(6)			
																								t(7)		
																									t(8)	
																										t(9)

Figure 5.3: Transfer matrix of the CASSI system for an $M = N = K = 3$ image cube.

For an $M \times N \times K$ image cube, the transfer matrix looks like this:

We can see that from row $(K-1)M + 1$ to row NM, each row in the transfer matrix contains a random data sequence that has K data entries. For rows 1 to $(K-1)M$ and rows $MN + 1$ to $M(N + K - 1)$, each row in the transfer matrix contains a random data sequence that has $\lceil \frac{z}{M} \rceil$ and $K - \lceil \frac{z}{M} \rceil$ data entries, respectively, where z represents the row number of the H matrix, which is identical to the row number of the CS measurement result g. As such, each row in the transfer matrix H implements a random intensity modulation (random sampling) on the original image cube f, and each pixel in the spectrally dispersed image g represents a CS measurement result for f. In CASSI systems, random sampling processes are implemented on the 3D spatial/spectral image cube of optical images. We utilized a Two Step Iterative Shrinkage/Thresholding (TwIST) algorithm to solve the image reconstruction problem, which considers the following Total Variation (TV)-regularized minimization problem [51-54]:

$$argmin_{f \in R^N} \|g - Hf\|_2^2 + \tau TV(f), \tag{5.7}$$

where τ is a regularization parameter for the Total Variation regularizer TV(f), which is defined as:

$$TV(f) = \sum_k \sum_{m,n} \sqrt{(f(m+1, n, k) - f(m, n, k))^2 + (f(m, n+1, k) - f(m, n, k))^2}. \tag{5.8}$$
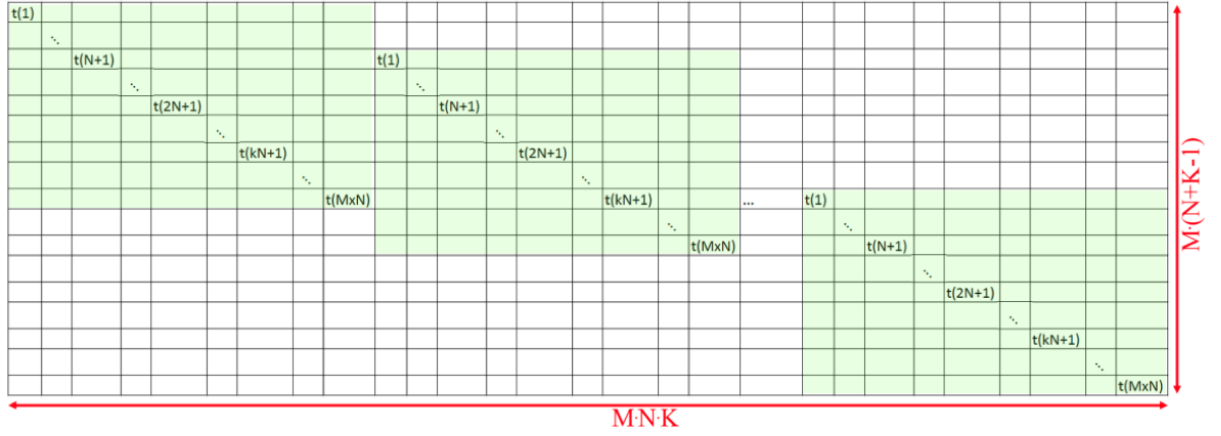
Figure 5.4: Transfer matrix for an $M \times N \times K$ image cube.

5.3   Simulations

We simulated the punch, shear, and smash operations of the CASSI system in the simulation setting (we used Matlab as the simulation tool) and used the TwIST algorithm to reconstruct the original image cube based on the simulated CS measurement results. In this simulation, a $256 \times 256 \times 24$ data cube was used as the imaging target, which is shown in Fig. 5.5(a).
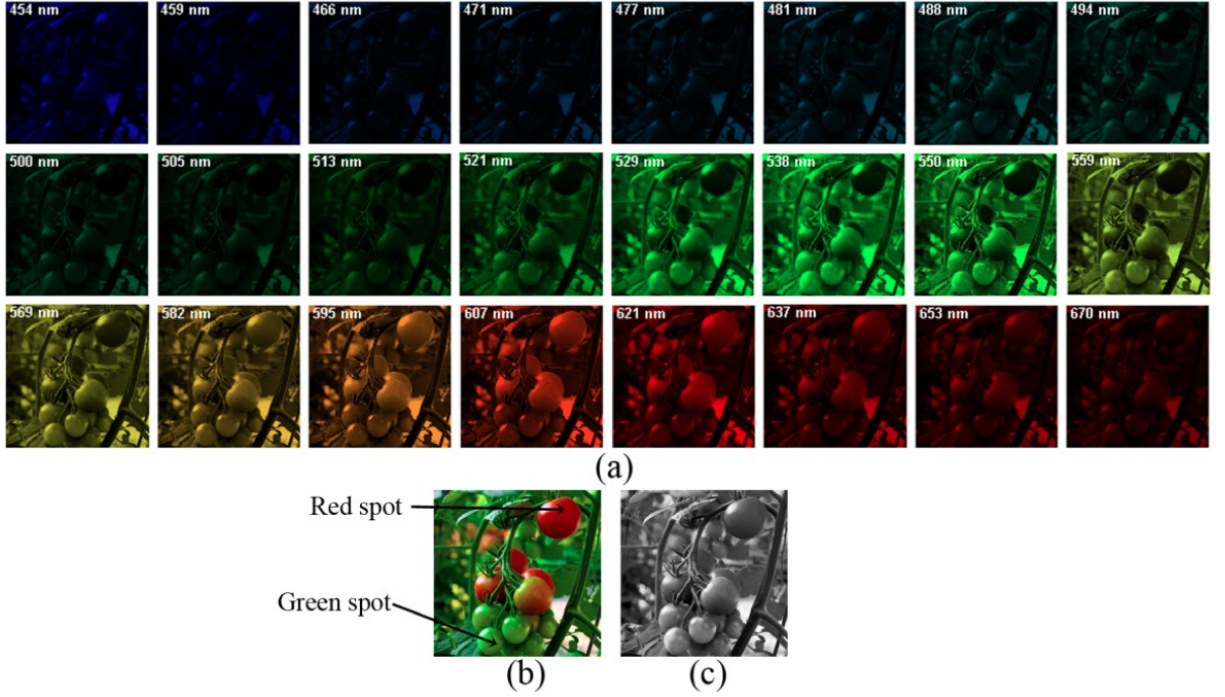

Figure 5.5: (a) Spatial/spectral image cube of the simulation target. (b) RGB image of the simulation target. (c) Optical image of the simulation target.

Figures 5.5(b) and (c) show an RGB image and an optical image of the simulation target. The RGB image was generated by using the 454 nm, 550 nm, and 621 nm spectral channels to represent the blue, green, and red colors in the RGB data format. In the RGB image, we can see that this simulation target is composed of some red and green tomatoes. The optical image is the intensity combination of all the 24 spectral channels of the image cube. In Fig. 5.6, we show the normalized intensity variations of two

pixel locations in the image cube, which are labeled as the red spot (y=36, x=206) and the green spot (y=222, x=122) in Fig. 5.5(b). The red spot is located on a red tomato and the green spot is located on a green tomato. Those intensity variations can be considered as the spectral curves of the imaging target at those two pixel locations. For the red spot, the spectral curve has an intensity peak at the spectral channel 20, which represents a wavelength of 607 nm. For the green spot, there is an intensity peak at the spectral channel 14, which represents a wavelength of 538 nm.
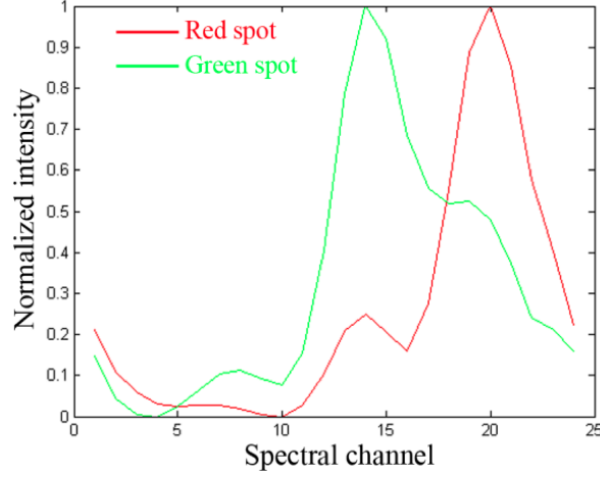

Figure 5.6: Spectral curves measured at the red spot and the green spot on the imaging target.

A 256×256 binary random pattern was used to implement the CS measurement process, which is shown in Fig. 5.7(a). In this CS measurement pattern, half of its pixels are set in the on condition and thus we say this pattern has an on pixel percentage of 50%. The CS measurement result generated with this random pattern is shown in Fig. 4.7(b), which was fed into the TwIST algorithm for reconstructing the original image cube. In this simulation, we assume the spectral dispersion caused by the prism happens only in the horizontal direction on the CCD camera plane and adjacent spectral channels are spatially separated by 1 pixel. Therefore, the CS measurement result has a pixel dimension of 256×279. In the TwIST algorithm, we set the regularization parameter τ to be 0.1 and the number of optimization iterations to be 100. The image reconstruction took about 650 seconds using a DELL desktop (model: precision 690) installed with Windows XP 32 bit operation system and 4GB memory.
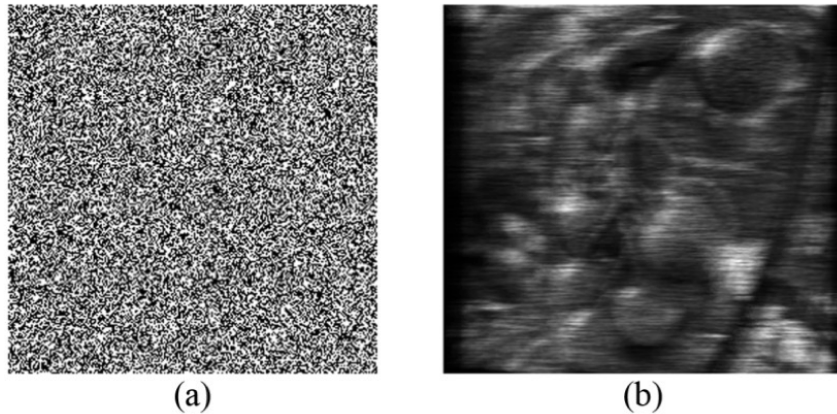

Figure 5.7: (a) A 256×256 CS measurement pattern. (b) Simulated CS measurement result for the image cube shown in Fig. 5.5(a).

Figure 5.8(a) shows the reconstructed image cube. Figures 5.8(b) and (c) show the RGB image and the optical images of the reconstructed image cube.
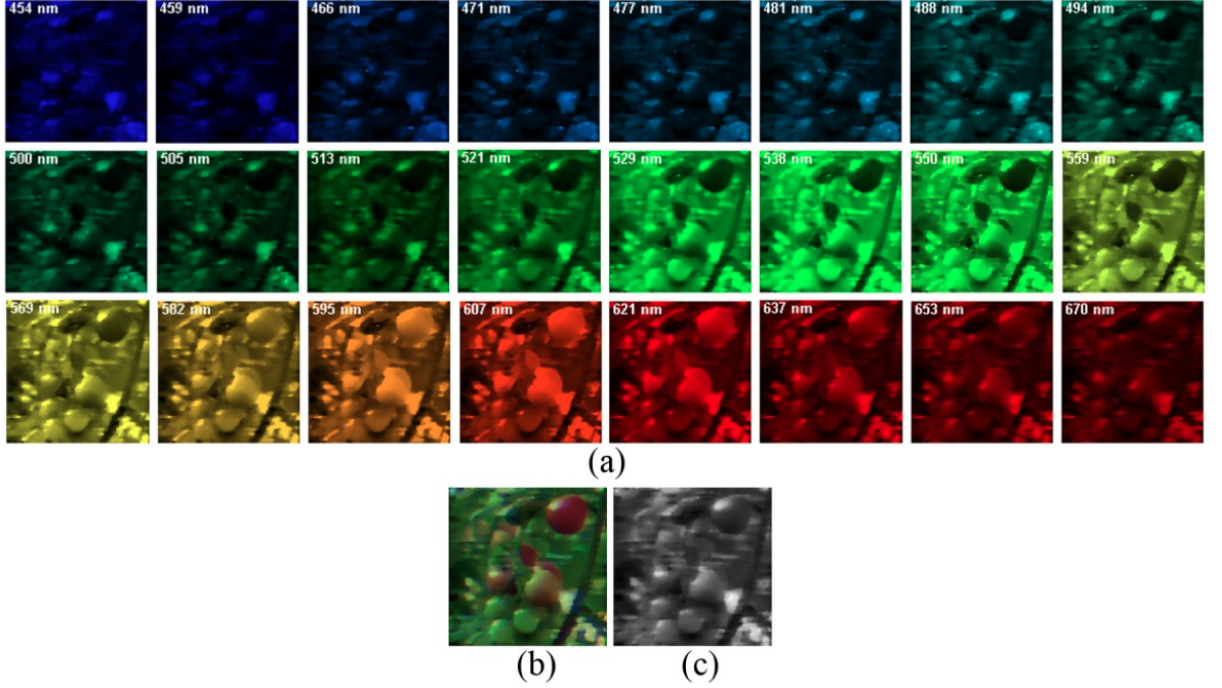
Figure 5.8: (a) Reconstructed image cube. (b) RGB image of the reconstructed image cube. (c) Optical image of the reconstructed image cube.

In Fig. 5.8(a), we can see that the red tomatoes in the imaging target were reconstructed with strong intensities in red spectral channels (595 nm to 637 nm) and green tomatoes were reconstructed with strong intensities in green spectral channels (529 nm to 582 nm). The PSNR value of the reconstructed optical image is 17.36 dB. In Fig. 5.9, we show normalized intensity variations of the reconstructed image cube at the red spot and the green spot (solid lines). Those intensity variations can be considered as the reconstructed spectral curves at those two pixel locations. Also in Fig. 5.9, spectral curves of the original image cube are shown in dotted lines. We can see that the reconstructed spectral curves have pretty good matches to the original ones. The Mean Square Errors (MSEs) of the deviations from the reconstructed spectral curves to the original spectral curves are 0.017% and 0.027% for the red and green spots, respectively.

5.4   DMD-based CASSI System

Conventional CASSI systems use photomasks to implement CS measurement patterns. In such systems, the pattern replacement process is a very time-consuming process. A new photomask needs to be lithographically fabricated and the entire system needs to be re-aligned after the installation of the new photomask. To expedite the pattern replacement process, we propose using a DMD to implement CS measurement patterns. As such, new patterns can be implemented without optical and/or mechanical modifications to the system. More importantly, the DMD provides a virtually unlimited selection pool for CS measurement patterns, such that patterns of different designs can be grouped to realize various Multi-Shot CS (MS-CS) measurement processes, which, as will be demonstrated in the following sections, can effectively enhance the quality of the reconstructed image cubes [52,55]. Figure 5.10 shows the schematic drawing of the DMD-based CASSI (DMD-SSI) system.

As can be seen in Fig. 5.10, the DMD-SSI system can be considered as a two- arm system, including an imaging arm and a relay-dispersion arm. In the imaging arm, a DMD is installed on the image plane of an imaging lens, which imposes intensity modulations on optical images formed on it. In the relay-dispersion arm, image intensities modulated by DMD patterns are collected into a relay lens/double-Amici prism
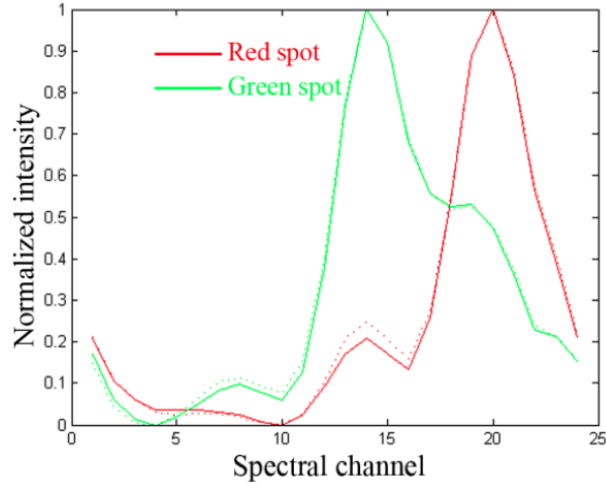
Figure 5.9: Spectral curves measured at the red spot and the green spot in the reconstructed image cube (solid lines) and spectral curves measured at those two locations in the original image cube (dotted lines).
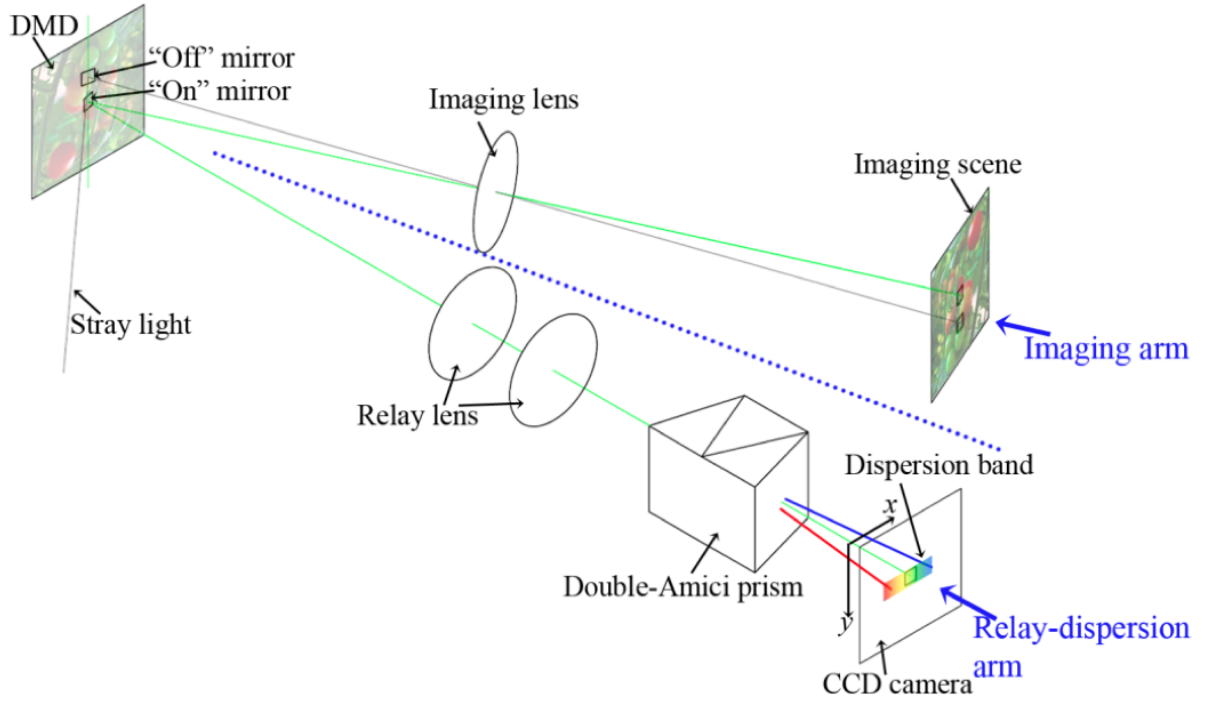

Figure 5.10: Schematic drawing of the DMD-SSI system.

structure. On the image plane of that relay lens/double-Amici prism structure, where a CCD camera is installed, spectrally dispersed images of the modulated image intensities are formed. Those spectrally dispersed images represent different sets of CS measurement results for the original image cube. Each on pixel on the DMD mirror plane results in a dispersion band on the CCD camera and CS measurement results are essentially intensity combinations of dispersion bands at different spatial locations on the CCD camera. The construction of the imaging arm of the DMD-SSI system is straightforward, which only involves using an imaging lens to form optical images on the DMD mirror plane. The construction of the relay-dispersion arm of the DMD-SSI system is more complicated than the imaging arm. Figure 5.11(a) shows the Zemax ray tracing model of the relay-dispersion arm installed in our DMD-SSI system.
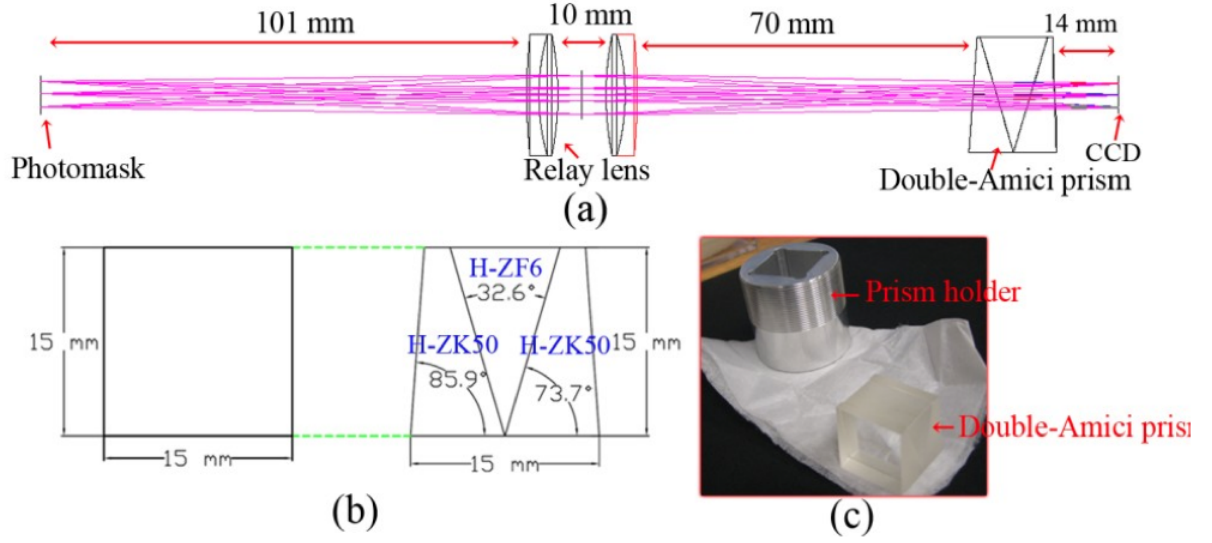
Figure 5.11: (a) Zemax ray tracing model for the relay-dispersion arm of the DMD-SSI system. (b) Optical design of the double-Amici prism. (c) Manufactured double-Amici prism and its mechanical holder.

In this setup, we used a pair of visible achromatic lenses (Thorlabs, stock number: AC254-100-A-ML) to realize the functionality of optical relay. The double- Amici prism was installed in between the exit aperture of the relay lens and the CCD camera. Figure 5.11(b) shows the optical design of the double-Amici prism, which is composed of three wedge prisms including a high dispersion wedge prism sandwiched in between two low dispersion ones. The angles and thicknesses of the three wedge prisms were optimized such that the wavelength component of 550 nm of the DMD reflected light can go through the double-Amici prism without angular or spatial deviations from the optical axis. Other wavelength components suffer from different levels of angular deviations when propagating through the double-Amici prism. We used CDGM glasses H-ZF6 (refractive index $n = 1.7552$, Abbe number $v_d = 24.5474$) and H-ZK50 (refractive index $n = 1.607$, Abbe number $v_d = 56.6572$) to build the high and low dispersion wedge prisms. Figure 5.11(c) shows the manufactured double-Amici prism and its mechanical holder.

Figure 5.12 shows the Zemax spot diagram of the relay lens/double-Amici prism structure at 0 field angle. In this spot diagram, we can see that due to the dispersion performance of the double-Amici prism, the wavelength components of 450 nm and 650 nm are spatially separated by about 220 μm. This spatial separation spans over approximately 22 CCD pixels and thus results in 22 spectral channels in the reconstructed image cubes. The number of spectral channels in the reconstructed image cubes can be increased or reduced by moving the prism closer to or further away from the relay lens [56]. In our experimental setup, we usually align the optics to ensure the acquisition of 24 spectral images in the reconstructed image cubes. From Fig. 5.12, we can also observe a non-linear dispersion performance of the double- Amici prism. We observe that the spatial separation between the wavelength components of 450 nm and 500 nm (50 nm difference) is 88 μm, whereas the spatial separation between the wavelength components of 600 nm and 650 nm (also 50 nm difference) is only about 30 μm. We can see that this prism is more dispersive in the short wavelength region of the visible spectrum than in the long wavelength region. This non-linear dispersion performance was also discussed in [51].

We experimentally realized the DMD-SSI in our lab, which is shown in Fig. 5.13. The DMD used in this setup is a TI Discovery 1100 series DMD product. The imaging lens is a Leica COLORPLAN-P2 projector lens, which has a good control over chromatic aberrations. The focal length of the imaging lens is 90 mm and its f-number is 2.5. The CCD camera is an AVT Stingray F031B camera, which has a pixel dimension of 540×640 and a pixel pitch of 9.9 μm. In this experimental setup, we use a 2×2
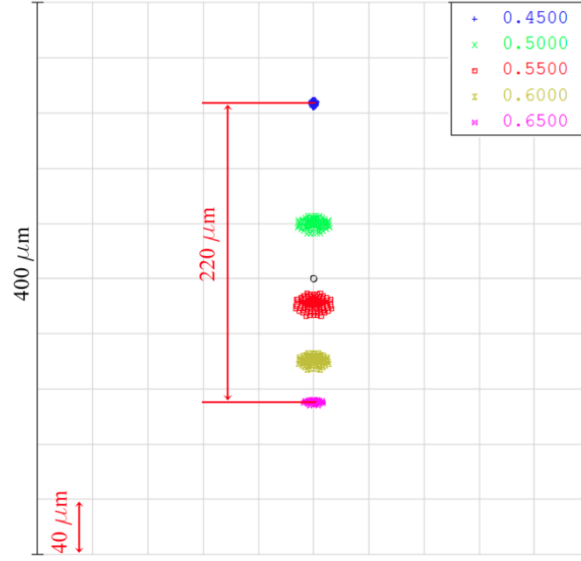
Figure 5.12: Spot diagram of the relay lens/double-Amici prism structure at 0 field angle.
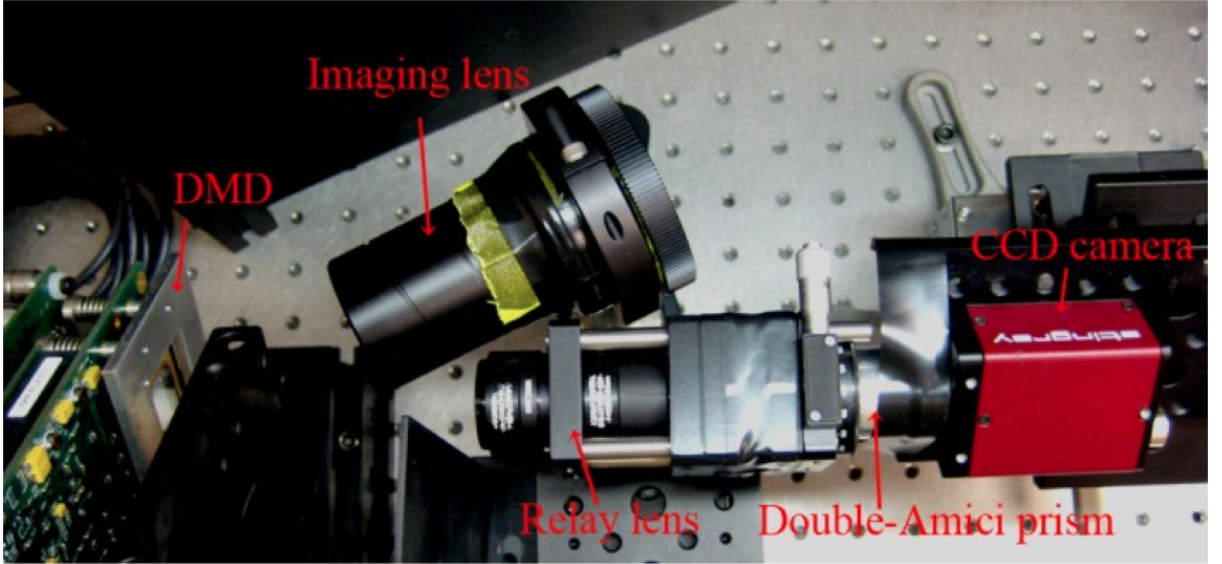

Figure 5.13: Experimental setup of the DMD-SSI system.

DMD super-pixel ($27.36 \times 27.36 \mu m^2$) to represent one pixel in the CS measurement pattern, and image one DMD super-pixel onto a 3×3 CCD super-pixel ($29.7 \times 29.7 \mu m^2$).

5.5 Calibration of the CASSI System

The simulation result presented in Section 5.3 demonstrated that the TwIST algorithm can effectively reconstruct the original image cube using CS measurement results generated from an ideal CASSI system. However, in experimental settings, practical issues such as noise contaminations and/or optical aberrations make the collection of ideal CS measurement results impossible. In the following example, we present a simple case demonstrating that external noise poses negative impact on the image reconstruction quality. We also introduce a simple calibration process can be used to alleviate that negative impact.
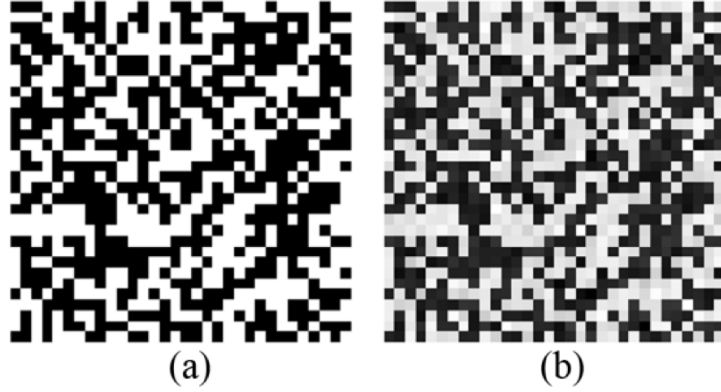
Figure 5.14: (a) Partial view of an ideal CS measurement pattern (32×32 pixels). (b) A noise-contaminated CS measurement pattern generated by adding white noise to the pattern shown in Fig. 5.14(a).

Figure 5.14(a) shows a partial view (32×32 pixels) of an ideal CS measurement pattern, which is a 256×256 binary random pattern. The white pixels in this pattern represent the binary value 1, and the black pixels represent the binary value 0. In Fig. 5.14(b), we added white noise to the ideal CS measurement pattern, which models the noise happened on the DMD mirror plane due to issues like dust scattering and deformations/vibrations of mirror pixels happened in their tilting/resetting process. The average intensity of the white noise considered in this simulation is 0.53, and its standard deviation is 0.12. We used the ideal and the noise-contaminated patterns to generate CS measurement results, which were then input into the TwIST algorithm for reconstructing the original image cube. For the sake of paper space, we do not show the entire reconstructed image cubes. Instead, in top row images of Fig. 5.15, we show RGB images of the original (Fig. 5.15(a)) and the reconstructed image cubes (Figs. 5.15(b) and (c)). In bottom row images of Fig. 5.15, we show optical images of the original (Fig. 5.15(d)) and the reconstructed image cubes (Figs. 5.15(e) and (f)).

Comparing Fig. 5.15(b) with Fig. 5.15 (c) and comparing Fig. 5.15(e) with Fig. 5.15(f), we can see that the quality of the reconstructed RGB and optical images is apparently affected by the noise considered in the CS measurement pattern, in the sense that Figs. 5.15(c) and (f) look more blurry and noisy than Figs. 5.15(b) and (e). The PSNR value of the optical image reconstructed using the noisy CS measurement pattern is 15.69 dB, which is 9.6% lower than the PSNR value of the optical image reconstructed using the ideal CS measurement pattern (17.36 dB). To mitigate the quality degradation caused by noise contaminations, when solving the image reconstruction problem, it is helpful to consider the same amount of noise that happened in the CS measurement process in the system transfer matrix H.

In Fig. 5.16(a), we show the RGB image reconstructed when the same amount of noise that happened in the CS measurement process was considered in the system transfer matrix. Compared to Fig. 5.16(b), which is the RGB image reconstructed without considering the noise in the system transfer matrix , we can see that Fig. 5.16(a) looks less noisy and the color contrast between the red and green tomatoes is more visually apparent. Figure 5.16(c) shows the optical image reconstructed when the noise is considered in the system transfer matrix and Fig. 5.16(d) shows the optical image reconstructed with the ideal system transfer matrix. We calculated the PSNR values of those reconstructed optical images and noted that, by considering the noise in the system transfer matrix, the PSNR value of the reconstructed optical image was improved from 15.69 dB (Fig. 5.16(d)) to 17.07 dB (Fig. 5.16(c)).

In the above simulation, we only considered one kind of noise contaminations in the DMD-SSI system. In experimental settings, other kinds of noise contaminations, such as mechanical vibrations, stray light in the lab environment, and electronic noise of the camera, cause additional errors to the CS measurement results. To fully account for those non-ideal factors, a calibration process was proposed in [51,53], which involves the acquisition of a series of monochromic images for the CS measurement pattern. Each of
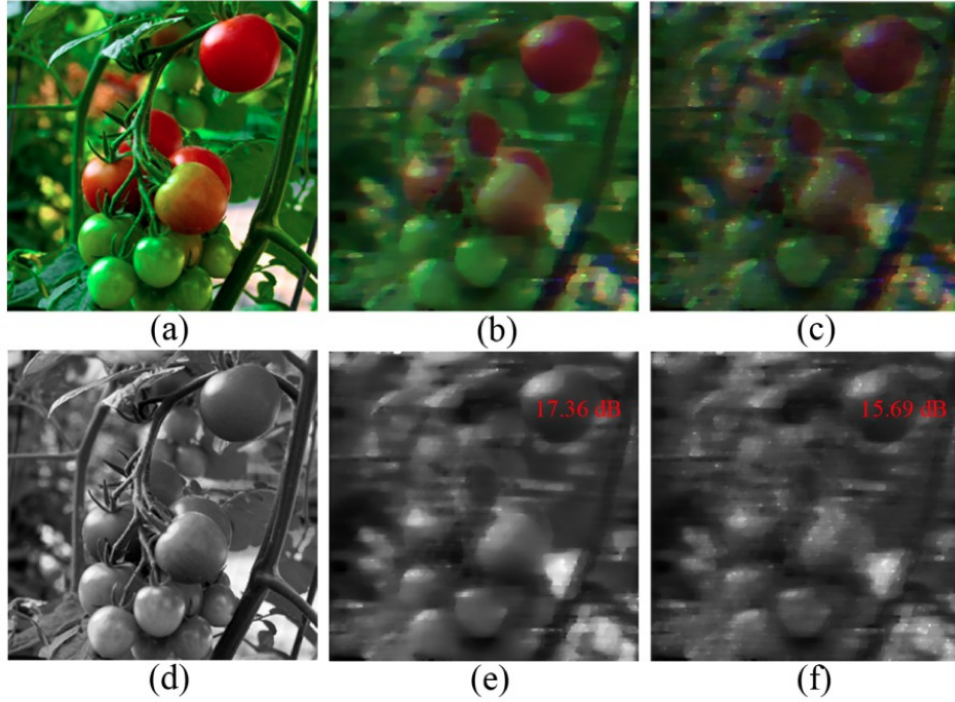
Figure 5.15: (a) RGB image of the original image cube. (b) RGB image of the reconstructed image cube when the ideal random pattern was used to implement the CS measurement process. (c) RGB image of the reconstructed image cube when the noise-contaminated CS measurement pattern was used. (d) Optical image of the original image cube. (e) Optical image of the reconstructed image cube when the ideal CS measurement pattern was used. (f) Optical image of the reconstructed image cube when the noise-contaminated CS measurement pattern was used.

the monochromic images contains not only the spatial information of the implemented CS measurement pattern, but also all the wavelength-dependent noises and aberrations. The acquired monochromic images are then used to build a practical system transfer matrix for the experimental setup, such that all the noises and aberrations present in the experiment setup can be considered in the image reconstruction process. Figure 5.17 shows the calibration setup for our DMD-SSI system, which is composed of a wide-band Xenon lamp (Newport, stock number: 66477) and a visible monochromator (Oriel, model number: 77200).

In the calibration process, monochromic emissions generated from the monochromator are used to illuminate the DMD mirror plane and corresponding monochromic images of the implemented DMD pattern can be captured by the CCD camera installed in the DMD-SSI system. Figure 5.18(a) and (b) show an ideal CS measurement pattern and one of its monochromic images captured at the wavelength of 612 nm. In this figure, we can see that the monochromic image is contaminated with random noises and optical blurs. Also, the intensity contrast between the on and off pixels is lower in the monochromic image than in the ideal CS measurement pattern. All of those non-ideal factors will be considered in the image reconstruction process by the practical system transfer matrix.

In the calibration process, we capture monochromic images every 1 nm from 450 nm to 685 nm. Therefore, a total number of 236 monochromic images are captured. Those monochromic images are spatially separated, due to the dispersion performance of the prism. Not all of those 236 monochromic images are used to build the transfer matrix for the experimental setup. This is because the CCD camera cannot accurately resolve spatial separations smaller than 1 CCD pixel. Therefore, monochromic images that have spatial separations smaller than 1 CCD pixel are considered as identical in this calibration process. From those 236 monochromic images captured in the calibration process, we found 24 non-
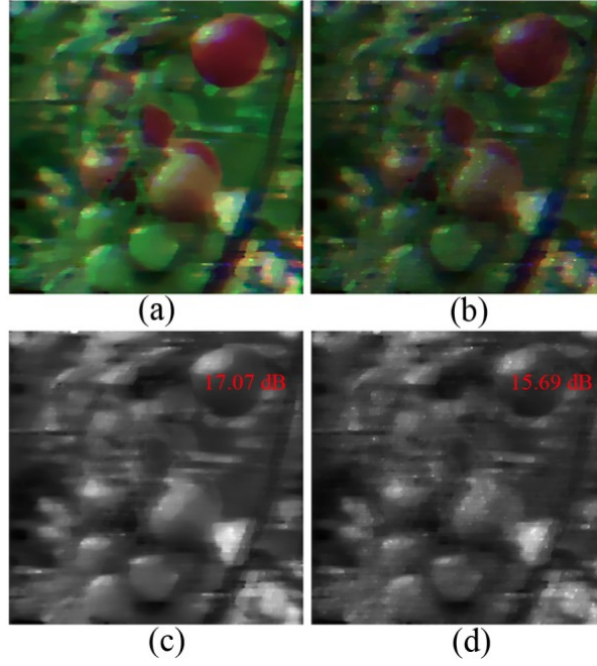
Figure 5.16: RGB and optical images reconstructed using the noise-contaminated CS measurement pattern. In (a) and (c), the same amount of noise happened in the CS measurement process was considered in the system transfer matrix. In (b) and (d), the noise was not considered in the system transfer matrix.
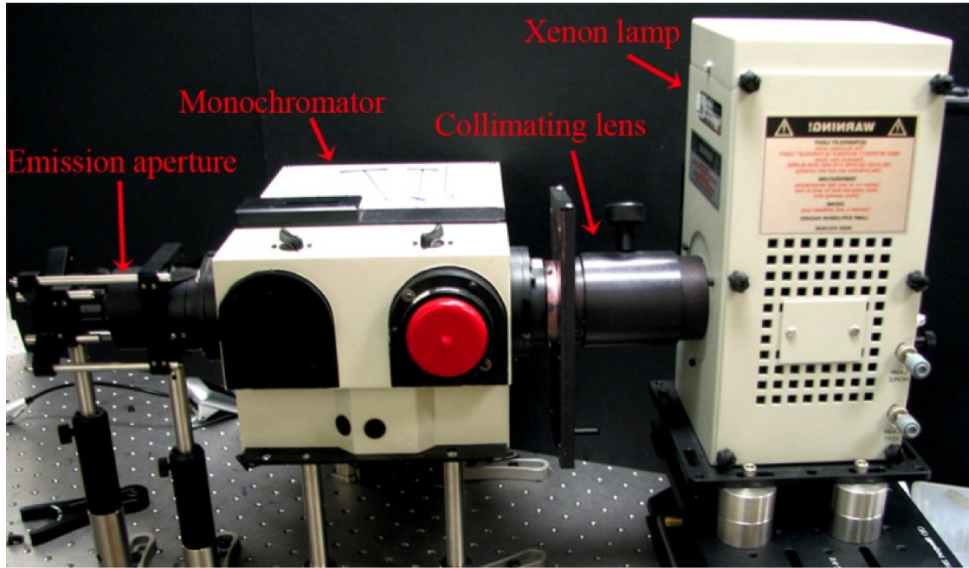

Figure 5.17: Calibration setup for the DMD-SSI system.

identical images and used them to build the practical system transfer matrix. We say those 24 non-identical monochromic images form a calibration cube for the experimental setup. Figure 5.19(a) shows the wavelength information of the 24 non-identical monochromic images. Figure 5.19(b) shows the first and the last monochromic images included in the calibration cube, which were captured at the wavelengths of 453 nm and 671 nm, respectively. Fake colors are added to those two monochromic images to enhance their visual perception. We can see that those two monochromic images are spatially separated by 23 CCD pixels in the horizontal direction of the CCD camera. Please note that the calibration process is only useful to one experimental setup. If the optical/mechanical architecture of the DMD-SSI system is
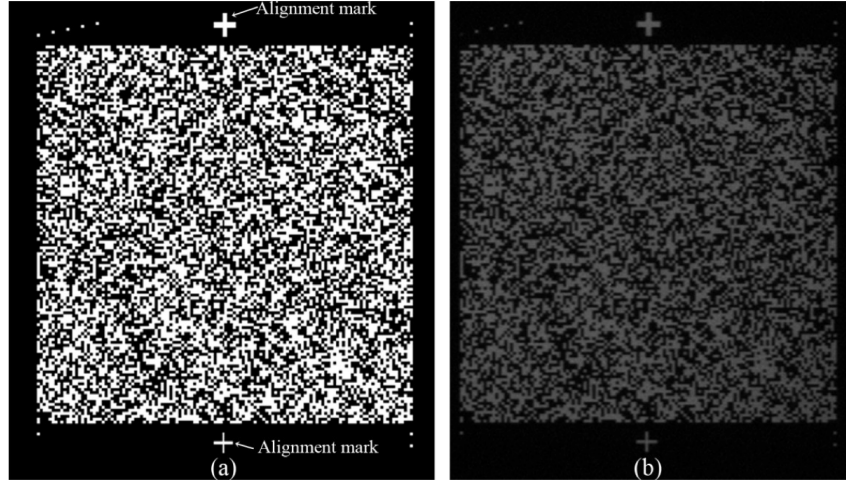
Figure 5.18: (a) An ideal CS measurement pattern (128 × 128). (b) A monochromic image of the CS measurement pattern captured by the DMD-SSI system at 612 nm.

modified, such as a new lens is installed or the position of the prism is moved, a new calibration process needs to be implemented for the modified setup.
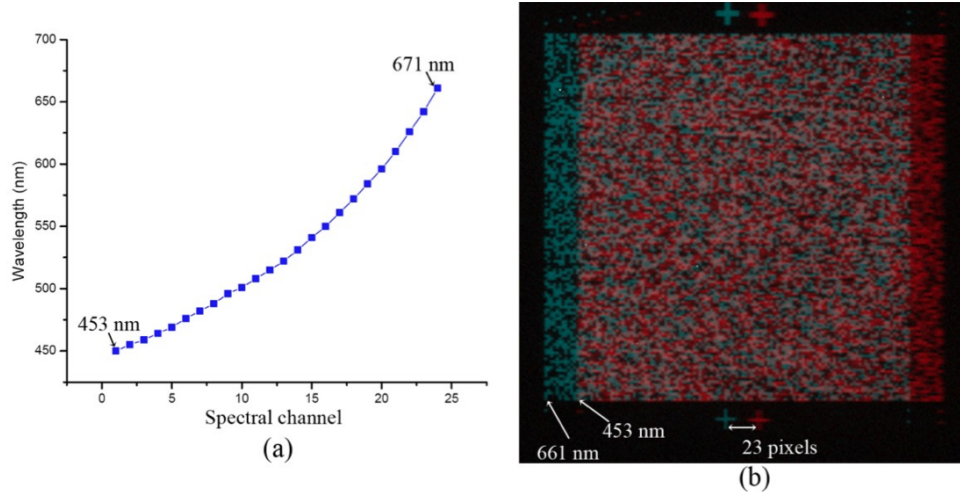

Figure 5.19: (a) Wavelength information of non-identical monochromic images captured in the calibration process. (b) Monochromic images captured at 453 nm (red pattern) and 671 nm (blue pattern).

5.6 Experimental Results

Figure 5.20 shows an image reconstruction result obtained from the experimental DMD-SSI setup. In this case, the binary random pattern shown in Fig. 5.18 was used as the CS measurement pattern. Figure 5.20(a) shows a CCD image of the imaging target, which is composed of a green and a red toy car. Figure 5.20(b) shows the CS measurement result generated from the DMD-SSI setup. Figure 5.20(c) shows the reconstructed image cube of the imaging target. We can see that the green car was reconstructed with strong intensities in green spectral channels (529 nm to 580 nm), whereas the red car was reconstructed with strong intensities in red spectral channels (605 nm to 636 nm).

In Fig. 5.21, we show another set of image reconstruction result which was generated with a different
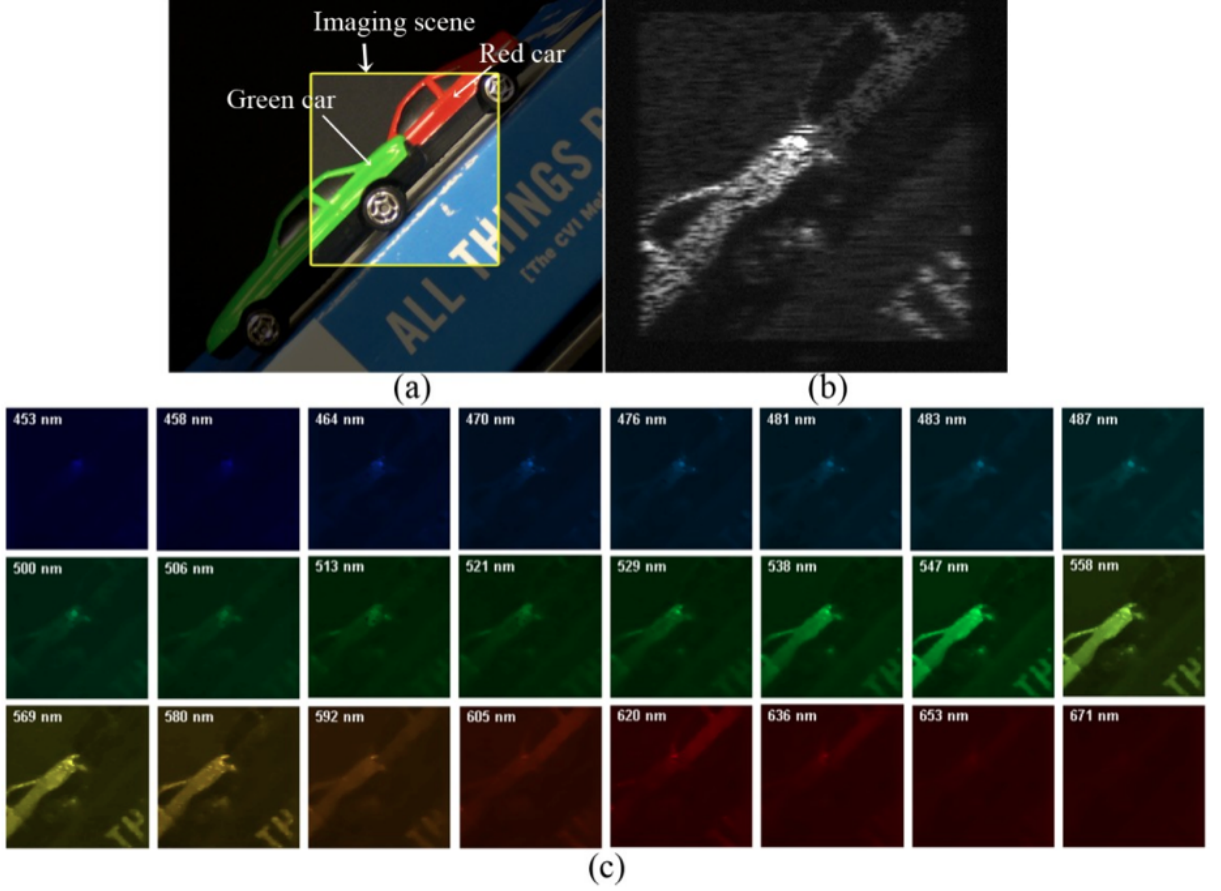
Figure 5.20: (a) CCD image of the imaging target. (b) CS measurement result acquired by the DMD-SSI system for the imaging target. (c) Reconstructed spatial/spectral image cube (fake colors were added to enhance the visual perception of those spectral images).

imaging target. Also, a different CS measurement pattern was used to realize the CS measurement process. A new calibration process was implemented prior to this image reconstruction experiment. Figure 5.21(a) shows a monochromic image of the CS measurement pattern used in this experiment, which was captured at the wavelength of 587 nm. Figure 5.21(b) shows a CCD image of the imaging target used in this experiment, which is composed of three colorful plastic stripes. Figure 5.21(c) shows the CS measurement result captured from the experimental DMD-SSI setup. Figure 5.21(d) shows the reconstructed spatial/spectral image cube of the imaging target. In this result, we can see that the blue color stripe was reconstructed with strong intensities in spectral channels from 460 nm to 498 nm, whereas the green color stripe was reconstructed with strong intensities in spectral channels from 517 nm to 576 nm and the red color stripe was reconstructed with strong intensities in spectral channels from 601 nm to 663 nm. This reconstruction result is in accordance with our visual perception to the blue, green, and red color stripes in the imaging target.

5.7   Multi-shot CS Measurements

Multi-Shot CASSI (MS-CASSI) systems were developed to enhance the quality of image cubes reconstructed by conventional Single-Shot CASSI (SS-CASSI) systems. In MS-CASSI systems, the photomask is mounted on a piezo stage. By horizontally and/or vertically shifting the photomask using the stage, different regions of the random pattern coated on the photomask can be used to impose intensity modulations on the original image cube. MS-CS measurement processes can be realized by using multiple shifts of the piezo-stage. In [52], the authors demonstrated the quality enhancement brought by the MS-CASSI
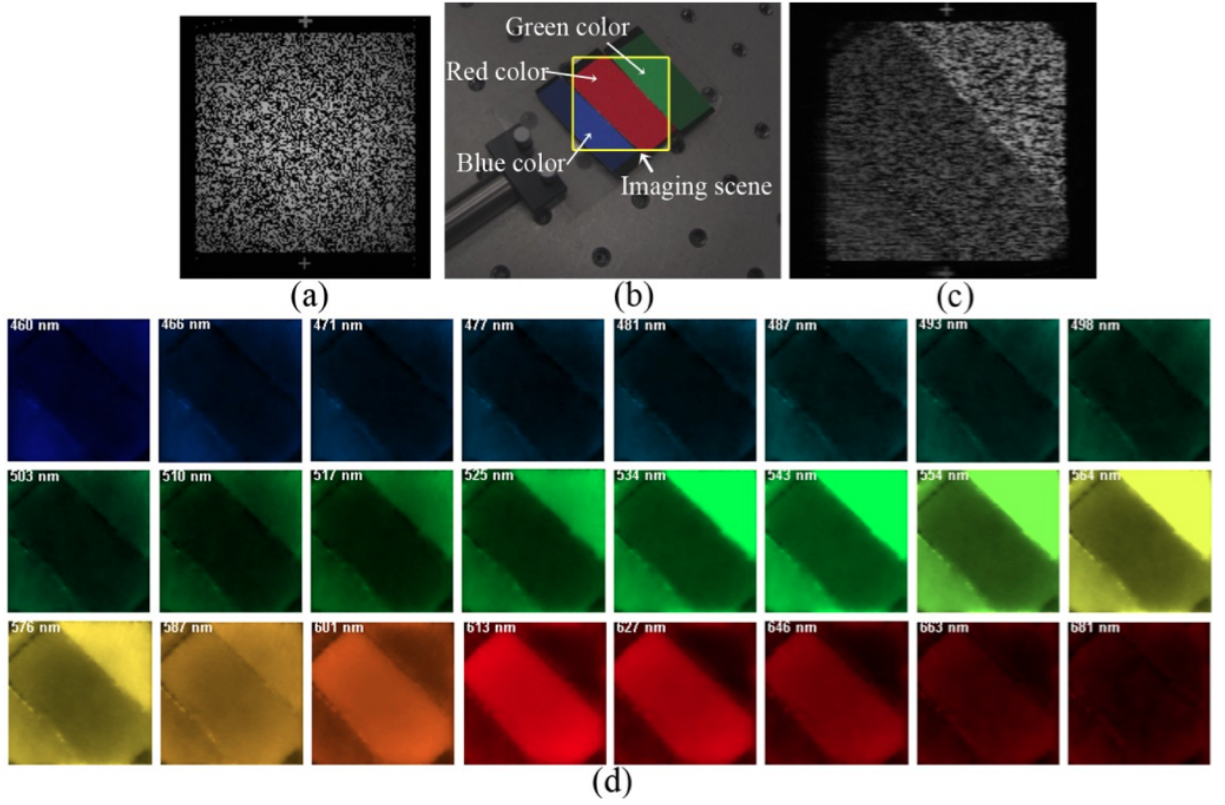
Figure 5.21: (a) Monochromic image of the CS measurement pattern captured at 587 nm. (b) CCD image of the imaging target. (c) CS measurement result. (d) Reconstructed spatial/spectral image cube of the imaging target (fake colors were added to enhance the visual perception).

system. DMD-SSI systems can also be used to realize MS-CS measurement processes [55]. Compared to piezo stage-based MS-CASSI systems, DMD-SSI systems realize MS-CS measurement processes without mechanical motions, and thus, they are free from registration errors happened in the motion process. More importantly, DMD-SSI systems has a much higher flexibility in implementing CS measurement patterns, in the sense that in addition to the shifted random patterns that the piezo stage-based system can only provide, DMD-SSI systems can use patterns of independent designs to realize MS-CS measurement processes.

We implemented MS-CS measurement processes with our DMD-SSI setup. Figure 5.22(a) shows the imaging target used in this experiment, which is a red chili pepper with a green stem. Figure 5.22(b) shows one of the CS measurement patterns used in this experiment. Figure 5.22(c) shows the CS measurement result generated when the CS measurement pattern shown in Fig. 5.22(b) was implemented with the DMD. Top row images in Fig. 5.23 show spectral images (channels 13-24 of the reconstructed image cube) reconstructed with a Single-Shot CS (SS-CS) measurement process. Center row images in Fig. 5.23 show spectral images reconstructed with a 6-shot MS-CS measurement process implemented with shifted random patterns and bottom row images show spectral images reconstructed with a 6-shot MS-CS measurement process implemented with independent random patterns.

In this figure, we can see that both the SS-CS and the MS-CS measurement processes can result in meaningful image reconstruction results. We can see that the green stem portion of the pepper target was reconstructed with strong intensities in green spectral channels, which are from 538 nm to 581 nm (channels 14-18), and the red body portion of the pepper target was reconstructed with strong intensities in red spectral channels, which are from 606 nm to 670 nm (channels 20-24). However, we noted that the spectral images reconstructed with MS-CS measurement processes have much better quality than the
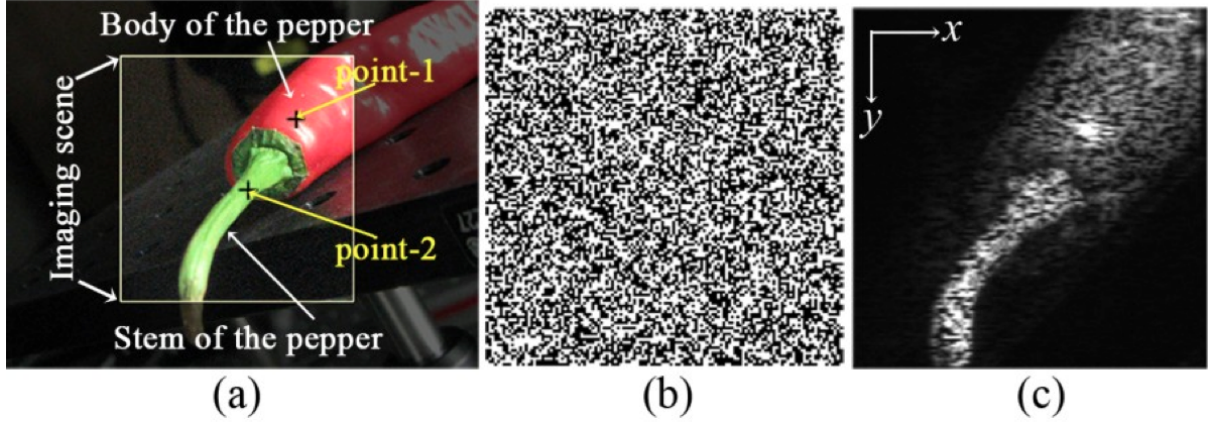
Figure 5.22: (a) CCD image of the imaging target. (b) One of the CS measurement patterns used in the MS-CS measurement experiment. (c) CS measurement result generated from our experimental setup, when the pattern shown in Fig. 5.22(b) was implemented with the DMD.

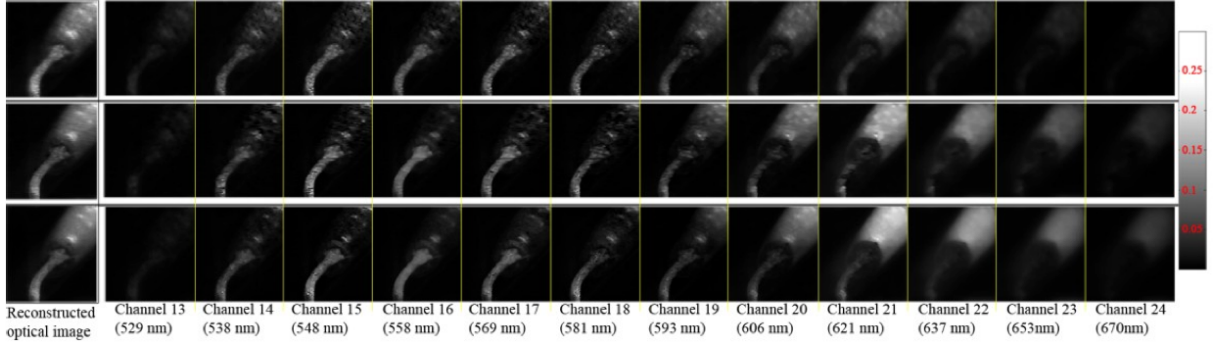| Reconstructed optical image | Channel 13 (529 nm) | Channel 14 (538 nm) | Channel 15 (548 nm) | Channel 16 (558 nm) | Channel 17 (569 nm) | Channel 18 (581 nm) | Channel 19 (593 nm) | Channel 20 (606 nm) | Channel 21 (621 nm) | Channel 22 (637 nm) | Channel 23 (653nm) | Channel 24 (670nm) |

Figure 5.23: Top row images: spectral images (channels 13-24 in the reconstructed image cube) reconstructed with a SS-CS measurement process. Center row images: spectral images reconstructed with a 6-shot MS-CS measurement process, implemented with shifted random patterns. Bottom row images: spectral images reconstructed with a 6-shot MS-CS measurement process, implemented with independent random patterns.

spectral images reconstructed with the SS-CS measurement process, in the sense that they look less noisy and blurry. Also, in spectral images reconstructed with MS-CS measurement processes, the intensity contrast between the body/stem portions of the pepper target and the dark background is more visually apparent.

In Fig. 5.24, we show three colorful images generated by using channel 16 and channel 21 in the reconstructed image cubes as the green and red color components in the RGB data format. We can see that those colorful images look similar to the CCD image of the imaging target shown in Fig. 5.22(a). Also in this figure, we can see that colorful images reconstructed with MS-CS measurement processes look less noisy than the one reconstructed with the SS-CS measurement process. They also have a higher color contrast between the stem and the body portions of the pepper target. We also evaluated the intensity variations of the reconstructed image cubes at point-1 and point-2 on the imaging scene, which are located on the body and stem portions of the pepper target, respectively. The locations of point-1 and point-2 are demonstrated in Fig. 5.22(a). Those intensity variations can be considered as reconstructed spectral curves on those two pixel locations. We also used a commercial spectrometer (Avantes, model number: AvaSpec-1024) to generate reference spectral curves at those two locations. Figure 5.25 shows the reconstructed (dotted lines) and the reference spectral curves (solid lines).
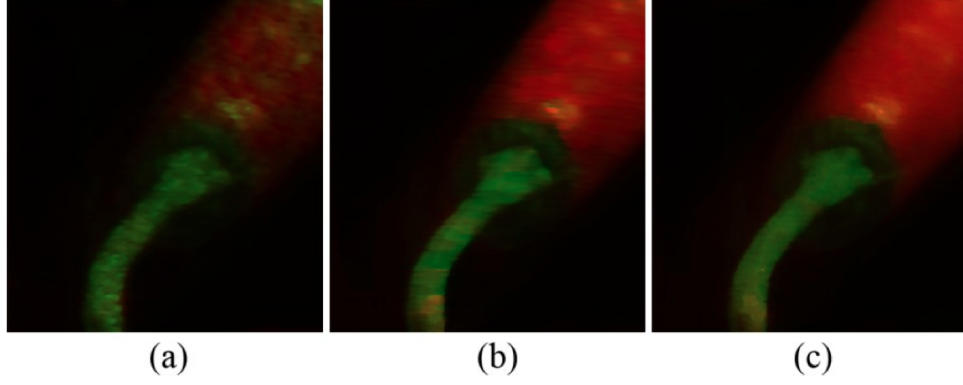
Figure 5.24: Colorful images synthesized using spectral channels 16 and 21 in the reconstructed image cubes as the green and red color components in the RGB data format. (a) Colorful image generated with the SS-CS measurement process. (b) Colorful image generated with a 6-shot MS-CS measurement process, implemented with shifted random patterns. (c) Colorful image generated with a 6-shot MS-CS measurement process, implemented with independent random patterns.
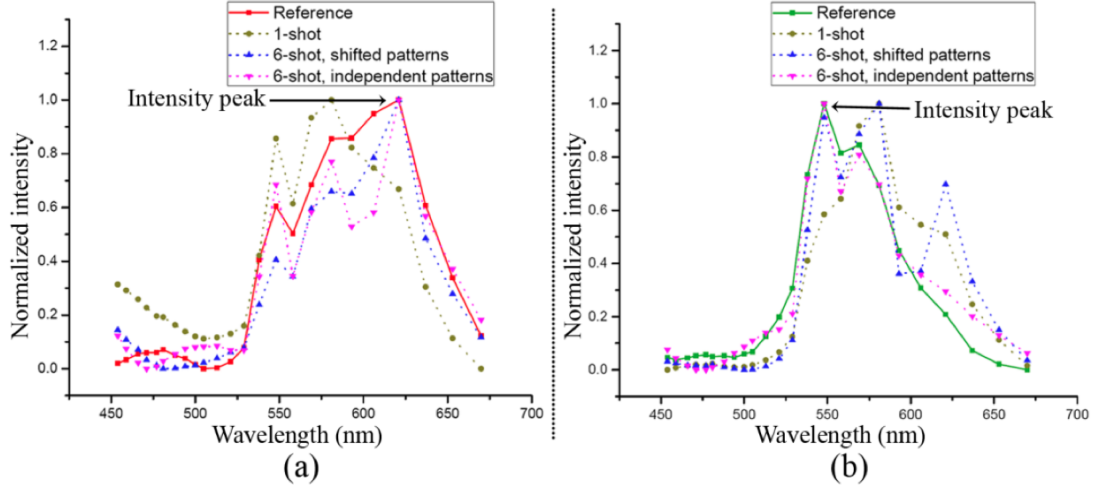

Figure 5.25: (a) Reconstructed and reference spectral curves measured at point-1 on the pepper target. (b) Reconstructed and reference spectral curves measured at point-2 on the pepper target.

In Fig. 5.25, we can see that the reference spectral curves (solid curves) have an intensity peak at the spectral channel of 621 nm for point-1 and an intensity peak at the spectral channel of 548 nm for point-2. We call those two spectral channels the fingerprint spectral channels of the pepper target in the body and stem portions. In spectral curves reconstructed with the SS-CS measurement process (dotted line in dark yellow color), we can see the intensity peaks miss the ones in the reference spectral curves, which implies the reconstruction quality is not ideal. In this case, the MSE values of the deviations from the reconstructed spectral curves to the reference curves are 3.3% at point-1 and 2.9% at point-2, respectively. For spectral curves reconstructed with MS-CS measurement processes (dotted curves in blue and pink colors), we can see that their intensity peaks match the ones in the reference spectral curves. Also, MSEs of the deviations from the reconstructed spectral curves to the reference curves dropped to 1.2% and 1.4% for point-1, and to 2.4% and 0.4% for point-2, when shifted and independent random patterns were used to implement the MS-CS measurement processes, respectively.

Chapter 6

Communications System

The objective of this task is to develop a robust, low-delay, low-complexity, communication system for the transmission of multispectral measurements. In order to achieve robustness against changes in the channel quality, and to reduce the system complexity with respect to standard communications systems, we have developed a discrete-time, analog-processing system that completely skips the digital domain and achieves a performance close to the theoretical limits. The key idea at the encoder site is to perform simple non-linear transformations on the available measurements. These transformations, denoted as M() and T() in Fig. 1, depend on the source/channel statistics and on the desired transmission rate. The resulting values are directly transmitted though the communications channel using very simple PAM signaling. ML decoding at the receiver is straightforward, and leads to excellent performance. The research developed in this project has focused on the development of the appropriate non-linear mappings, and on the implementation of testbeds to study the performance of the proposed system in practical scenarios.
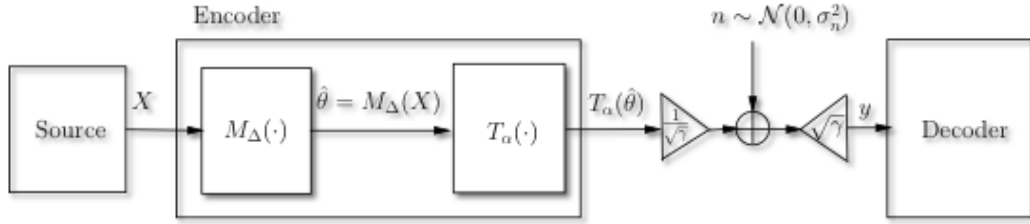

Figure 6.1: Discrete-time continuous-amplitude communications system

6.1 Development of non-linear mappings

A key piece of our work is the development of low-complex non-linear mappings that match the statistics of the measurements to the channel, leading to performance close to the theoretical limits. We denote the number of measurements to be transmitted as N, and K denotes the total number of allowed channel uses. Then, the theoretical limit establishing the minimum amount of distortion (or equivalently, the maximum Signal to Distortion Ratio, SDR) that can be achieved for a certain channel quality is a function of the bandwidth reduction factor N/K and the Rate Distortion Function, R(D). This theoretical limit holds for any communication system, and our goal is to get as close as possible to the limit with the lowest possible complexity.

We started our research with the development of non-linear mappings for the case of independent and identically distributed measurements transmitted through RF wireless channels. We also implemented quasi-optimal decoding algorithms with very reduced complexity, close to that of Maximum Likelihood, ML. Next, we investigated mappings that exploit the correlation existing between the measurements to achieve an improved performance. Finally, we also developed mappings for the case in which the

measurements are transmitted optically, which presents new research problems as the characteristics of optical wireless channels, and thus the mapping designs, are very different from that of RF channels. Through the process, we also discovered a technique to simplify even more the encoding process when the bandwidth reduction factor is 2, decreasing the computational complexity of the system by an order of magnitude. Interestingly, the resulting performance in this case is very similar to that obtained with the original mappings.

6.2 Testbeds implementation

In addition to the theoretical work, we have implemented two testbeds to study the performance of the proposed system in practical scenarios. The first testbed, which will be described in more detail in the sequel, uses Software Defined Radios (SDRs) for the electromagnetic transmission of the measurements through wireless channels, while the second testbed performs wireless optical communications. The RF testbed is composed of two Universal Software Radio Peripherals (USRP2) (see Fig. 2). The transmit and receive antennas are separated 2 meters, and thus the wireless channel is a quasi-static fading channel, which for the transmission of each frame behaves as an Additive White Gaussian Noise (AWGN) channel. The system has a frequency of operation in the ISM band, fc=2.41 GHz, and the baseband sampling frequency is fs=195 samples/s. We apply a squared root raised cosine pulse-shaping filter with a roll-off factor of 20% and the symbol period is Ts=20 samples/s. As explained before, we used the very simple PAM modulation and transmit data just using the in-phase component.

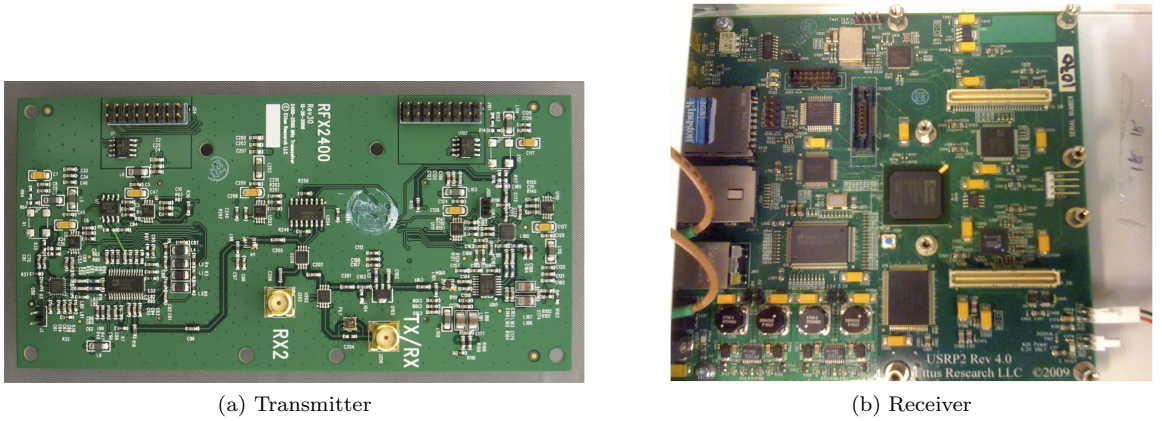(a) Transmitter   (b) Receiver

Figure 6.2: RF testbed

In order to perform frequency synchronization, the testbed used a global GPS Disciplined Oscillator shared between the transmitter and the receiver. The main goal of this procedure is to align the frequency of the carrier at the receiver with the frequency of the carrier at the transmitter. The result is a coarse-grained frequency synchronization that avoids the continue rotation of the received symbols at the receiver. Although this technique solved in general the problem of frequency mismatch, there was a remaining impairment related to a constant carrier phase error. We addressed this impairment using SISO frequency estimator algorithms (Kays estimator) that leads to good results in the testbed implementation. In terms of frame synchronization, we divide the data in frames of fixed size (10,000 symbols), and at the beginning of each frame we add a known pilot sequence of 101 symbols generated by a BPSK modulation. At the beginning of each received frame, we perform a cross correlation procedure between the received frame and the expected pilot sequence in order to find the start of the sequence.

6.3 Results

Our results focus on the transmission of the multispectral measurements through the RF testbed. As explained before, the development of appropriate mappings depends on the statistics of the measurements,

(a) Original measurements
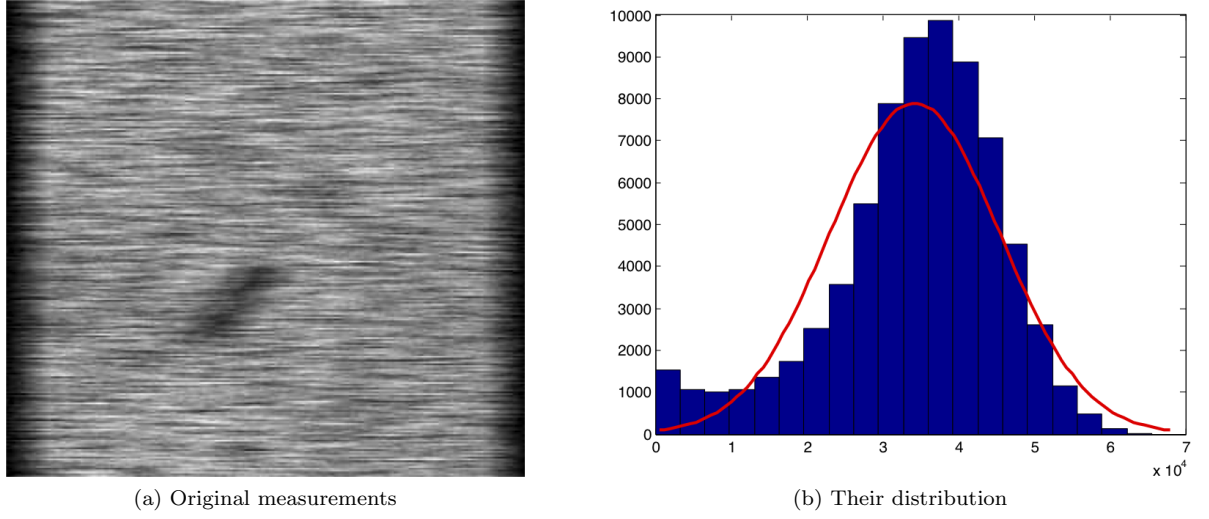

(b) Their distribution

Figure 6.3: Notice the good match between the measurements and the Gaussian distribution

which, as shown in Fig. 3, can be accurately approximated by a Gaussian distribution. We consider two bandwidth reduction factors: N/K=1, or direct transmission, and N/K=2.

In the case of N/K=1, it is well known that direct transmission through an AWGN channel is optimal provided that the measurements are iid and Gaussian. Therefore, since the wireless channel can be approximated as AWGN, the performance of the proposed system should approach the theoretical limit for Gaussian sources, which can be easily calculated using information theoretical arguments. Indeed, Fig. 4(left) shows that simulation results with MMSE decoding perfectly fit the theoretical limit, while, as expected, ML decoding results in performance lost for low signal to noise ratios in the channel (CSNR). Notice the excellent match between simulation results and the testbed evaluation. Similar results can be seen in Fig. 4(right) for the case in which the bandwidth reduction factor is N/K=2.
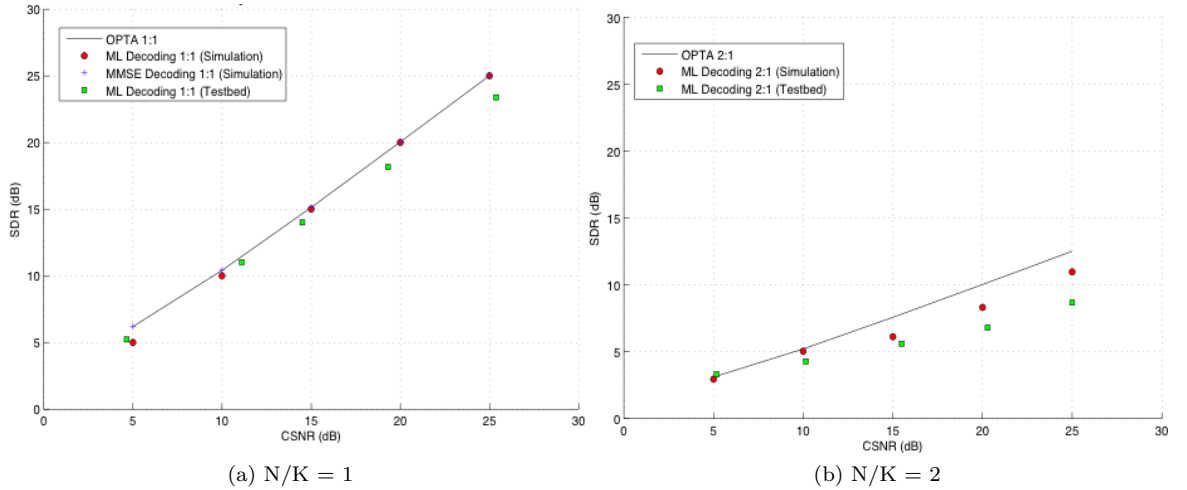

(a) N/K = 1

(b) N/K = 2

Figure 6.4: Theoretical limit and performance of the proposed system for the transmissiosn of the original measurements through an RF wireless channel. The system is evaluated through simulations and through the testbed.

Publications

Journals

- H. Arguello, H. Rueda, Y. Wu, D. W. Prather, G. R. Arce, Higher-order computational model for coded aperture spectral imaging. Applied Optics, 52, D12-D21, (2013)

- H. Arguello, C. Correa, G. R. Arce, Fast lapped block reconstructions in compressive spectral imaging. Applied Optics, 52, D32-D45, (2013)

- H. Arguello and G. R. Arce, Rank minimization code aperture design for spectrally selective compressive imaging. IEEE Trans. Image Process., Vol. 22, pp. 941-954, (2013).

- H. Arguello and G. R. Arce, Code aperture optimization for spectrally agile compressive imaging. J. Opt. Soc. Am. A, 28 (11), 2400-2413, (2011).

- Y. Wu, I. O. Mirza, G. R. Arce, and D. W. Prather, "Development of a digital-micromirror- device-based multishot snapshot spectral imaging system", Opt. Lett. 36, 2692-2694 (2011).

Conferences

- H. Arguello, H. Rueda, Y. Wu, D. W. Prather, G. R. Arce, Demonstration of a Higher-order discretization model for compressive spectral imaging. COSI 2013, Arlington, VA, (June 2013)

- H. Arguello, H. Rueda, G. R. Arce, High precision discretization model for coded aperture-based compressive spectral imaging. IEEE ICASSP, Vancouver, Canada (May 2013)

- H. Arguello, G. R. Arce, Optimization of pseudorandom coded apertures for spectrally selective compressive imaging. SPIE conference on Defense, Security and Sensing, Baltimore, MD, USA (April 2013)

- H. Arguello, C. V. Correa, G. R. Arce, Block-based reconstructions for compressive spectral imaging. SPIE conference on Defense, Security and Sensing, Baltimore, MD, USA (April 2013)

- H. Arguello, H. Rueda, G. R. Arce, On super-resolved coded aperture spectral imaging. SPIE conference on Defense, Security and Sensing, Baltimore, MD, USA (April 2013)

- H. Arguello, H. Rueda, G. R. Arce, Spatial super-resolution in coded aperture spectral imaging. SPIE conference on Defense, Security and Sensing, Baltimore, MD, USA (April 2012)

- H. Arguello and G. R. Arce, Spectrally selective compressive imaging by matrix system analysis. OSA Optics and Photonics Congress, Monterey, CA, USA. (2012).

- H. Arguello and G. R. Arce, Restricted isometry property in coded aperture compressive spectral imaging. Submitted to IEEE Statistical Signal Processing Workshop, Ann Arbor, MI, USA (2012).

- H. Arguello and G. R. Arce, Spectrally selective code aperture design by rank minimization in compressive imaging. Submitted to OSA Optics and Photonics Congress, Monterey, CA, USA. (2012).

- H. Arguello and G. R. Arce, Code aperture agile spectral imaging (CAASI). In Proc. International Congress of Imaging and Applied Optics (Toronto, Canada, July 2011), OSA Optics and Photonics Congress.

- H. Arguello and G. R. Arce, Anomaly recovery from compressed spectral imagery via low-rank matrix minimization. In SPIE Conference on Defense, Security and Sensing (Orlando, Florida, April 2011), SPIE.

- Y. Wu, I. O. Mirza, P. Ye, G. R. Arce and D. W. Prather, "Development of a DMD-based compressive sampling hyperspectral imaging (CS-HSI) system", Proc. SPIE 7932, 79320I (2011).

- Y. Wu, I. O. Mirza, G. R. Arce and D. W. Prather, "Demonstration of a DMD-based compressive sensing (CS) spectral imaging system", CLEO 2011 - Laser Applications to Photonic Applications, OSA Technical Digest, (2011).

- H. Arguello and G. R. Arce, Code aperture design for compressive spectral imaging. In European Signal Processing Conference, EUSIPCO (Aalborg, North Denmark, August 2010), European Association for Signal Processing.

- H. Arguello, P. Ye, G. R. Arce, Spectral aperture code design for multi-shot compressive spectral imaging. In Proc. International Congress of Digital Holography and Three-Dimensional imaging (DH) (Miami, Florida, April 2010), OSA Optics & Photonics Congress, pp. 11-14.